

MASTER

Validation and improvement of a dynamic stiffness measurement setup

Wijnen, R.A.G.

Award date:
2019

[Link to publication](#)

Disclaimer

This document contains a student thesis (bachelor's or master's), as authored by a student at Eindhoven University of Technology. Student theses are made available in the TU/e repository upon obtaining the required degree. The grade received is not published on the document as presented in the repository. The required complexity or quality of research of student theses may vary by program, and the required minimum study period may vary in duration.

General rights

Copyright and moral rights for the publications made accessible in the public portal are retained by the authors and/or other copyright owners and it is a condition of accessing publications that users recognise and abide by the legal requirements associated with these rights.

- Users may download and print one copy of any publication from the public portal for the purpose of private study or research.
- You may not further distribute the material or use it for any profit-making activity or commercial gain

Validation and improvement of a dynamic stiffness measurement setup

R.A.G. (Ruud) Wijnen - 0856504
DC 2019.065

Supervisors: prof.dr. H. (Henk) Nijmeijer TU/e
dr.ir. R.H.B. (Rob) Fey TU/e
ir. Hein van Beek ASML
Twan van de Weijer, MSc ASML

Committee: prof.dr. H. (Henk) Nijmeijer
prof.dr.ir. I. (Ines) Lopez Arteaga
prof.dr.ir. A.S.J. (Akke) Suiker

Eindhoven University of Technology
Department of Mechanical Engineering
Dynamics and Control group

Eindhoven, 20th June 2019

Abstract

Dynamic stiffness is a widely used measure to characterize the isolation performance of vibration isolation systems. It describes the dynamic properties as function of frequency. In order to effectively employ a vibration isolation system in a specific vibration isolation application, its performance has to be experimentally characterized (as a function of frequency). For that purpose an experimental setup to measure the dynamic stiffness of vibration isolation systems has been developed a few years ago and is currently used within ASML. The dynamic stiffness measurement results are, however, influenced by the dynamic behavior of the measurement setup itself.

In this thesis the dynamic behavior of the dynamic stiffness measurement setup and its influence on the dynamic stiffness measurement results are investigated. Therefore, a test object has been designed according to specific requirements. This test object is used for the validation of the dynamic stiffness measurement setup. Its dynamic behavior is initially investigated by performing a numerical modal analysis (NMA) using a lumped mass-spring model. This model is experimentally validated by performing dynamic stiffness measurements with the test object mounted in the setup. The results of these measurements are also required to investigate at what frequencies the measurements are influenced by the dynamic behavior of the setup. This behavior is subsequently investigated by performing experimental modal analysis (EMA) on the setup. With this research each resonance peak in the dynamic stiffness measurements caused by dynamic behavior of the setup is clarified. From this it can be concluded that mainly the dynamic behavior of the shaker table configuration and the force cell influence the measurements. Thus, proposals for improvement of the setup are to design a lighter and stiffer force cell and shaker table configuration. This will move the influence of the dynamic behavior of these components outside the frequency range of interest of 1 - 2000 Hz.

Moreover, a finite element (FE) model with a simplified geometry of the real setup is made. This model is updated with the aid of the EMA results in order to obtain a valid and representative model. The purpose of the FE model is threefold. Firstly, it enables the prediction of the dynamic behavior of the setup. Secondly, it can be used to imitate the dynamic stiffness measurements with any object mounted in the setup in order to verify that setup dynamic behavior has minimal influence on the dynamic stiffness measurement. Thirdly, the FE model enables to test the influence of changes made to the setup in the model prior to practical implementation.

Nomenclature

Abbreviations

AM(s)	Airmount(s)
BF	Base frame
CMIF(s)	Complex mode indicator function(s)
CMS	Component mode synthesis
DFT	Discrete Fourier transform
DOF(s)	Degree(s) of freedom
EMA	Experimental modal analysis
EUV	Extreme ultraviolet
FC	Force cell
FE	Finite element
FEM	Finite element method
FFT	Fast Fourier transform
FRAC	Frequency response assurance criterion
FRF	Frequency response function
MAC	Modal assurance criterion
MF	Metrology frame
NMA	Numerical modal analysis
ODS(s)	Operational deflection shape(s)
PSD	Power spectral density
POB	Projection optics box
POI(s)	Point(s) of interest
SVD	Singular value decomposition
TM	Transmissibility
VIS(s)	Vibration isolation system(s)

Notation

q	Bold symbol indicates a matrix
\bar{q}	Bar indicates modal coordinate system
<u>q</u>	Underline indicates a column
\dot{q}	Dot indicates a first derivative
\ddot{q}	Double dot indicates a second derivative
\hat{q}	Hat indicates an estimator

Superscript

H	Indicating the Hermitian transpose
*	Indicating a complex conjugate

Subscript

B	Related to a data block
dyn	Dynamic
eff	Effective
i	Related to input
int	Interface
k	Related to eigenmode/eigenfrequency or a step
m	Related to modes
o	Related to output
par	Parasitic
pas	Passive
tot	Total
w	Related to windowed signal
xx	From x to x
xy	From x to y
yy	From y to y

Symbols

		Unit
a	Acceleration	m/s ²
d	Diameter	m
E	Young's modulus	Pa
f	Frequency	Hz
F	Force	N
H	FRF matrix	-
I	Area moment of inertia	m ⁴
k	Stiffness	N/m
L	Length	m
m	Mass	kg
n	Number of DOFs	-
N	Number of samples or normal payload	- or N
R	Rotation	rad or °
S	Power spectral density	-
t	Time	s
t ₀	Time shift	s
T	Measurement time or minimal period time	s
TM	Transmissibility	-
U	Displacement	m

Greek Symbols

γ^2	Coherence estimator function	-
λ	Eigenvalue	rad/s
μ	Mean	-
ξ	Dimensionless modal damping factors	-
Ξ	Diagonal damping matrix	-
ρ	Density	kg/m ³
σ	Standard deviation	-
σ^2	Variance	-
Σ	Singular value matrix	-
ψ^2	Mean square value	-
ω	Angular frequency	rad/s
Ω	Diagonal eigenfrequency matrix	rad/s

Contents

Abstract	i
Nomenclature	iii
1 Introduction	1
1.1 ASML	1
1.2 Vibration isolation	2
1.2.1 Dynamic stiffness	3
1.2.2 Dynamic stiffness measurement setup	6
1.3 Problem definition and research goals	7
1.4 Thesis outline	8
2 Modal analysis	9
2.1 Numerical modal analysis	9
2.1.1 Modal superposition	10
2.2 Experimental modal analysis	11
2.2.1 Experimental data	12
2.2.2 Fourier transformation	13
2.2.3 Random processes	15
2.2.4 System identification	16
2.2.5 Modal parameter estimation	16
2.3 Summary	17
3 Experimental setup and test object modeling	19
3.1 Lumped mass-spring model	19
3.1.1 Dynamic stiffness	21
3.2 Test object	22
3.2.1 Modal analysis	23
3.2.2 Dynamic stiffness	25
3.2.3 Pre-stressed modal analysis	28
3.3 Experimental modal analysis of the test object	30
3.4 Finite element model	34
3.5 Summary	35
4 Experimental measurements and validation	37
4.1 Dynamic stiffness measurements	37
4.1.1 Sensor locations	39
4.1.2 Repeatability test	42
4.1.3 Influence of dynamic behavior	45
4.2 Experimental modal analysis of the setup	46
4.3 Experimental versus numerical results	50
4.3.1 Modal analysis	50
4.3.2 Dynamic stiffness results	55
4.4 Discussion	57

5	Conclusions and recommendations	59
5.1	Conclusions	59
5.2	Recommendations	60
	Bibliography	61
A	Dynamic stiffness setup	I
A.1	Background	I
A.2	Setup pictures	I
B	Test object designs	VII
B.1	Modal analysis	VIII
C	Model reduction	XI
C.1	Component mode synthesis	XI
C.1.1	Craig-Bampton method	XII
C.1.2	Hintz-Herting method	XIII
D	Measurement plan	XV
D.1	Experimental modal analysis guide	XVII
D.1.1	Piezo measurements	XVII
D.1.2	Modal hammer measurements	XIX
E	Dynamic stiffness measurement investigations	XXI
E.1	Accelerometer fixation	XXI
E.2	Standstill measurements	XXII

Chapter 1

Introduction

Nowadays it is hard to imagine a world without daily life applications such as laptops, smart phones, televisions, cars, and even washing machines. One important thing that these applications have in common is the fact that they all contain microchips. A microchip is also referred to as an integrated circuit, which consists of a large collection of interconnected electronic components (transistors, resistors, capacitors) placed on a tiny piece of semiconductor material (silicon). The manufacturing of these chips is performed by printing a pattern onto a pre-processed silicon wafer coated with a light-sensitive chemical (photoresist). This patterning process where the coated wafers are exposed to a desired pattern of light is called (photo)lithography. Afterwards, the wafers are post-processed, tested, and cut into hundreds of single microchips. A fundamental step in these microchip manufacturing processes is lithography [1] and this is where ASML plays a huge role.

1.1 ASML

Currently, the world's largest supplier of lithography systems is ASML. These systems are used in the manufacturing process of microchips for the semiconductor industry. They have to be accurate at sub-nanometer scale to allow the shrink of microchips, but also extremely fast to enable a high throughput. One of the most recent ASML lithography system is shown in Figure 1.1 and is known as the TWINSCAN NXE system. The most important difference with its predecessor (TWINSCAN NXT) is that NXE systems use extreme ultraviolet (EUV) light which has a shorter wavelength in order to further shrink the size of microchip features. As a consequence, parts of the NXE systems have to work in vacuum and mirrors are used in the projection optics box (POB) instead of lenses.

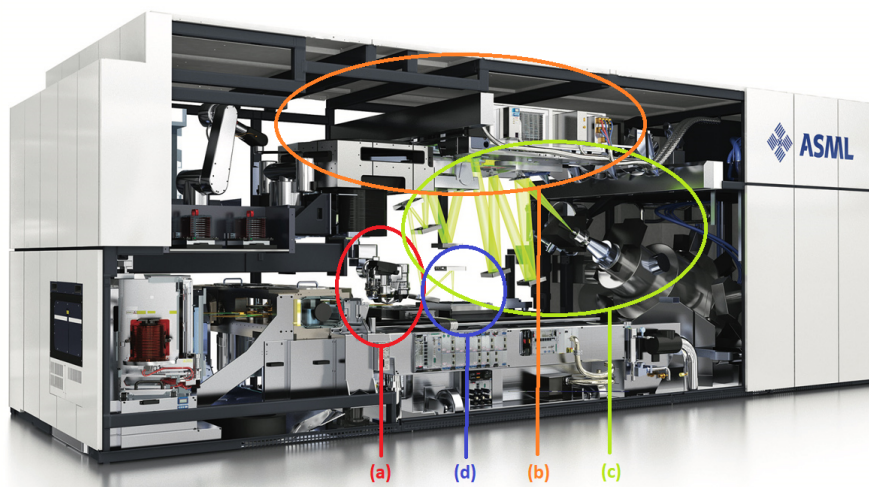


Figure 1.1: NXE lithography system with (a) the wafer stage measurement side, (b) the reticle stage, (c) the POB and the illuminator, and (d) the wafer stage exposure side [2].

Initially, a wafer is pre-aligned at the wafer stage measurement side (a). Meanwhile, a blueprint of a geometric chip pattern (reticle) is accurately positioned by the reticle stage (b). The EUV light produced by the illuminator (c) is reflected by the reticle. This creates an image of the pattern, which is reduced and focussed in the POB using mirrors and projected onto the surface of another wafer at the wafer stage exposure side (d) [3]. Afterwards, unwanted silicon is etched away revealing a three-dimensional structure. This process can be executed multiple times for tens of layers, ultimately creating a grid of hundreds of microchips on a single silicon wafer.

In ASML's latest lithography machines as shown in Figure 1.1, EUV light with a short wavelength of 13.5 nm is used to manufacture smaller chip features. This results in faster, more powerful chips marking the beginning of a new era in lithography. Prior to the current high-tech and advanced systems there is, however, a relatively short history yet rapidly grown evolution of the lithography systems within ASML. Figure 1.2 shows this evolution which started over 30 years ago.

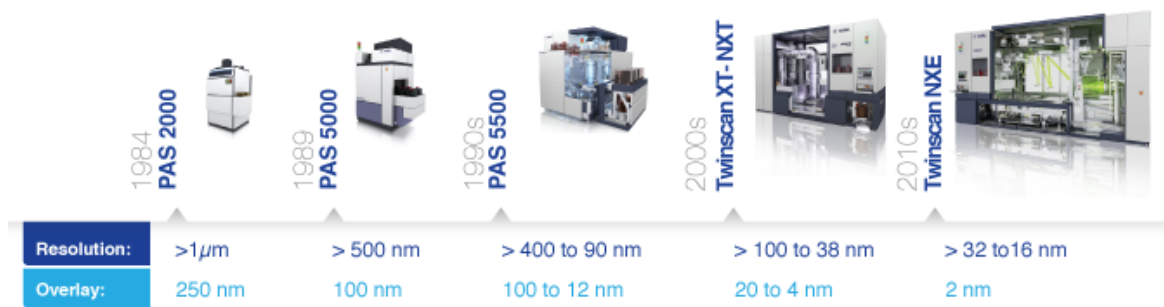


Figure 1.2: Evolution of the ASML lithography systems [4].

One can see that ASML's lithography systems have become larger and more accurate over the years. The resolution improved from micrometer scale to a couple of nanometers and the overlay improved with a factor of 125 in order to produce more detailed and smaller chips. This evolution is often associated with Moore's law, which describes a trend where the number of transistors per chip doubles roughly every two years as features on the chips become smaller. By making the features on a chip smaller they become more energy-efficient, the computational power increases, and the overall cost goes down which is all beneficial. Furthermore, the lithography systems have become faster resulting in higher throughput. Both trends combined as well as increasing excitation levels require accuracy specs to be stricter. This creates a challenge for the vibration isolation systems (VISs) within the ASML machines.

1.2 Vibration isolation

In many high-tech applications, vibrations are undesired and can cause unwanted disturbances on critical points of the system. These disturbances may lead to huge problems such as: life time reduction due to material fatigue, physical damage or destruction of a building (think of earthquakes), and inaccurate positioning of motion systems, e.g. in lithography machines, resulting in unacceptable errors and useless products such as microchips in this case. Preventing the latter is one of the main challenges in ASML's lithography systems and this is to a great extent achieved with vibration isolation. A vibration isolation system isolates the vibration sensitive object or payload from the source of vibration excitation [3]. Therefore, passive and active vibration isolation systems can be used. A passive vibration isolation system typically consists of a mechanical system which is a combination of carefully designed springs and dampers. The payload can then be seen as a mass-spring-damper system for which vibration isolation starts above the resonance frequency. This will be explained in more detail in Section 1.2.1. A passive isolation system is relatively cost efficient and non-complex, but isolating performance as well as payload positioning performance is limited. An active

vibration isolation system employs actuators and sensors to control and isolate incoming vibrations. These systems are more expensive and complex but can perform better in terms of isolation and positioning. Several types of VISs are used within the ASML machines where airmounts (AMs) are one of them. In Figure 1.3 an NXT system is schematically presented where these AMs are located in between the base frame (BF) and the metrology frame (MF).

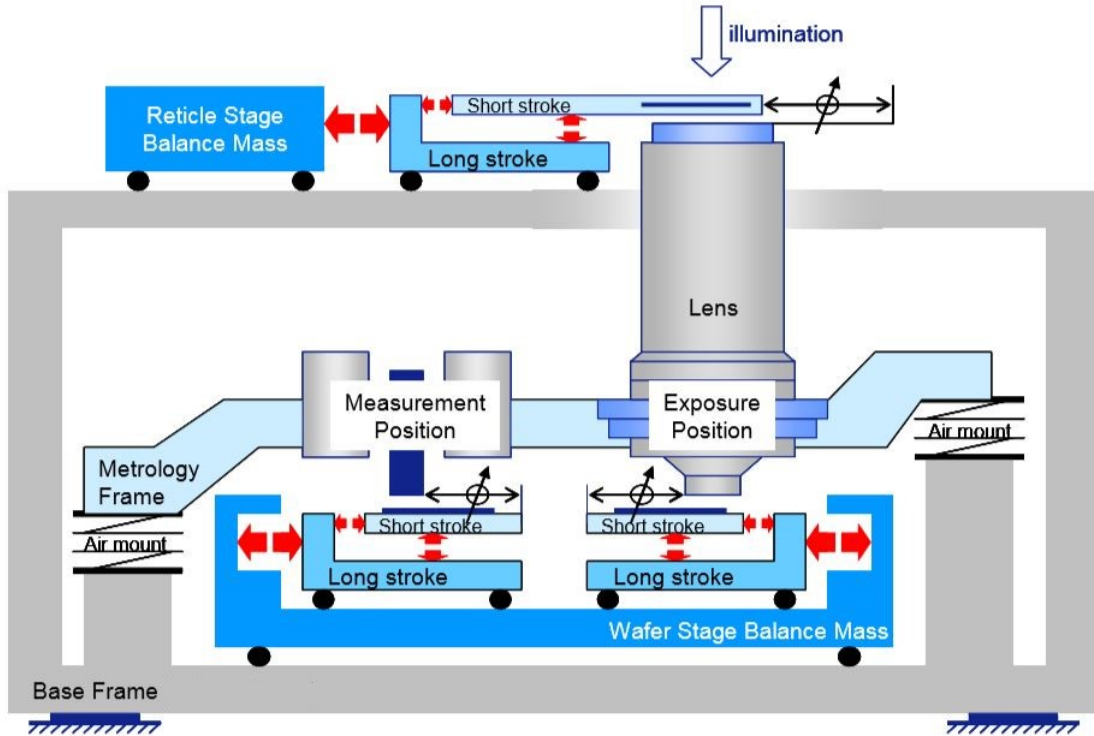


Figure 1.3: Schematic representation of a TWINSKAN NXT ASML lithography system [5].

During the exposing of wafers the lens should remain as still as possible for good imaging. It has, however, been found that relative small disturbances on the BF can easily lead to significant performance errors. A source of these disturbances are the scanning stages, which can cause large forces exciting the BF. These excitations follow their guidance path through the AMs to the MF and the lens (receiver). The purpose of the AMs is to actively isolate the MF from vibrations coming from the BF (transmissibility), dampen MF vibrations from disturbances acting on the MF (compliance), and position the MF relative to the BF (drift compensation) [6]. Therefore, the lens is mounted on the MF using AMs to isolate it from vibrational disturbances as much as possible. The positioning of the AMs is such that they can provide isolation and position control in six degrees of freedom (DOFs). In the NXE systems, AMs are also used between the BF and the illuminator to isolate the illuminator from internal and external vibrations. This does not apply to NXT systems such as the one shown in Figure 1.3. It is thus desired to create a vibration free environment (silent world) by isolating vibrations from the outside world due to wafer stage and reticle stage scans, human activities, and floor vibrations. Therefore, exact knowledge of the behavior of VISs in the frequency range of interest is required.

1.2.1 Dynamic stiffness

Different frequency dependent measures can be used during the characterization of isolation performance of VISs. A commonly used frequency dependent measure to characterize the isolation performance of vibration isolation systems is transmissibility (TM). It is defined as the ratio of vibration between the isolated mass and the source of vibration as function of frequency. A schematic representation to clarify this definition is given in Figure 1.4 by means of a lumped mass-spring model

in which the two masses are separated by a VIS with (dynamic) stiffness k_{dyn} .

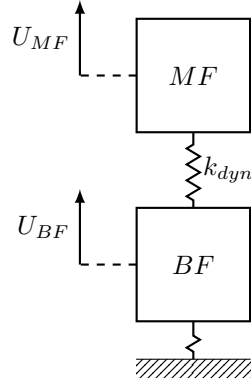


Figure 1.4: Schematic representation of vibration isolation.

In this case the vibrations are the resulting displacements of the MF and the BF due to a disturbance force on the BF. The transmissibility can then be expressed as

$$TM(f) = \frac{U_{MF}(f)}{U_{BF}(f)}, \quad (1.1)$$

where U_{MF} [m] is the displacement of the metrology frame as function of frequency, and $U_{BF}(f)$ [m] the displacement of the base frame as function of frequency. Figure 1.5 shows an example of the transmissibility of the lumped mass-spring model as a result of a disturbance on the BF.

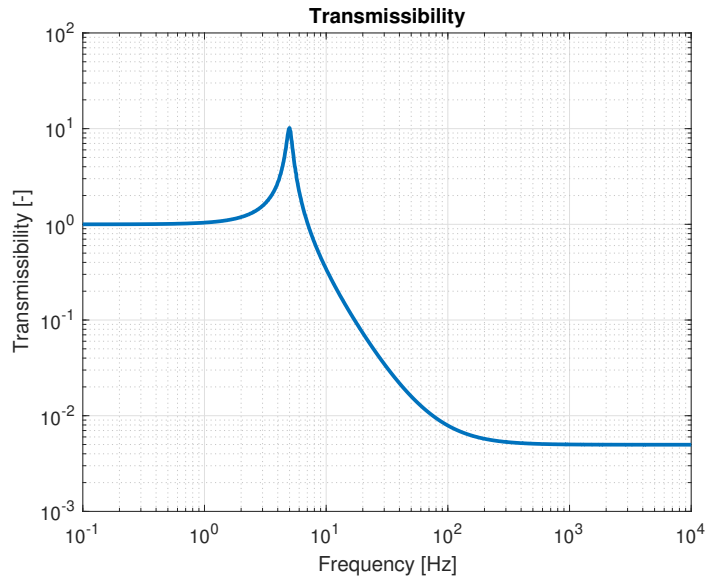


Figure 1.5: The transmissibility of a vibration isolation system.

It can be seen that for low frequencies the MF follows the vibrations of the BF. In this frequency region $TM(f) = 1$ and the VIS does not make a difference. For $TM(f) > 1$ the BF vibrations are amplified to the MF and performance gets worse, which is undesirable and may occur around the resonance frequency. The height of the resonance peak can be reduced by adding (more) damping. Moreover, the location of the resonance peak can be shifted to the left or to the right by decreasing or increasing the stiffness, respectively. For frequencies beyond the resonance frequency, i.e. $TM(f) < 1$, only a part of the vibrations of the BF are transmitted to the MF. This is where the MF gets isolated from vibrations on the BF. The TM curve has a -2 slope here and at a certain frequency the TM

reaches a saturation level where the slope is increased by +2 to a 0 slope due to internal dynamics of the VIS. Note that the transmissibility approach considers the vibration isolation system as a black box where isolation performance is investigated on system level.

There is also an option to investigate vibration isolation performance on module level when exact knowledge of the dynamic behavior of VISs in the frequency range of interest is required. For this purpose the dynamic stiffness is used as a frequency dependent measure to characterize the isolation performance of an isolation system. The dynamic stiffness refers to the extended frequency region where also the internal dynamics of vibration isolators becomes important. It is the frequency dependent stiffness of the spring indicated with k_{dyn} as shown in Figure 1.4 and can be defined as the force at the MF that results from a relative displacement between the MF and BF due to a disturbance force on the BF. This can be expressed as

$$k_{dyn}(f) = \frac{F_{MF}(f)}{|U_{MF}(f) - U_{BF}(f)|}, \quad (1.2)$$

where $k_{dyn}(f)$ [N/m] is the dynamic stiffness as function of frequency, and $F_{MF}(f)$ [N] the force on the metrology frame as function of frequency. Figure 1.6 shows an example of the dynamic stiffness obtained with the lumped mass spring-model .

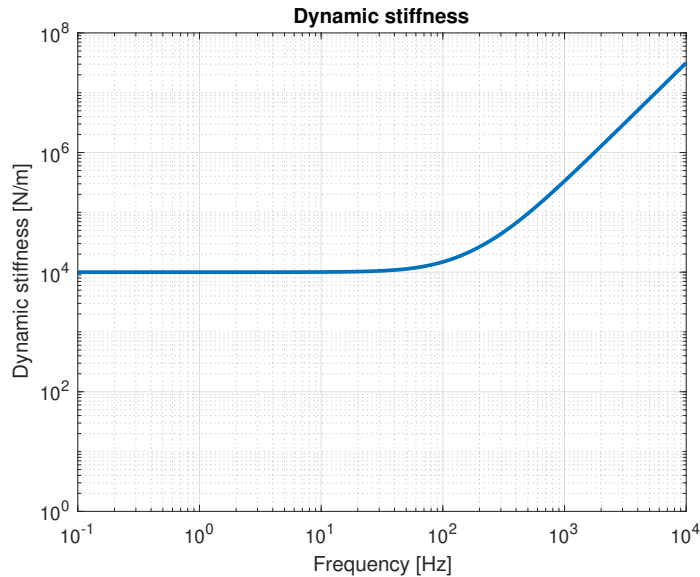


Figure 1.6: The dynamic stiffness of a vibration isolation system.

For low frequencies the static stiffness of the vibration isolation system is represented with the horizontal stiffness line. By increasing or decreasing this stiffness the line will be shifted up or down, respectively. At a certain frequency the dynamic stiffness increases with a +2 slope due to internal dynamics of the VIS. Note that this happens at the same frequency as where the TM reaches its saturation level, hence these two measures for characterization of isolation performance of VISs are related.

Measuring the dynamic stiffness in a wide frequency range is difficult. There are two basic approaches: the indirect method where the transmissibility is measured and mass and inertia properties are used to approximate forces at the MF, or the direct method where the transmitted force is directly measured via a force cell attached to the MF. The main disadvantage of the indirect TM method is the influence of forces introduced by links parallel to the test object. It is impossible to distinguish between these forces and forces transmitted via the test object. The latter is not measured directly and an approximation has to be made which is prone to errors. The direct dynamic stiffness method, however, directly measures forces transmitted via the test object for which no approximation is needed and is therefore used to characterize vibration isolation performance. In order to effectively use an isolator in a specific vibration isolation application, its stiffness and damping properties have

to be experimentally characterized as a function of frequency [7]. It is therefore highly relevant to have a setup that can accurately measure the dynamic stiffness of vibration isolators.

1.2.2 Dynamic stiffness measurement setup

A test setup to measure the dynamic stiffness of vibration isolation systems has been developed by Philips Innovation Services (PInS) a few years ago and is adopted by ASML. The setup in its current state is shown in Figure 1.7, which also indicates the components of the setup and the global coordinate system throughout this thesis. A more detailed background of the setup is given in Appendix A including a list with measurement equipment and additional detailed pictures of the setup components.

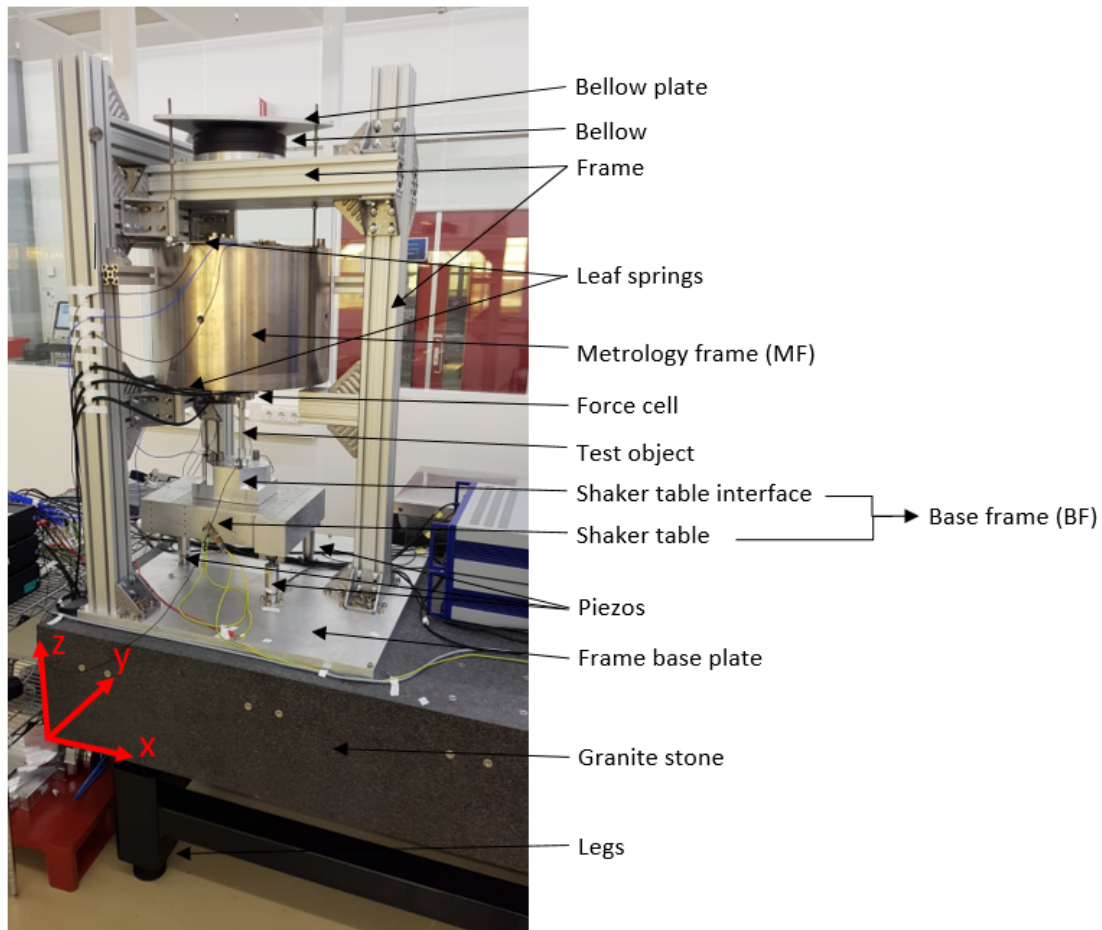


Figure 1.7: The dynamic stiffness measurement setup.

This setup can be used to determine the vibration isolation performance by measuring the dynamic stiffness of vibration isolators such as airmounts. On top of the setup a bellow can be used to either pull or press a force of 11000 N on the MF weight of 550 kg, resulting in a possible pre-tension force of approximately 5500 ± 11000 N on the object under test. It can be used to mimic the loaded operational situation of vibration isolation systems in an ASML machine. Note that the bellow can be attached underneath or on top of the frame to respectively press or pull an additional load.

The dynamic stiffness can be determined by exciting the shaker table and measuring the resulting forces and accelerations. The shaker table can be excited in the vertical direction by means of three piezo actuators underneath the shaker table and in horizontal direction by a shaker connected to the shaker table via a rod. To allow horizontal motion, the three piezos are removed and replaced by two leaf springs. During this thesis, however, only the vertical case with piezo excitation is considered.

The resulting forces are measured by three local 3 DOF force sensors which are mounted in between a base plate and an interface plate. This configuration is shown at the top in Figure 1.8a and is referred to as the force cell. The acceleration responses are measured with three 1 DOF accelerometers (for the z -direction) and one 3 DOF accelerometer (for the xy -directions) at both the BF and MF as respectively shown at the bottom in Figure 1.8a and at the top in Figure 1.8b.

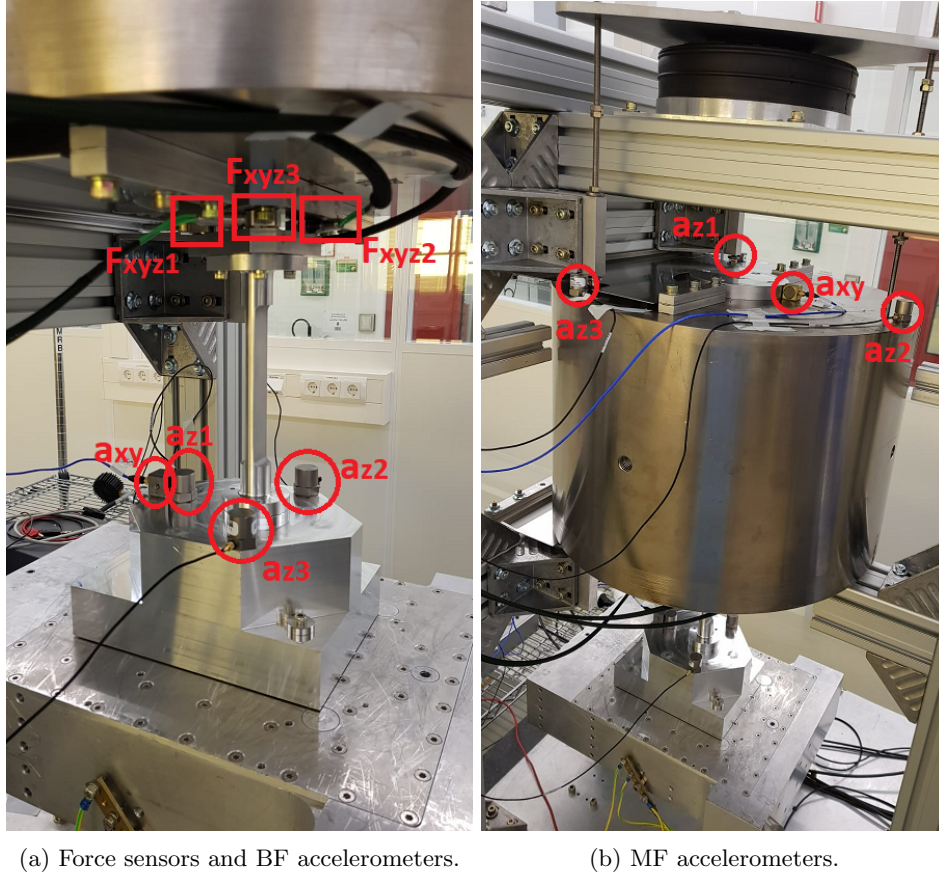


Figure 1.8: The force sensors and accelerometers used for dynamic stiffness measurements.

It can be seen that the force cell is mounted underneath the MF to directly measure the forces due to excitations transferred through the shaker table via the object under testing. In this case a reference test object is mounted in the setup, which is designed for the validation of the setup. A global 6 DOF force is determined by combining the three local 3 DOF force sensors. Also the individual acceleration responses in z -direction are combined to one global acceleration for both the BF and MF. Thereby rigid transformations are assumed while flexible internal behavior might occur which can influence the measurement. Moreover, the dynamic behavior of other components might also influence the measurement results. It is therefore desired to investigate the dynamic behavior of the setup in the frequency range of interest such that it can be validated and improved if necessary.

1.3 Problem definition and research goals

There is a continuous trend of microchips becoming cheaper and smaller due to shrink of the feature sizes on these chips. In lithography systems for fabrication of chips, it means a trend of tighter accuracy specs combined with increased excitation levels due to higher throughput. This creates a challenge for the vibration isolation systems within the ASML machines implying stricter requirements such as improvement of vibration isolation performance and isolation of higher payloads. Moreover, the frequency range of interest increases from 1 - 1000 Hz to 1 - 2000 Hz for which internal dynamics of isolators becomes more important.

A frequency dependent measure to characterize the isolation performance of these VISs is dynamic stiffness. In order to measure the dynamic stiffness of vibration isolation systems an experimental setup has been developed a few years ago. However, due to the stricter requirements on VISs there is a wish to further analyze and improve the test setup. It has also been found that during dynamic stiffness measurements the results are influenced by the dynamic behavior of the setup itself. This especially applies to the extended frequency range of interest where internal dynamic behavior starts to play a role. Such dynamic behavior might be problematic in the experimental characterization of vibration isolation performance by means of currently inexplicable resonance peaks in the measurement results. It is therefore desired to investigate and clarify the origin of these resonance peaks.

In conclusion, vibration isolation has to improve and it is required to fully understand the isolation behavior of VISs for a larger frequency range of interest of 1 - 2000 Hz. Therefore, full understanding of the dynamic behavior of the dynamic stiffness measurement setup itself is required as well. The main problem during this thesis is the fact that:

- The dynamic stiffness measurement setup is not comprehensively validated in the frequency range of interest of 1 - 2000 Hz resulting in lack of knowledge about its dynamic behavior influencing dynamic stiffness measurements.

It is, however, desired to know what part of the measured dynamic stiffness response originates from the object under test and what part from setup artifacts. Furthermore, the setup is currently not suitable for experiments regarding the stricter requirement of isolating higher payloads. Moreover, the suitability of the setup to perform accurate measurements on VISs for a greater frequency range of interest has yet to be determined. These research problems lead to the research goals.

As stated in the problem definition, the dynamic stiffness measurement setup is not comprehensively validated and lack of knowledge about its dynamic behavior is troublesome for accurate characterization of vibration isolation performance. Now there is a wish to further analyze and improve the test setup due to stricter requirements on vibration isolation systems. Therefore, the dynamic behavior of the setup itself has to be investigated. The purpose of this investigation is to gain better knowledge of the dynamic behavior of the setup such that the response from the object under test can be distinguished from setup artifacts in dynamic stiffness measurements. Hence, the main research goals of this thesis are to:

1. Validate the dynamic stiffness measurement setup by obtaining full knowledge of its dynamic behavior in the frequency range of interest of 1 - 2000 Hz.
2. Make a proposal for improvements of the dynamic stiffness measurement setup.

Reaching these goals is ultimately of great importance to correctly characterize the isolation performance of vibration isolation systems. Thus, in this thesis the research question is how the dynamic stiffness measurement setup can be comprehensively validated in order to obtain full knowledge of the dynamic behavior such that proposals for improvement can be made.

1.4 Thesis outline

Several steps are required in order to achieve the research goals and answer the research question. Initially, an introduction and the required theory behind modal analysis is elaborated in Chapter 2 for both numerical and experimental modal analysis. Afterwards, a test object to validate the dynamic stiffness measurement setup is designed according to specific requirements as elaborated in Chapter 3. This chapter also discusses numerical models and simulations of the test object and a lumped mass-spring model to approximate dynamic stiffness results and the influence of dynamic behavior of the setup. For this purpose numerical modal analysis is performed using the modal superposition method. Moreover, a finite element model is introduced which is yet to be updated with the experimental results in the next chapter. Subsequently, in Chapter 4 the results of experimental dynamic stiffness measurements and experimental modal analysis are investigated. These results are used to update the numerical models such that they can be used for reliable predictions. Also a discussion is given on these results. Lastly, conclusions and recommendations are given in Chapter 5 where proposals for improving the measurement setup are given.

Chapter 2

Modal analysis

Modal analysis is the study of the dynamic properties (eigenfrequencies, damping and mode shapes) of a mechanical structure under vibration using (estimated) frequency response functions (FRFs). These dynamic properties are required to achieve the desired design and control of the vibrations of structural components [8]. Modal analysis can be performed both numerically and experimentally, for which the required theory is elaborated in this chapter. Note that only linear systems are considered.

Numerical modal analysis is typically performed with a finite element model to predict the dynamic properties of (complex) structural systems. However, this numerical prediction contains inaccuracies due to the structural uncertainties and assumptions involved in the calculations. Experimental modal analysis can be used to update the numerical FE model since experimental results can be considered as (closest to) the true behavior of the mechanical structure. Model updating is mostly required to eventually validate the numerical model such that it can be used for cheap and accurate future studies rather than performing expensive and time consuming experimental modal testing over and over again.

2.1 Numerical modal analysis

A common method to predict or approximate the true behavior of a dynamic system is numerical modeling. A numerical model represents a simplification or approximation of a real-world system and consists of an underlying mathematical set of equations which can be solved. In this thesis the main interest is to obtain dynamic properties referring to modal analysis. Numerical modal analysis of simple linear dynamic systems is often performed using Newton's laws whereas finite element discretization is used for larger and geometrically more complex systems. A linear dynamic system with multiple DOFs can be described by the equations of motion defined as

$$\mathbf{M}\ddot{\underline{q}}(t) + \mathbf{G}\dot{\underline{q}}(t) + \mathbf{K}\underline{q}(t) = \underline{f}(t), \quad (2.1)$$

where $\mathbf{M}, \mathbf{G}, \mathbf{K} \in \mathbb{R}^{n \times n}$ are respectively the mass, (viscous) damping, and stiffness matrices with n the total number of DOFs, and $\underline{q}, \underline{f} \in \mathbb{R}^{n \times 1}$ are the physical DOFs and load/excitation columns, respectively.

There are two approaches to perform numerical modal analysis, namely the time domain approach and the frequency domain approach. In the time domain the governing differential equations are solved wherein the excitation is a function of time. In the frequency domain the excitation is discretized into a series of harmonic components and the dynamic response is expressed by superimposing the responses from each harmonic component. Due to the fact that understanding the behavior of the system is more intuitive and mathematical analysis is simplified in the frequency domain, the description of the system is usually converted from time domain to frequency domain with the Fourier transform. In case of harmonic response analysis the transfer from excitation to response in the frequency domain is expressed as

$$\mathbf{H}(\omega) = (-\omega^2\mathbf{M} + j\omega\mathbf{G} + \mathbf{K})^{-1}, \quad (2.2)$$

with ω [rad/s] the angular frequency, and $\mathbf{H}(\omega) \in \mathbb{C}^{n \times n}$ the FRF matrix [9]. Computation of the FRF matrix might however lead to excessive computation times if n is large and many frequency points need to be evaluated. Also note that the equations of motion as in (2.1) are coupled through the (non-diagonal) damping and stiffness matrices, hence the equations must be solved simultaneously. It is therefore desired to execute a model reduction technique to reduce the computation time. For this purpose a general approach in numerical modal analysis [10] is to:

1. Uncouple the equations of motion via coordinate transformation from the physical coordinate system to the modal coordinate system based on eigenmodes using the orthogonality property.
2. Perform dynamic analysis using only the uncoupled equations with eigenvalues and eigenmodes in the frequency range of interest.

This approach is known as the modal superposition method and solves n uncoupled equations, i.e. diagonal structural matrices, rather than solving a coupled system with n DOFs in the physical coordinate system.

2.1.1 Modal superposition

A powerful technique for reducing the computation time when performing dynamic response analysis of linear dynamic systems is the modal superposition method [10]. With this method the dynamic response of a structure can be approximated by superposition of the desired number of eigenmodes. A prerequisite for this technique is to solve the linear eigenvalue problem of the undamped homogeneous part of (2.1), namely

$$\mathbf{M}\ddot{\underline{q}}(t) + \mathbf{K}\underline{q}(t) = \underline{0}, \quad (2.3)$$

by assuming that $\underline{q}(t) = \underline{u}_k e^{\lambda_k t} = \underline{u}_k e^{j\omega_k t}$ is a solution. This results in the linear eigenvalue problem

$$(\lambda_k^2 \mathbf{M} + \mathbf{K}) \underline{u}_k = 0 \quad \text{with} \quad \lambda_k^2 = -\omega_k^2 \leq 0, \quad (2.4)$$

where $\lambda_{k\pm} = \pm j\omega_k = \pm 2\pi j f_k$ is the k^{th} eigenvalue (imaginary), ω_k [rad/s] the k^{th} angular eigenfrequency (real), f_k [Hz] the k^{th} eigenfrequency (real), and \underline{u}_k the k^{th} undamped eigenmode (real). In case of proportional or weak damping it is also sufficient to solve the undamped linear eigenvalue problem. The undamped eigenmodes are stored columnwise in the eigenmode matrix $\mathbf{U} \in \mathbb{R}^{n \times n}$ to define the coordinate transformation as

$$\underline{q}(t) = \mathbf{U}\underline{p}(t), \quad (2.5)$$

with $\underline{p} \in \mathbb{R}^{n \times 1}$ the modal DOFs column. Substitution of (2.5) in (2.1) and pre-multiplication by \mathbf{U}^T results in

$$\mathbf{U}^T \mathbf{M} \mathbf{U} \ddot{\underline{p}}(t) + \mathbf{U}^T \mathbf{G} \mathbf{U} \dot{\underline{p}}(t) + \mathbf{U}^T \mathbf{K} \mathbf{U} \underline{p}(t) = \mathbf{U}^T \underline{f}(t). \quad (2.6)$$

With the orthogonality property

$$\underline{u}_i^T \underline{u}_j = \begin{cases} 1, & i = j \\ 0, & i \neq j, \end{cases} \quad (2.7)$$

and assuming weak or proportional damping it can be shown that the structural matrices in the modal coordinate system defined as

$$\bar{\mathbf{M}} = \mathbf{U}^T \mathbf{M} \mathbf{U}, \quad (2.8)$$

$$\bar{\mathbf{G}} = \mathbf{U}^T \mathbf{G} \mathbf{U}, \quad (2.9)$$

$$\bar{\mathbf{K}} = \mathbf{U}^T \mathbf{K} \mathbf{U}, \quad (2.10)$$

are diagonal with respectively modal masses \bar{m}_k , modal damping $\bar{g}_k = 2\bar{m}_k \xi_k \omega_k$ with ξ_k a dimensionless modal damping factor for mode k , and modal stiffness $\bar{k}_k = \bar{m}_k \omega_k^2$ on the diagonal such that uncoupling is satisfied. The eigenmodes are often mass normalized such that

$$\bar{\mathbf{M}} = \mathbf{I}, \quad (2.11)$$

$$\bar{\mathbf{G}} = 2\bar{\boldsymbol{\Xi}}\bar{\boldsymbol{\Omega}}, \quad (2.12)$$

$$\bar{\mathbf{K}} = \bar{\boldsymbol{\Omega}}^2, \quad (2.13)$$

with $\Xi \in \mathbb{R}^{n \times n}$ a diagonal matrix with dimensionless modal damping factors ξ_k , and $\Omega \in \mathbb{R}^{n \times n}$ the diagonal eigenfrequency matrix with angular eigenfrequencies ω_k on the diagonal. This results in the uncoupled proportionally damped equations of motion:

$$\mathbf{I}\ddot{\underline{p}}(t) + 2\Xi\Omega\dot{\underline{p}}(t) + \Omega^2\underline{p}(t) = \mathbf{U}^T \underline{f}(t). \quad (2.14)$$

Consider the general case where eigenmodes are not scaled by mass normalization. Then for harmonic excitation and response the FRF matrix of the proportionally damped system results in

$$\mathbf{H}(\omega) = \mathbf{U} (-\omega^2 \bar{\mathbf{M}} + j\omega \bar{\mathbf{G}} + \bar{\mathbf{K}})^{-1} \mathbf{U}^T \quad (2.15)$$

$$= \sum_{k=1}^n \frac{u_k u_k^T}{\bar{m}_k (-\omega^2 + 2j\omega \xi_k \omega_k^2 + \omega_k^2)} \quad (2.16)$$

$$\approx \sum_{k=1}^{n_m} \frac{u_k u_k^T}{\bar{m}_k (-\omega^2 + 2j\omega \xi_k \omega_k^2 + \omega_k^2)}, \quad (2.17)$$

with $n_m < n$ the desired number of modes. The accuracy of the approximation increases by taking more modes into account, but the computation time increases as well. One should therefore not take more modes into account than necessary. For the case where eigenmodes are scaled by mass normalization the FRF matrix results in

$$\mathbf{H}(\omega) = \mathbf{U} (-\omega^2 \mathbf{I} + 2j\omega \Xi \Omega + \Omega^2)^{-1} \mathbf{U}^T \quad (2.18)$$

$$= \sum_{k=1}^n \frac{u_k u_k^T}{-\omega^2 + 2j\omega \xi_k \omega_k^2 + \omega_k^2} \quad (2.19)$$

$$\approx \sum_{k=1}^{n_m} \frac{u_k u_k^T}{-\omega^2 + 2j\omega \xi_k \omega_k^2 + \omega_k^2}. \quad (2.20)$$

In conclusion, the modal superposition method is a commonly used model order reduction technique in numerical modal analysis. It approximates the dynamic behavior by superposition of a desired number of modes and can be applied to simple linear dynamic systems as well as geometrically more complex systems using the finite element method (FEM). A larger number of modes taken into account results in a more accurate approximation yet larger computation costs. Validation of the numerical modal analysis results is typically performed with experimental modal analysis results.

2.2 Experimental modal analysis

It is mentioned before that EMA can be performed to obtain the dynamic properties closest to the true representation of the considered structure. These results are used to update the numerical model such that it can be validated and used for cheap and quick future studies. In such analysis it is assumed that the dynamic system is linear. An excitation source is applied to the mechanical structure in order to make it vibrate. Two main excitation principles are therefore used: a shaker connected to the structure via a force transducer or a modal hammer (impact) excitation with a force transducer head. The input excitation signals and the resulting output response signals are measured to estimate the FRFs. The experimental results are considered as the true behavior of the mechanical structure, while the numerical results obtained with the FEM are typically regarded as less accurate due to structural uncertainties and corresponding assumptions. Therefore, EMA results can be used as reference for comparison with NMA results. Based on this comparison the accuracy of the numerical model can eventually be improved by model updating. The basic approach to perform EMA can be summarized in five steps [10]:

1. Collect suitable experimental data in the time domain.
2. Apply the Fourier Transform to the time domain data collected during step 1.
3. Use random (statistical) processes to determine the probability of the occurrence of particular amplitudes in non-deterministic signals.

4. Apply system identification to estimate a possible linear relation between the input and output signals based on characteristic quantities for random processes.
5. Apply a modal parameter estimation procedure to estimate the dynamic properties.

The elaborated theory on EMA is based on these five steps.

2.2.1 Experimental data

The first step in EMA is to gather suitable experimental data. The mechanical structure of interest is therefore excited with a shaker or modal hammer and the resulting excitation signals $x(t_k)$ and response signals $y(t_k)$ as function of time are measured at each time step t_k . The analogue signals from the sensors are fed into data acquisition systems to initially condition the signals with an anti-aliasing filter and secondly digitize the signals with an analogue digital converter. The digital signals can thereafter be further processed. Two potential signal processing problems are noise and signal leakage and can be compensated for by using averaging and windowing techniques. For this purpose different methods are used depending on the source of excitation.

2.2.1.1 Shaker excitation

In case of shaker excitation a white noise or frequency sine sweep (multisine) signal is sent to the shaker for which the bandwidth is determined by the sample frequency and the measurement time. The random (non-periodic) time data obtained during shaker excitation is divided into a number of data blocks. Signal leakage is minimized by applying a window to each data block to force the data to better satisfy the periodicity requirement of the Fast Fourier transform (FFT) process. For this purpose a Hanning window is applied to each data block enforcing the beginning and end to be zero wherefor an example is shown in Figures 2.1a and 2.1b. After application of the FFT to the windowed signals, the frequency domain data can be averaged to reduce the effect of measurement noise resulting in smoother FRFs.

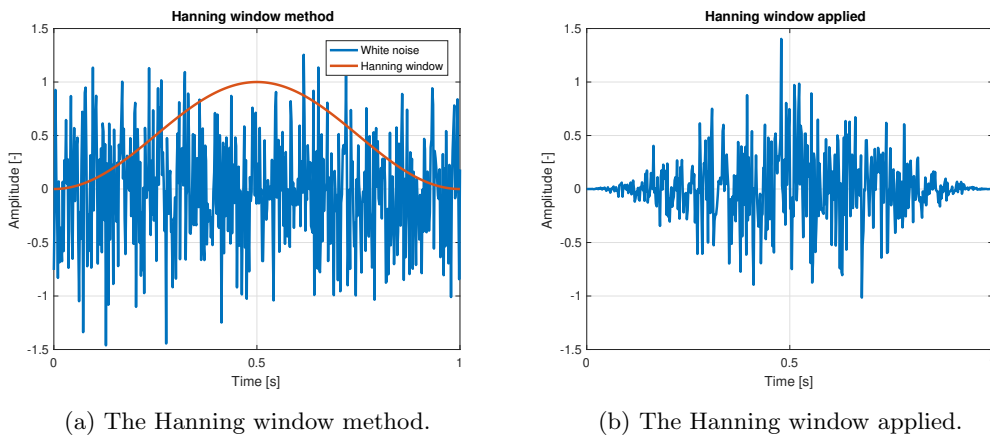


Figure 2.1: The effect of using a Hanning window.

2.2.1.2 Modal hammer excitation

In case of modal hammer excitation the signal is in principle a Dirac function where all frequencies are distributed with a uniform amplitude. In practice however the bandwidth is limited by the material of the hammer head and the mass of the hammer, i.e. the harder the head the shorter the pulse duration and thus the higher the frequency content. During modal hammer excitation the force pulse is usually relatively short compared to the length of the time record, hence the portion of signal after the pulse plus the oscillation at the end of the pulse is noise and can be eliminated with a rectangular window. An example of applying the rectangular window is shown in Figures 2.2a and 2.2b. Note that a short pre-trigger length is applied before the impulse response.

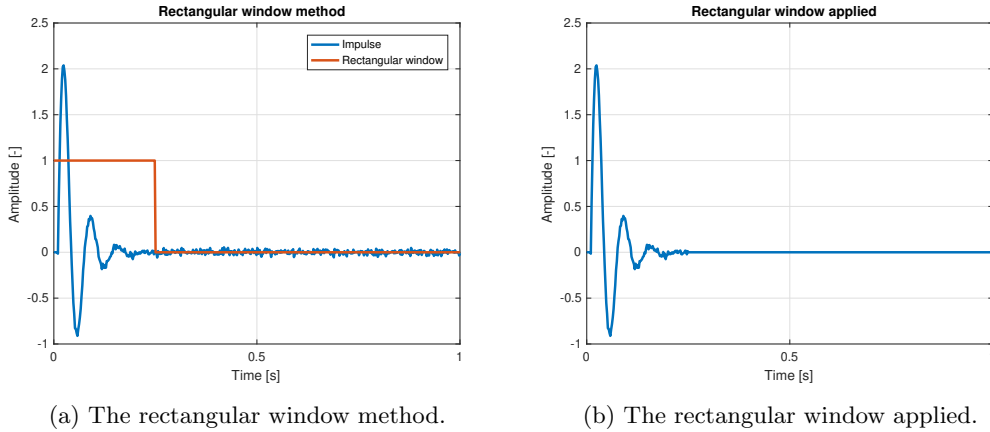


Figure 2.2: The effect of using a rectangular window.

The response signal is an exponential decaying function and depending on the damping it decays out before or after the measurement frame. An exponential window is used to minimize leakage by forcing the response to decay out in the measurement frame such that it better satisfies the periodicity requirement of the FFT process. An example of applying the exponential window is shown in Figures 2.3a and 2.3b. In this case one should realize that additional (numerical) damping has been introduced which should be taken into account.

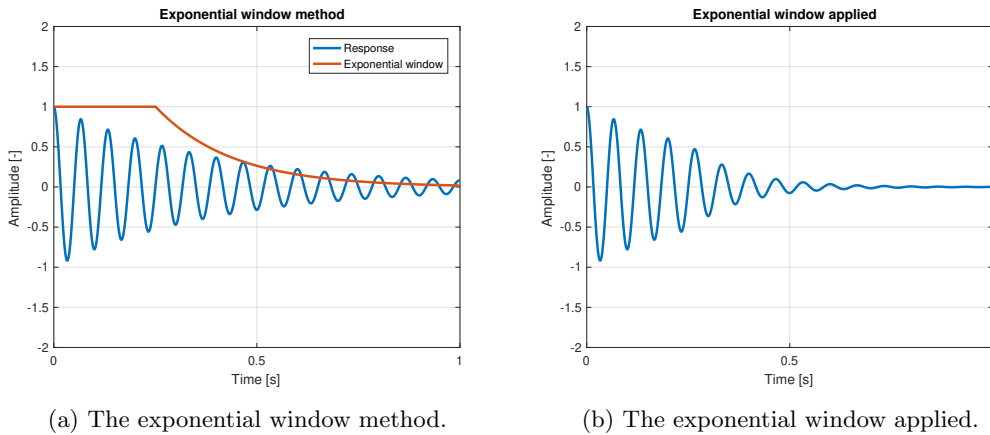


Figure 2.3: The effect of using an exponential window.

A last important feature during hammer modal analysis is that multiple impacts are performed for averaging to reduce the effect of random noise resulting in smoother FRFs.

2.2.2 Fourier transformation

In order to make life easier during modal analysis, the (Fast) Fourier transform is used to convert the obtained time signals to a representation in the frequency domain. In other words, the Fourier transform decomposes the time signals in its harmonic components to simplify modal analysis by representing the dynamic behavior of a mechanical structure with FRFs. For pure periodic signals where $x(t) = x(t + T)$ with T the minimal period time of the signal, the complex form of the Fourier series can be written as

$$x(t) = \sum_{n=-\infty}^{\infty} c_n e^{2\pi f_n t j} \quad \text{with} \quad c_n = \frac{1}{T} \int_0^T x(t) e^{-2\pi f_n t j} dt \quad \text{for} \quad n \in \mathbb{Z}. \quad (2.21)$$

Here the (complex) Fourier coefficients c_n determine the contribution of each harmonic component, i.e. $e^{2\pi f_n t j} = \cos(2\pi f_n t) + j \sin(2\pi f_n t)$ with $f_n = \frac{n}{T}$, to the signal $x(t)$. However, there is a property

of the Fourier transform that affects the energy distribution in the frequency domain known as signal leakage. It is the result of the physical limitation of measuring a complete representation of the data for infinite time along with the periodicity assumption of each time data block required by the Fourier transform [11][12]. In practice one measures non-periodic signals (white noise or an impulse response) for which the Fourier integral requires the measurement (period) time to approach infinity, i.e. $T \rightarrow \infty$. The Fourier transform of a non-periodic signal $x(t)$ is defined as

$$X(f) = F[x(t)] = \int_{t=-\infty}^{\infty} x(t)e^{-2\pi ftj} dt, \quad (2.22)$$

and the inverse Fourier transform is defined as

$$x(t) = F^{-1}[X(f)] = \int_{f=-\infty}^{\infty} X(f)e^{2\pi ftj} df. \quad (2.23)$$

If the signal $x(t)$ is periodic, the Fourier integral can be evaluated over a finite time interval rather than an infinite time interval. Therefore windowing techniques are used to satisfy the periodicity requirement as explained before. The windowed signal $x_w(t_k)$ is digitized such that

$$x_w(t_k) = x_w(k\Delta T) \quad \text{in } 0 \leq t < T \quad \text{for } k = 0, 1, \dots, N-1, \quad (2.24)$$

with N the number of samples and sample time $\Delta T = \frac{T}{N}$. Now the discrete approximation of the Fourier integral is determined with

$$X(f) = \int_{t=-\infty}^{\infty} x(t)e^{-2\pi ftj} dt \approx \sum_{k=0}^{N-1} x_w(k\Delta T)e^{-2\pi fj k\Delta T} \Delta T, \quad (2.25)$$

which should only be evaluated at discrete values $f_n = \frac{n}{T}$ with $n \in \mathbb{Z}$. As a result the Discrete Fourier transform (DFT) can be defined as

$$X(f_n) = \Delta T \sum_{k=0}^{N-1} x_w(k\Delta T)e^{-2\pi jkn \frac{\Delta T}{T}} = \Delta T \sum_{k=0}^{N-1} x_w(k\Delta T)e^{-2\pi j \frac{kn}{N}} \quad \text{with } n \in \mathbb{Z}, \quad (2.26)$$

such that it is periodic with sample frequency $f_N = \frac{N}{T}$. Therefore it only makes sense to evaluate the DFT for N discrete frequencies such that

$$X(f_n) = \Delta T \sum_{k=0}^{N-1} x_w(k\Delta T)e^{-2\pi j \frac{kn}{N}} \quad \text{with } n = 0, 1, \dots, N-1. \quad (2.27)$$

However, computing the DFT can be practically slow for large N and a solution to this problem is to apply a FFT algorithm. Computing the DFT directly requires $\mathcal{O}(N^2)$ operations whereas the FFT requires only $\mathcal{O}(N \log_2 N)$ operations. The algorithm is explained in [10] and is beyond the scope of this study.

The practical application of the FFT comes with two error sources: signal leakage due to non-periodic signals and aliasing due to a limited number of discrete values taken into account, i.e. sample frequency being too small. The first problem is solved with windowing techniques to reduce edge discontinuities whereas aliasing can be avoided by choosing the Nyquist frequency (half the sample frequency) larger than the maximum frequency in the signal such that

$$f_{Nyquist} = \frac{f_s}{2} = \frac{1}{2\Delta T} > f_{max}. \quad (2.28)$$

In practice f_{max} is usually unknown and very high, so high frequency components in the signal need to be removed by (low pass) filtering. Note that the factor 2 applies in theory whereas in practice this should be a factor of 5-10 in order to perform proper measurements. A reason for that is to restrain the influence of measurement noise, since measuring more samples gives more accurate results.

The signals discussed so far are assumed to be deterministic. However, in practice signals are often non-deterministic (random processes) such that exact values at a certain time are unknown. By averaging these signals the statistical characteristics can be determined.

2.2.3 Random processes

An efficient way of dealing with random vibrations is to use a statistical process to determine the probability of the occurrence of particular amplitudes. In this type of approach, the random vibration can be characterized using a mean, the standard deviation and a probability density function [13]. By considering a random signal $x(t)$ the time averages of the mean μ_x , the mean square value ψ_x^2 and the standard deviation σ_x , hence therewith the variance σ_x^2 , are determined as:

$$\mu_x = E[x(t)] = \lim_{T \rightarrow \infty} \frac{1}{T} \int_0^T x(t) dt, \quad (2.29)$$

$$\psi_x^2 = E[x^2(t)] = \lim_{T \rightarrow \infty} \frac{1}{T} \int_0^T x^2(t) dt, \quad (2.30)$$

$$\sigma_x = E[(x(t) - \mu_x)] = \lim_{T \rightarrow \infty} \frac{1}{T} \int_0^T (x(t) - \mu_x) dt. \quad (2.31)$$

Most random processes follow a Gaussian (normal) probability density function describing the probability of the random variable reaching a certain amplitude in small frequency segments and is defined as

$$p(x) = \frac{1}{\sigma\sqrt{2\pi}} e^{-\frac{(x-\mu)^2}{2\sigma^2}}. \quad (2.32)$$

Note that the Gaussian probability density function $p(x)$ does not indicate the frequency content of the random signal. For this purpose the power spectral density (PSD) is used, which is a measure for the power intensity of a random process in the frequency domain. The time series $x(t)$ is therefore windowed to signal $x_w(t) = w(t)x(t)$ in order to compute the Fourier transform to determine the PSD. The mean square value (mean power) of $x_w(t)$ is related to the auto PSD using the (inverse) Fourier transform such that

$$\begin{aligned} \psi_x^2 &= E[x_w^2(t)] = \frac{1}{T} \int_0^T x_w^2(t) dt = \frac{1}{T} \int_{-\infty}^{\infty} x_w^2(t) dt \\ &= \frac{1}{T} \int_{t=-\infty}^{\infty} \left[x_w(t) \int_{f=-\infty}^{\infty} X_w(f) e^{2\pi f t j} \right] dt \\ &= \frac{1}{T} \int_{f=-\infty}^{\infty} X_w(f) \left[\int_{t=-\infty}^{\infty} x_w(t) e^{2\pi f t j} dt \right] df \\ &= \int_{f=-\infty}^{\infty} \frac{1}{T} X_w(f) X_w^*(f) df \\ &= \int_{f=-\infty}^{\infty} S_{xx}(f) df, \end{aligned} \quad (2.33)$$

with the asterisk in $X_w^*(f)$ indicating the complex conjugate of $X_w(f)$, and the two sided auto PSD function of the windowed excitation signal $x_w(t)$ is defined as

$$S_{xx}(f) = \frac{1}{T} X_w^*(f) X_w(f) = \frac{1}{T} |X_w(f)|^2. \quad (2.34)$$

The auto PSD corresponding to a random process is a random process itself and requires averaging over a number of data blocks. Since the auto PSD S_{xx} is independent of a time shift t_0 in the time signal, i.e. $x(t - t_0)$, it does not have any phase information and can accurately be estimated as

$$\hat{S}_{xx}(f) = \frac{1}{N_b T} \sum_{k=1}^{N_b} [X_{w,k}^*(f) X_{w,k}(f)], \quad (2.35)$$

with N_b the number of data blocks over which the random process is averaged. This does not hold for the linear FFT $X_w(f)$ whereby averaging is problematic due to the phase shift.

In a same way as the auto PSD, the cross PSD describing the coherence between the excitation signal and the response signal for frequency f can be determined. The cross PSD results in

$$S_{xy}(f) = \frac{1}{T} X_w^*(f) Y_w(f), \quad (2.36)$$

which can be estimated as

$$\hat{S}_{xy}(f) = \frac{1}{N_b T} \sum_{k=1}^{N_b} [X_{w,k}^*(f) Y_{w,k}(f)]. \quad (2.37)$$

In contrast to the real auto PSD S_{xx} , the cross PSD S_{xy} is complex and does contain phase information. Now the auto and cross PSDs are used for system identification, i.e. the estimation of relations between the input and output, such that FRFs of the system can be estimated.

2.2.4 System identification

In dynamic analysis it is important to estimate a possible linear relation between input and output signals based on characteristic quantities for random processes. This process of estimating the dynamic behavior of a dynamical system with statistical methods is known as system identification. The response of the system without disturbances in the frequency domain is defined as

$$Y(f) = H_{xy}(f)X(f), \quad (2.38)$$

with H_{xy} the FRF of the system and $X(f)$ the FFT of the time signal $x(t)$. The linear FFTs are problematic for averaging as mentioned before. Therefore, the auto and cross PSDs are used such that system identification can be performed by estimating the FRFs depending on the type of noise with

$$\hat{H}_1(f) = \frac{\hat{S}_{xy}(f)}{\hat{S}_{xx}(f)}, \quad (2.39)$$

$$\hat{H}_2(f) = \frac{\hat{S}_{yy}(f)}{\hat{S}_{yx}(f)}. \quad (2.40)$$

The \hat{H}_1 estimator is superior near anti-resonances and minimizes the output noise being statistically independent from $x(t)$ and the input noise which goes through the system and is statistically independent from $x(t)$ as well. The \hat{H}_2 estimator is superior near resonances and minimizes the input noise which does not go through the system and is not statistically independent from $x(t)$. It can moreover be shown as elaborated in [10] that

$$\left| \hat{S}_{xy}(f) \right|^2 \leq \hat{S}_{xx}(f) \hat{S}_{yy}(f) \quad \text{for } T \rightarrow \infty, \quad (2.41)$$

which results in the coherence function estimated as

$$\hat{\gamma}_{xy}^2(f) = \frac{\left| \hat{S}_{xy}(f) \right|^2}{\hat{S}_{xx}(f) \hat{S}_{yy}(f)} = \frac{\hat{H}_1(f)}{\hat{H}_2(f)} \quad \text{with } 0 \leq \hat{\gamma}_{xy}^2(f) \leq 1. \quad (2.42)$$

The coherence estimator is used in order to verify the measurement quality. It tells for each frequency which part of the output comes from the input and which part from the output noise. For $\hat{\gamma}_{xy}^2(f) \rightarrow 1$ the FRF estimators \hat{H}_1 and \hat{H}_2 are equal and there is a strong linear relation between input and output indicating a good measurement quality. In case of $\hat{\gamma}_{xy}^2(f) \rightarrow 0$ the FRF estimators are different and output is dominated by noise and/or a nonlinear relation such that there is no relation between input and output indicating a poor measurement quality. Now that the FRFs of the experimental data are estimated, modal parameter fit procedures are used to determine the dynamic properties of the system.

2.2.5 Modal parameter estimation

The final step is to estimate the modal parameters (eigenfrequencies, damping and mode shapes) from the measured set of FRFs. A common numerical tool in processing experimental data is the complex mode indicator function (CMIF) and is used to estimate the number of interesting modes and the corresponding (eigen)frequencies and mode shapes. The CMIF is an algorithm based on

singular value decomposition (SVD) applied to (multiple) reference FRF measurements to identify the amount of (significant) eigenvalues in each individual spectral line of the FRF matrix [14][15]. In other words, the CMIF actually determines the existence of significant operational deflection shapes (ODSs) which might indicate a mode and the relative magnitude of each mode or ODS. Note that an ODS is not a real mode shape, but it might represent or look like a mode shape. Most CMIF approaches use an economical approach such that the number of spectral lines is equal to the smallest number, either the number of inputs or the number of outputs. By taking the SVD of the FRF matrix it can be decomposed as

$$\mathbf{H}(f) = \mathbf{U}(f)\mathbf{\Sigma}(f)\mathbf{V}(f)^H, \quad (2.43)$$

with $\mathbf{U}(f)$ the real valued left hand eigenvector matrix, $\mathbf{\Sigma}(f)$ the (complex) singular value matrix containing spectral lines, and $\mathbf{V}(f)$ the real valued right hand eigenvector matrix where the superscript H indicates the Hermitian transpose. The imaginary part of the FRF matrix is used in the SVD approach to compute the CMIF. This imaginary method will result in real valued rather than complex singular vectors and a better representation of neighbouring modes for acceleration over force. In conclusion, the measured FRFs are used to estimate the modal parameters with the CMIF approach by means of a SVD.

The obtained singular values can be plotted as a function of frequency known as the CMIF plot of a spectral line, which indicates interesting phenomena as peaks and the height of each peak indicates its importance. The corresponding frequencies of these peaks give an estimate for the (damped) eigenfrequencies of each mode/ODS within the accuracy of the frequency resolution. Note that not all peaks in the CMIF plot identify modes, because errors such as noise and leakage can also generate a peak. Furthermore, CMIF spectral lines are arranged from largest to smallest. For increasing frequencies it is thus possible that another mode/ODS becomes dominant. When this happens the mode/ODS will take over the highest spectral line and peaks visible in the lower CMIFs may therefore often indicate such a takeover rather than an actual resonance peak.

A method to compare modes is the modal assurance criterion (MAC), which gives the degree of correlation between two modes/ODS. The MAC values can be computed with

$$MAC = \frac{|u_{1,i}^H u_{2,j}|^2}{(u_{1,i}^H u_{1,i})(u_{2,j}^H u_{2,j})}, \quad (2.44)$$

which shows the similarity between two modes/ODSs and helps to verify whether the correct modes/ODSs from the CMIF are chosen. The MAC value varies between 0 and 1, i.e. $0 \leq MAC \leq 1$, and for identical modes/ODSs the MAC value reaches 1. This value decreases significantly when modes/ODSs are not similar. Since the MAC is calculated from one to another ODS, a square matrix is calculated. The MAC value will be 1 for a mode or ODS compared to itself. Now this concludes the required theory throughout this thesis to perform modal analysis.

2.3 Summary

This chapter gives an introduction on modal analysis of linear dynamic systems. The required theory for both numerical and experimental modal analysis is elaborated. First, the general numerical modal analysis method is introduced after which the modal superposition method is explained. In this part only undamped and weakly/proportionally damped systems are considered which suffices for the numerical models in this thesis. Subsequently, the required theory on experimental modal analysis is elaborated based on five steps and will be applied during the executed modal analyses in this research. In the sequel of this thesis numerical modal analysis are performed initially as elaborated in Chapter 3 and validated with experimental modal analysis and experimental measurement results as elaborated in Chapter 4.

Chapter 3

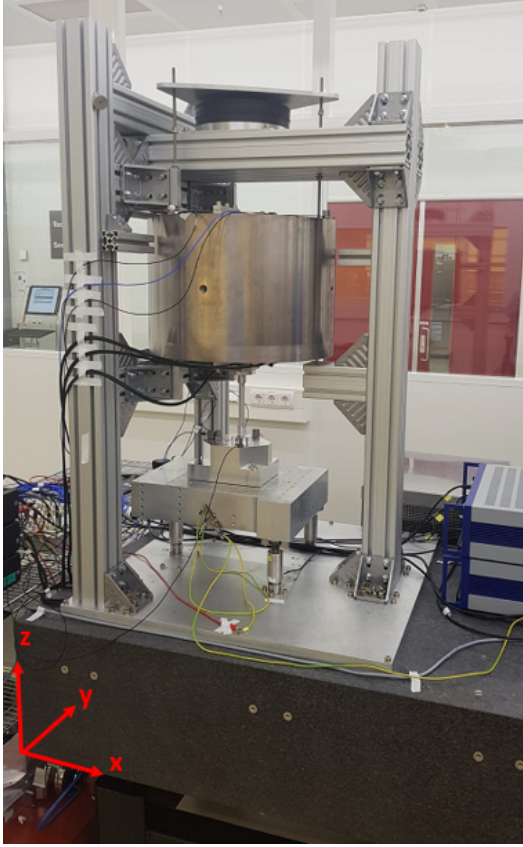
Experimental setup and test object modeling

A widely used tool in engineering design and analysis is numerical modeling. It can be defined as the process of solving physical problems by appropriate simplification of reality. For this purpose a (complex) mathematical model should be constructed which represents a simplified yet accurate representation of the physical problem. With the development of efficient computational technologies these complex mathematical models can be solved numerically. Thereby engineering design optimization and analysis can be performed numerically in a cheap and time efficient manner rather than executing costly and time consuming practical experiments.

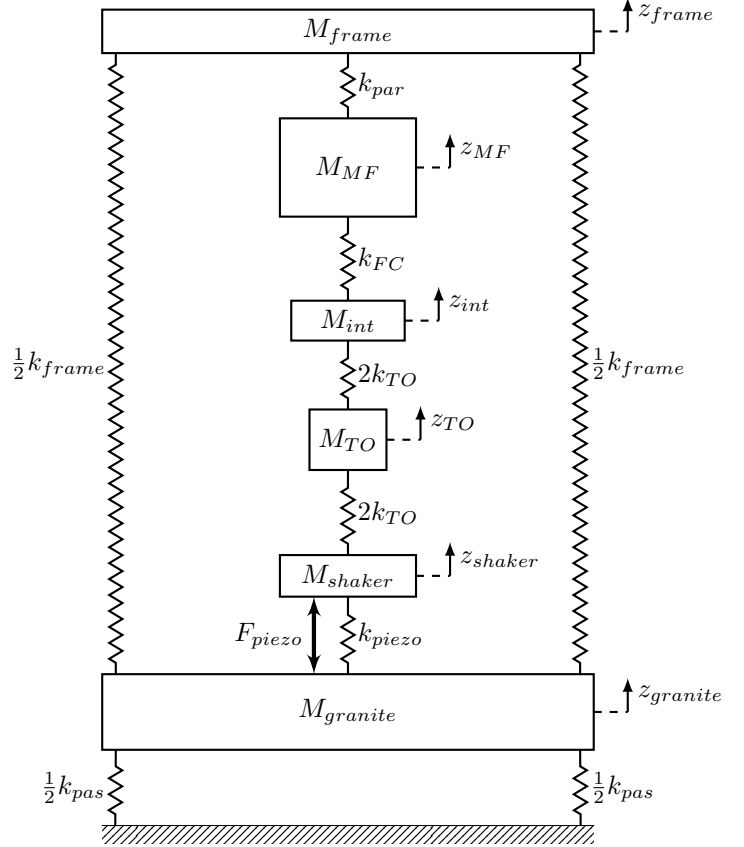
In this chapter a 1-dimensional lumped mass-spring model of the setup is constructed to perform initial predictions of the dynamic stiffness during actual measurements. Afterwards, the design and analysis of the test object intended for validation of the dynamic stiffness measurement setup is elaborated. The numerical model of this test object is validated with the aid of experimental modal analysis results. In order to perform more realistic simulations of the actual dynamic stiffness measurements and to investigate the dynamic behavior of the setup, a 3-dimensional finite element model has been made. The FE model will be updated with the obtained experimental data for which the results are elaborated later on in Chapter 4.

3.1 Lumped mass-spring model

A 1-dimensional lumped mass-spring model of the setup has been made including the most important parts. The actual setup is shown again in Figure 3.1a and the lumped mass-spring model is schematically visualized in Figure 3.1b. In this model only the vertical displacements in z -direction are considered. Note that the granite stone with mass $M_{granite}$ is passively isolated from floor vibrations by k_{pas} . On top it contains three piezo actuators with a combined stiffness k_{piezo} , which deliver a positive force F_{piezo} to the shaker table with mass M_{shaker} and a negative force F_{piezo} to the granite stone. The object under test (TO) with total stiffness k_{TO} and mass M_{TO} is positioned on top of the shaker table and is attached at the top to the force cell interface with mass M_{int} . The stiffness of the force cell (FC) is indicated with k_{FC} and is attached to the metrology frame (MF) with mass M_{MF} . The metrology frame is attached to the support frame by M8 threaded rods via a bellow plate and a bellow with combined stiffness k_{par} which cause forces parallel to the test object getting translated to the support frame with mass M_{frame} . These forces are also known as parasitic forces. The support frame is attached to the granite stone with total stiffness k_{frame} .



(a) The dynamic stiffness measurement setup.



(b) Lumped mass-spring model.

Figure 3.1: The actual setup and a lumped mass-spring model.

A modal analysis is performed with this model to investigate the effect of structural dynamics of the setup on the dynamic stiffness of the object under test. For this purpose the equations of motion of the system are generally formulated as

$$\underline{F}(t) = \underline{M}\ddot{\underline{z}}(t) + \underline{G}\dot{\underline{z}}(t) + \underline{K}\underline{z}(t), \quad (3.1)$$

where $\underline{F} \in \mathbb{R}^{n \times 1}$ contains the forces acting on the system, $\underline{M}, \underline{G}, \underline{K} \in \mathbb{R}^{n \times n}$ respectively the mass, damping, and stiffness matrices. For the undamped model as in Figure 3.1b this results in

$$\begin{aligned} -F_{piezo} &= M_{granite}\ddot{z}_{granite} + (k_{pas} + k_{piezo})z_{granite} - k_{piezo}z_{shaker} - k_{frame}z_{frame}, \\ F_{piezo} &= M_{shaker}\ddot{z}_{shaker} + (k_{piezo} + 2k_{TO})z_{shaker} - k_{piezo}z_{granite} - 2k_{TO}z_{TO}, \\ 0 &= M_{TO}\ddot{z}_{TO} + (2k_{TO} + 2k_{TO})z_{TO} - 2k_{TO}z_{shaker} - 2k_{TO}z_{int}, \\ 0 &= M_{int}\ddot{z}_{int} + (2k_{TO} + k_{FC})z_{int} - 2k_{TO}z_{TO} - k_{FC}z_{MF}, \\ 0 &= M_{MF}\ddot{z}_{MF} + (k_{FC} + k_{par})z_{MF} - k_{FC}z_{int} - k_{par}z_{frame}, \\ 0 &= M_{frame}\ddot{z}_{frame} + (k_{par} + k_{frame})z_{frame} - k_{frame}z_{granite} - k_{par}z_{MF}, \end{aligned} \quad (3.2)$$

which can be written in matrix form as

$$\begin{bmatrix} -F_{piezo} \\ F_{piezo} \\ 0 \\ 0 \\ 0 \\ 0 \end{bmatrix} = \begin{bmatrix} M_{granite} & 0 & 0 & 0 & 0 & 0 \\ 0 & M_{shaker} & 0 & 0 & 0 & 0 \\ 0 & 0 & M_{TO} & 0 & 0 & 0 \\ 0 & 0 & 0 & M_{int} & 0 & 0 \\ 0 & 0 & 0 & 0 & M_{MF} & 0 \\ 0 & 0 & 0 & 0 & 0 & M_{frame} \end{bmatrix} \begin{bmatrix} \ddot{z}_{granite} \\ \ddot{z}_{shaker} \\ \ddot{z}_{TO} \\ \ddot{z}_{int} \\ \ddot{z}_{MF} \\ \ddot{z}_{frame} \end{bmatrix} + \begin{bmatrix} k_{pas} + k_{piezo} & -k_{piezo} & 0 & 0 & 0 & -k_{frame} \\ -k_{piezo} & k_{piezo} + 2k_{TO} & -2k_{TO} & 0 & 0 & 0 \\ 0 & -2k_{TO} & 4k_{TO} & -2k_{TO} & 0 & 0 \\ 0 & 0 & -2k_{TO} & 2k_{TO} + k_{FC} & -k_{FC} & 0 \\ 0 & 0 & 0 & -k_{FC} & k_{FC} + k_{par} & -k_{par} \\ -k_{frame} & 0 & 0 & 0 & -k_{par} & k_{par} + k_{frame} \end{bmatrix} \begin{bmatrix} z_{granite} \\ z_{shaker} \\ z_{TO} \\ z_{int} \\ z_{MF} \\ z_{frame} \end{bmatrix}.$$

With these equations of motion the dynamic stiffness of the test object can eventually be predicted.

3.1.1 Dynamic stiffness

Investigation of the influence of dynamic behavior of the setup on the dynamic stiffness of the object under test is performed with system identification. It uses input and output signal measurements to build a mathematical model of the system. Therefore, piezo force input signals $x(t)$ are used to generate the output displacement signals $y(t)$ with the known system. In this case these signals have 5 million time points, sampled with a time increment of $\Delta t = 2 \cdot 10^{-5}$ seconds hence a sample frequency of $f_s = 50$ kHz and total measurement time of 100 seconds. These time signals are divided into 20 data blocks with 50% overlap. Afterwards, a Hanning window is applied to each data block after which the FFT is computed. Thereafter, the auto PSD and cross PSD estimators are determined in order to estimate the FRF. The transfer from displacement to force is investigated to predict the dynamic stiffness of the object under test and to imitate actual measurements. The dynamic stiffness of the test object can be determined with

$$k_{dyn} = \frac{F_{FC}}{z_{MF} - z_{shaker}}, \quad (3.3)$$

in which

$$F_{FC} = k_{FC} \cdot (z_{MF} - z_{int}), \quad (3.4)$$

where z are the computed output displacements $y(t)$ as result of the piezo force input signals $x(t)$, and k_{FC} is the known force cell stiffness. The new input is a relative displacement, i.e. $x(t) = z_{MF} - z_{shaker}$, and the new output is a force, i.e. $y(t) = F_{FC} = k_{FC} \cdot (z_{MF} - z_{int})$, to determine the dynamic stiffness of the test object. A relative displacement is used instead of only shaker table displacement to get rid of the low frequency MF dynamic behavior. The resulting dynamic stiffness of the test object with 1% damping is shown in Figure 3.2. A white noise piezo input force on the shaker table and an opposite white noise piezo input force on the granite stone are used resulting in output displacements. These output displacements are used to compute the new input $x(t) = z_{MF} - z_{shaker}$ and output $y(t) = F_{FC}$ to determine the dynamic stiffness of the test object.

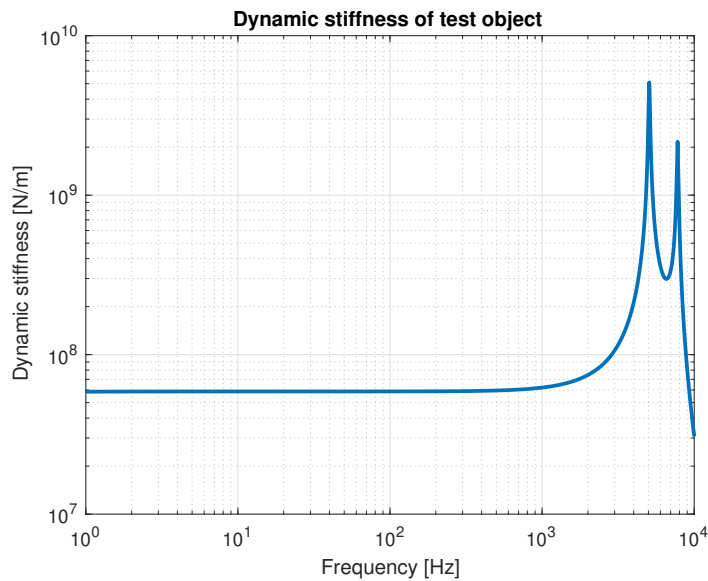


Figure 3.2: The dynamic stiffness of the test object.

Note that the static stiffness has a value of approximately $6 \cdot 10^7$ N/m. This corresponds to the axial static stiffness of the test object used throughout this project as elaborated in Section 3.2. Two resonance peaks can be seen in the dynamic stiffness of the test object. The first peak originates from the force cell resonance and the second peak is caused by the axial mode of the test object. In order to obtain more realistic predictions of the influence of the dynamic behavior of the setup a 3-dimensional finite element model is made and introduced in Section 3.4. Prior to that, the design and analysis of the test object intended for validation of the dynamic stiffness measurement setup is elaborated.

3.2 Test object

For the validation of the dynamic stiffness measurement setup in the frequency range of interest (1 - 2000 Hz) a test object has been designed according to the following requirements:

- A design with an eigenfrequency of its first eigenmode above 2000 Hz plus a margin of approximately 10%, such that resonance behavior in the frequency range of interest comes from the test setup itself.
- The top interface requires three holes with a diameter of 6.6 mm equally spaced, hence 120 degrees apart, on a circle with a diameter of 62 mm. The top interface has three contact surfaces, such that points of contact are defined more accurately.
- The bottom interface requires three threaded M5 holes equally spaced, hence 120 degrees apart, on a circle with a diameter of 43 mm. The bottom interface has three contact faces as well, such that points of contact are defined more accurately.
- The length of the test object requires to be 197.5 ± 1 mm. A tolerance of ± 1 mm is allowed, because the distance between the attachment points of top and bottom interfaces in the setup can be changed slightly.
- The test object has to be able to carry a load of at least the 550 kg of the steel cylinder (MF).

With these requirements an initial design is made and optimized to come to the final design. This design is shown in Figure 3.3 for several views and dimensions. The three top and bottom contact surfaces of the test object are marked. The design optimization procedure and the specifications are worked out in Appendix B. The chosen material is aluminum resulting in a total weight of 0.33 kg.

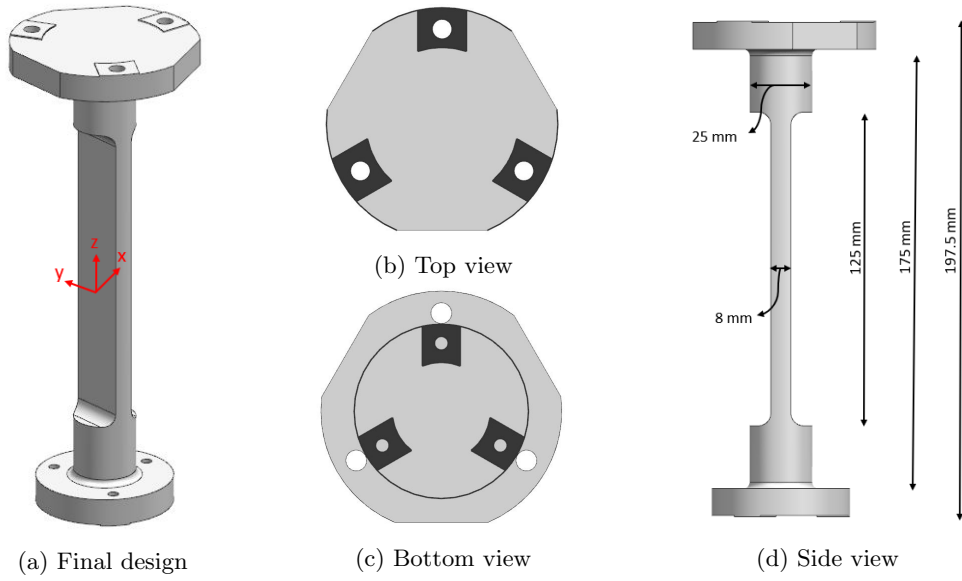


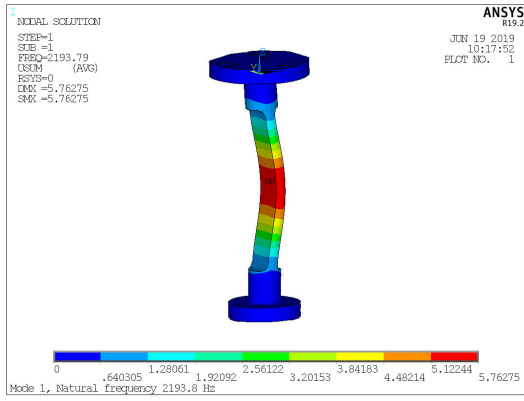
Figure 3.3: Several views and dimensions of the final test object.

3.2.1 Modal analysis

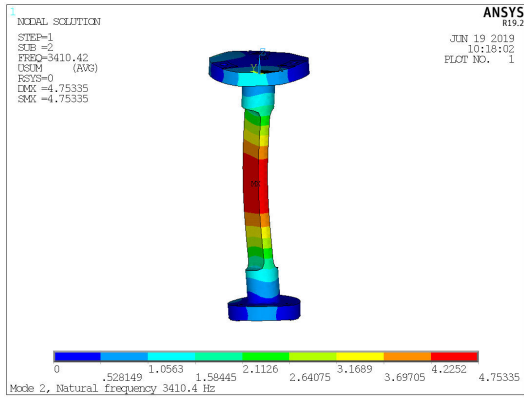
A numerical modal analysis (NMA) of the test object is performed to investigate the eigenfrequencies and corresponding eigenmodes such that it fulfills the first requirement. The constraints during this NMA prescribe that the three bottom and three top contact surfaces are fully constrained, i.e. $U_x = U_y = U_z = R_x = R_y = R_z = 0$ with U the displacements and R the rotations. The NMA is performed in ANSYS for which results of the first ten modes corresponding to the final design are given in Table 3.1 and visualized in Figure 3.4.

Table 3.1: Modal analysis of the final design with fixed boundary conditions.

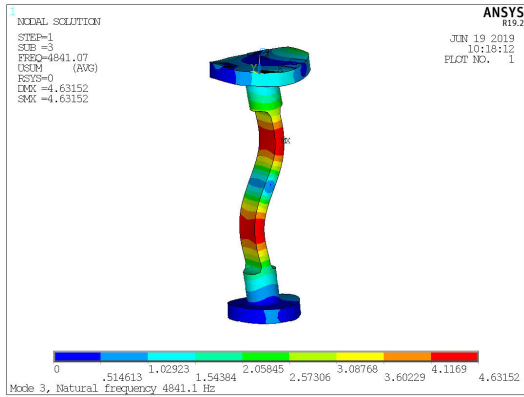
Mode	Eigenfrequency [Hz]	Description
1	2193.8	First bending in x -direction
2	3410.4	First bending in y -direction
3	4841.1	Second bending in x -direction
4	6904.7	Third bending x -direction
5	6959.0	Second bending in y -direction
6	7197.3	Torsion around z -axis
7	7811.5	Axial in z -direction
8	9259.6	Fourth bending in x -direction
9	9488.2	Third bending in y -direction
10	12130.3	Fifth bending in x -direction



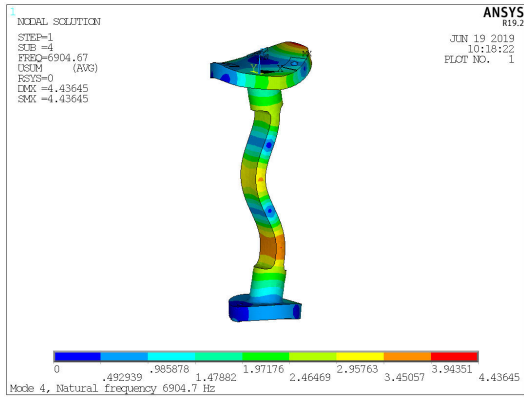
(a) Mode 1: 2193.8 Hz



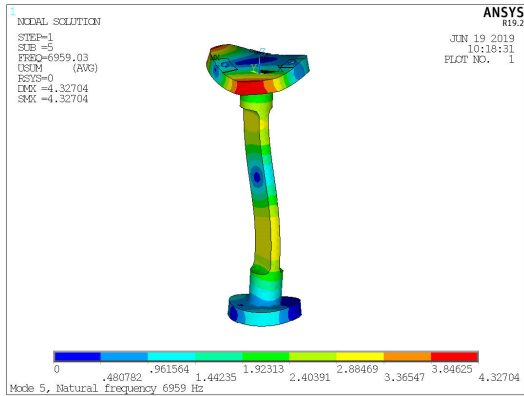
(b) Mode 2: 3410.4 Hz



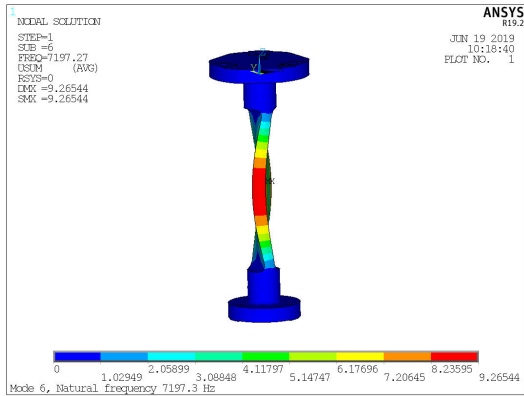
(c) Mode 3: 4841.1 Hz



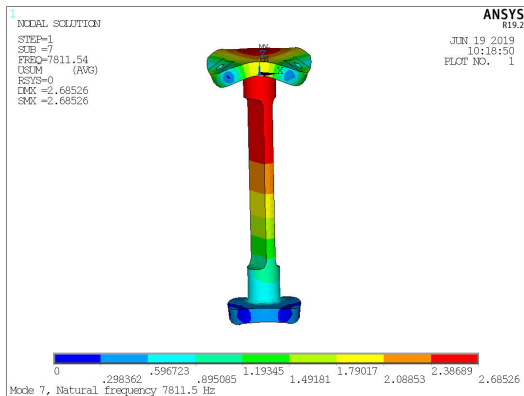
(d) Mode 4: 6904.7 Hz



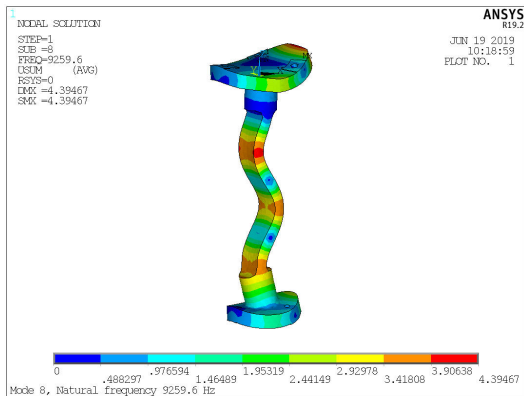
(e) Mode 5: 6959.0 Hz



(f) Mode 6: 7197.3 Hz



(g) Mode 7: 7811.5 Hz



(h) Mode 8: 9259.6 Hz

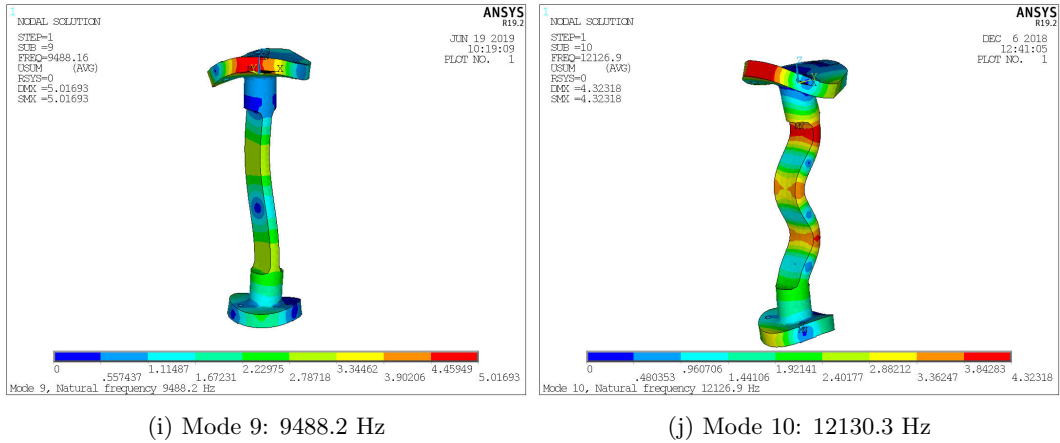


Figure 3.4: The first ten modes of the test object.

Note that the eigenfrequency of mode 1 fulfills the first requirement and results from bending in the weakest direction of the test object. During actual experiments the desired measurement direction is vertically in z -direction for which its first mode is found at 7811.5 Hz. However, measurements in z -direction might be influenced by resonance behaviour in other directions and therefore the lowest eigenfrequency in any direction is designed to be above 2000 Hz. The next step is to determine the dynamic stiffness of the test object.

3.2.2 Dynamic stiffness

The dynamic stiffness of the test object is computed for later comparison against experimental measurement results. It is numerically determined by performing modal analysis using the modal superposition method. These results are used to convert the modal data at certain points of interest (POIs) to a state space model in MATLAB. The POIs are modelled as remote points in ANSYS. In case of the test object the POIs are modelled at the top and bottom and connected to the contact surfaces.

Two methods to determine the dynamic stiffness are used and compared. The first method to derive the dynamic stiffness is to initially perform a modal analysis of the test object free in space and process the resulting modal data of the POIs. This method is referred to as the free-free method and is visualized in Figure 3.5a, where TO indicates test object. The other method to determine dynamic stiffness is to perform modal analysis with a huge point mass defined at the bottom and a stiff spring added at the top. This method is referred to as the mass-spring method and is visualized in Figure 3.5b.

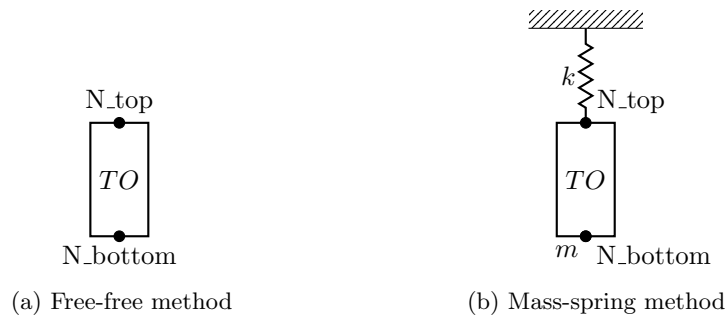


Figure 3.5: Methods to determine the dynamic stiffness.

The mass-spring method is a better representation of what actually happens during experimental dynamic stiffness measurements. The vibrations used as input to determine the dynamic stiffness are modelled at the bottom of the test object (N_{bottom}) with a huge 6 DOF point mass [kg] and mass moment of inertia [kgm^2] indicated with m to properly describe these vibrations. At the top of

the test object (N_top) a stiff 6 DOF spring k with stiffness [N/m] and rotational stiffness [Nm/rad] is modelled such that displacements can easily be converted to output forces. The values for k are chosen at least a factor 10^2 larger than the stiffness of the test object, i.e. $k \gg k_{TO}$, such that it does not influence the results. The values of m are chosen such that the eigenfrequencies due to this mass are outside the frequency range of interest during modal analysis, i.e. below 1 Hz. For the test object this results in typical values of $k = 1 \cdot 10^{10}$ N/m and $1 \cdot 10^8$ Nm/rad and $m = 1 \cdot 10^8$ kg and $1 \cdot 10^5$ kgm². When these values are lower it leads to undesired resonance behavior in the frequency range of interest due to higher eigenfrequencies of the point mass. However, when these values become larger it shows numerical instability causing incorrect results. It is therefore important to properly tune the mass and stiffness values in order to obtain accurate and numerically stable dynamic stiffness results.

3.2.2.1 Determination of dynamic stiffness

Several steps are required to determine the dynamic stiffness with the desired set of modes. First, modal analysis is performed with either the free-free method or the mass-spring method as shown in Figure 3.5. For this purpose the component mode synthesis (CMS) model reduction techniques of Hintz-Herting and Craig-Bampton as in [17][18][19][20] are often applied within ASML. These techniques are theoretically elaborated in Appendix C. Note that the CMS method is, however, not a core focus throughout this thesis and is just applied here. Next, a state space model is constructed with the (reduced) mass and stiffness matrices via modal superposition to compute the transfer from force to displacement defined as

$$H = \frac{U_{top}}{F_{bottom}}. \quad (3.5)$$

For the free-free method the dynamic stiffness can be determined by computing the inverse of (3.5). For the mass-spring method some additional steps are required to determine the dynamic stiffness. Therefore, the forces at the top and bottom are defined as

$$F_{bottom} = ma_{bottom} = ms^2 U_{bottom}, \quad (3.6)$$

$$F_{top} = kU_{top}, \quad (3.7)$$

where s is the Laplace variable. Substitution of (3.6) and (3.7) in (3.5) results in

$$H = \frac{U_{top}}{F_{bottom}} = \frac{1}{kms^2} \frac{F_{top}}{U_{bottom}}, \quad (3.8)$$

by which the dynamic stiffness is determined as the transfer from displacement to force

$$k_{dyn} = \frac{F_{top}}{U_{bottom}} = kms^2 H. \quad (3.9)$$

The resulting eigenfrequencies of the modal analysis with the mass-spring method with and without CMS reduction are given in Table 3.2.

Table 3.2: Modal analysis of final test object: mass-spring method.

Mode	Without CMS f_{eig} [Hz]	With CMS f_{eig} [Hz]	Description
1	2193.5	2193.5	First bending in x -direction
2	3408.2	3408.2	First bending in y -direction
3	4837.1	4837.1	Second bending in x -direction
4	6897.4	6897.4	Third bending in x -direction
5	6945.7	6945.7	Second bending in y -direction
6	7198.6	7198.6	Torsion around z -axis
7	7736.3	7736.3	Axial in z -direction
8	9257.1	9257.1	Fourth bending in x -direction
9	9488.1	9488.1	Third bending in y -direction
10	12121.8	12121.8	Fifth bending in x -direction

Note that the resulting eigenfrequencies are equal for the significance of 1 decimal. Also, results are almost equal compared to Table 3.1 where fixed boundary conditions are used instead of the mass-spring method. The latter results in slightly lower eigenfrequencies due to flexibility of the spring compared to the fixed boundary conditions. Figure 3.6 shows the resulting dynamic stiffness with 1% damping for both methods (free-free and mass-spring) with and without CMS. All methods result in a similar dynamic stiffness except for one off-diagonal term from U_x to F_y due to numerical instability caused by the large values for k and m .

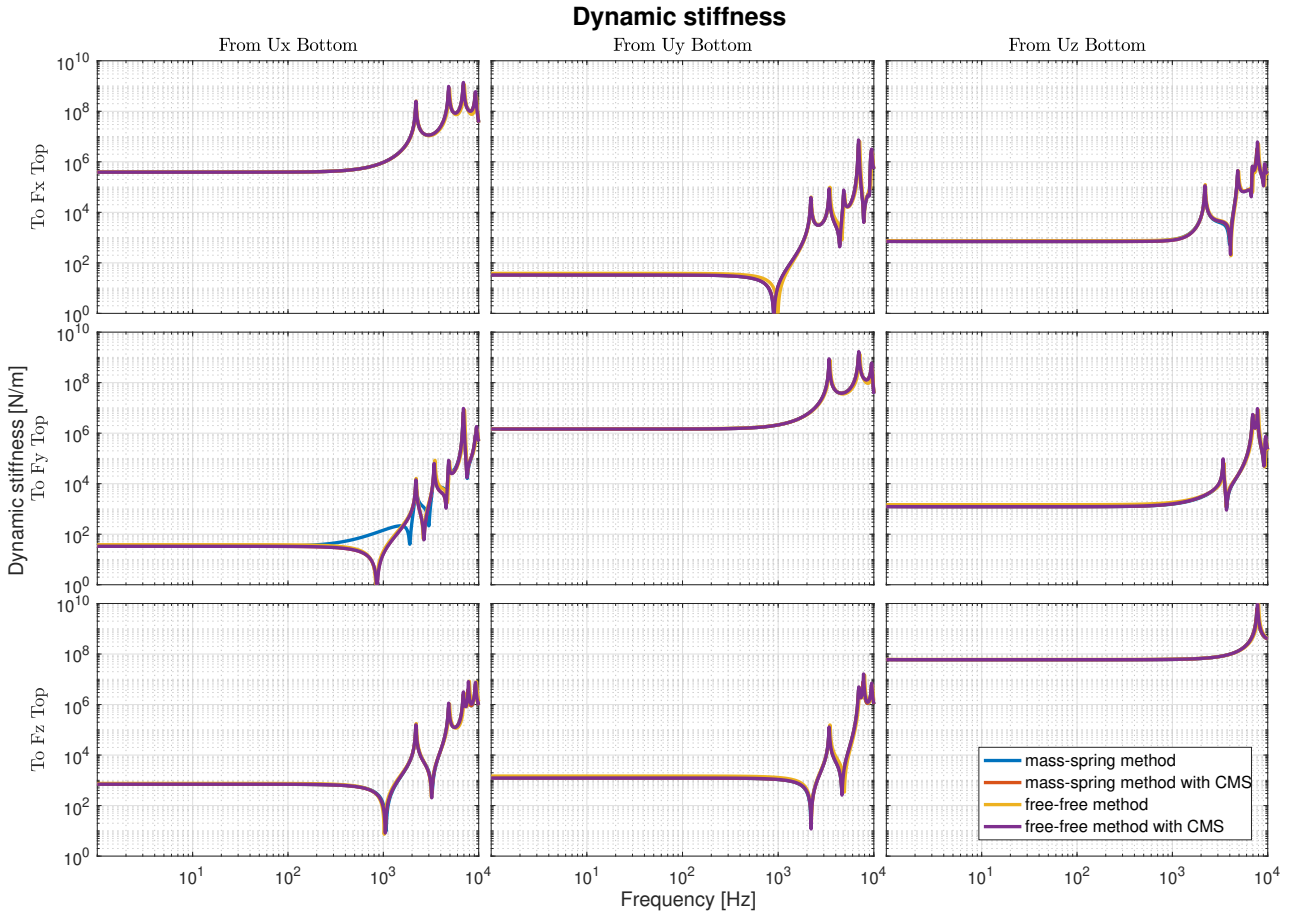


Figure 3.6: The dynamic stiffness of the final test object for all methods.

Throughout this research the main focus will be on the dynamic stiffness in vertical z -direction from U_z to F_z , since this will be the direction during experimental measurements. However, behavior in other directions (especially diagonal results) might influence measurement results and are therefore also shown. The resulting resonance frequencies match with the eigenfrequencies as in Table 3.2.

Another way to check whether the results are correct is to compute the static stiffness in ANSYS and compare it to the results in MATLAB. In ANSYS it is computed by prescribing an initial displacement on the bottom contact surfaces of the test object and then computing the resulting reaction forces with which the static stiffness can be calculated using $k_{static} = \frac{F}{U}$. In MATLAB, the static stiffness is determined from the horizontal part between 1 and 100 Hz in Figure 3.6. The results are given in Table 3.3, where xx -direction indicates the transfer from displacement in x -direction to force in x -direction, etc. The resulting values are almost similar and the static stiffness in axial z -direction indeed satisfies a value of approximately $6 \cdot 10^7$ N/m as also found in Figure 3.2.

Table 3.3: Comparison of static stiffness to check dynamic stiffness results.

Direction	ANSYS k_{static} [N/m]	MATLAB k_{static} [N/m]	Error [%]
xx	$3.869 \cdot 10^5$	$3.887 \cdot 10^5$	0.47
yy	$1.463 \cdot 10^6$	$1.466 \cdot 10^6$	0.21
zz	$5.924 \cdot 10^7$	$5.969 \cdot 10^7$	0.76

A next step is to investigate the effect of different payloads on the eigenfrequencies and stiffness of the test object. This is called a pre-stressed modal analysis.

3.2.3 Pre-stressed modal analysis

A vertical payload on top of the test object is included to perform a pre-stressed modal analysis. This payload affects the dynamic behaviour of the test object and will therefore increase the prediction accuracy of the actual behavior for realistic situations. In a pre-stressed modal analysis the test object acts as an inverted pendulum, for which the lateral stiffness can be approximated by superposition of two separate stiffness contributions as visualized in Figure 3.7 in the xz -plane. In this case the bottom of the test object is fixed and the top can only translate in x -direction.

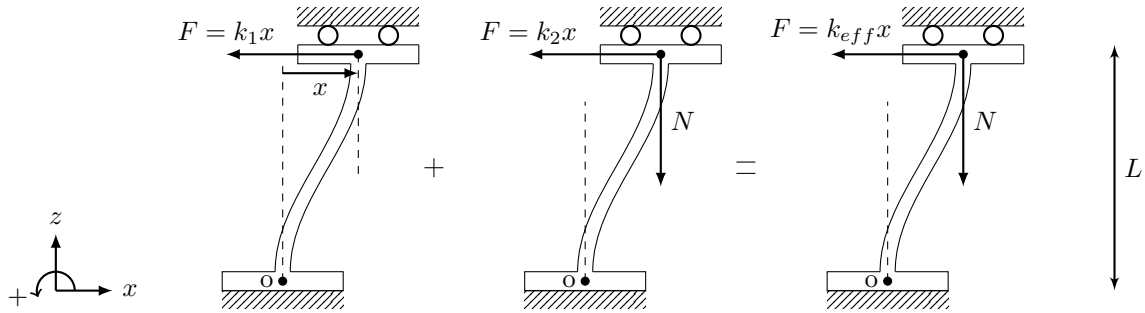


Figure 3.7: The effect of prestress on the effective stiffness.

Under the assumption that the rod has a constant diameter the positive lateral stiffness of the test object can be defined as

$$k_1 = \frac{12EI}{L^3} = \frac{12E \frac{\pi}{64} d^4}{L^3} = \frac{3\pi E d^4}{16L^3}, \quad (3.10)$$

for a constant diameter d [m] of the test object with E [Pa] the Young's modulus of the material, I [m⁴] the area moment of inertia, and L [m] the length of the test object. The other stiffness contribution results from a vertical compressive payload force on top of the test object, which tends to push the test object away from its equilibrium position. The sum of moments in this case results in

$$\begin{aligned} \sum M_o &= FL - (-Nx) = 0, \\ -\frac{N}{L} &= \frac{F}{x}, \end{aligned} \quad (3.11)$$

with N [N] the normal payload on the test object causing a negative stiffness defined as

$$k_2 = -\frac{N}{L}. \quad (3.12)$$

The combination of both contributions results in the effective lateral stiffness of the test object, which is strongly dependent on the vertical payload and results in

$$k_{eff} = k_1 + k_2 = \frac{3\pi E d^4}{16L^3} - \frac{N}{L}. \quad (3.13)$$

Note that the effective lateral stiffness of the test object will decrease for increasing payloads and as a result the eigenfrequencies will also decrease. However, the effective axial stiffness (hence the corresponding axial eigenfrequencies) will hardly be influenced by the effect of the relatively small payloads due to the relatively large axial stiffness of the test object.

This concept can also be explained with the effect of stress stiffening, which is the increase or decrease in transverse stiffness when a payload is applied in tension or compression along an axial direction. Normally, the stress stiffening effect is considered for components with relatively small lateral stiffness compared to its axial stiffness. The stress stiffening effect is accounted for by computing and using the so-called stress stiffness matrix, which is added to the regular stiffness matrix in order to give the total stiffness defined as

$$K_{tot} = K + W. \quad (3.14)$$

Here K is the regular stiffness matrix, and W is the stress stiffening matrix determined with the matrix of shape function derivatives and the matrix of the current Cauchy stresses [16]. In case of the actual situation where a compressive payload is applied along the axial direction of the test object, there is a decrease in transverse stiffness. This effect is preferably referred to as stress weakening, resulting in a decrease of total stiffness and corresponding eigenfrequencies as concluded before. Figure 3.8 shows the dynamic stiffness results of pre-stressed modal analyses for several payloads with 1% damping.

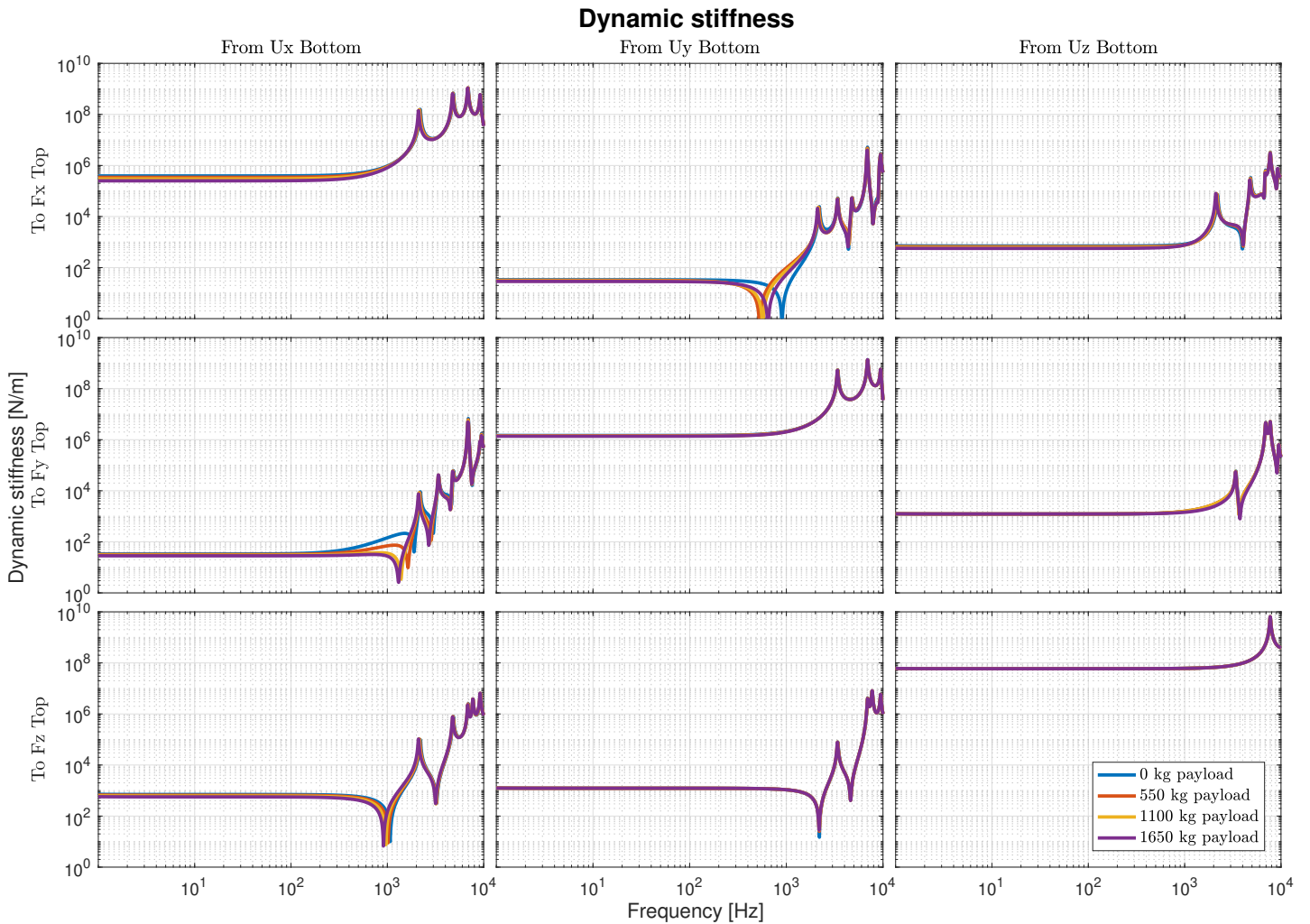


Figure 3.8: The pre-stressed dynamic stiffness of the final test object.

It can be seen that the payloads influence the static stiffness and eigenfrequencies of the test object especially in the xx -direction and some cross directions. This is due to the negative stiffness contribution which is also referred to as stress weakening. However, for the directions with higher stiffness it is difficult to notice the influence. The resulting static stiffness values for the different payloads are therefore given in Table 3.4.

Table 3.4: The static stiffness as result of different payloads on the test object.

Payload	0 kg	550 kg	1100 kg	1650 kg
Direction	k_{static} [N/m]	k_{static} [N/m]	k_{static} [N/m]	k_{static} [N/m]
xx	$3.89 \cdot 10^5$	$3.43 \cdot 10^5$	$2.97 \cdot 10^5$	$2.50 \cdot 10^5$
yy	$1.47 \cdot 10^6$	$1.43 \cdot 10^6$	$1.40 \cdot 10^6$	$1.37 \cdot 10^6$
zz	$5.94 \cdot 10^7$	$5.94 \cdot 10^7$	$5.94 \cdot 10^7$	$5.94 \cdot 10^7$

As expected the static stiffness decreases linearly in the lateral x - and y -direction for increasing payloads, whereas the static stiffness in z -direction does not change due to the relatively small payloads. Also the eigenfrequencies are influenced by different payloads for which results are given in Table 3.5. As expected the eigenfrequencies decrease for increasing payloads.

Table 3.5: The eigenfrequencies as result of different payloads on the test object.

Payload	0 kg	550 kg	1100 kg	1650 kg	Description
Mode	f_{eig} [Hz]	f_{eig} [Hz]	f_{eig} [Hz]	f_{eig} [Hz]	
1	2193.5	2164.8	2135.5	2105.6	First bending in x -direction
2	3408.2	3398.8	3389.3	3379.9	First bending in y -direction
3	4837.1	4807.8	4778.0	4747.9	Second bending in x -direction
4	6897.4	6873.5	6849.3	6825.0	Third bending in x -direction
5	6945.7	6938.3	6930.9	6923.5	Second bending in y -direction
6	7198.6	7193.0	7187.4	7181.8	Torsion around z -axis
7	7736.3	7732.6	7728.8	7725.0	Axial in z -direction
8	9257.1	9231.3	9205.3	9179.2	Fourth bending in x -direction
9	9488.1	9481.2	9474.2	9467.2	Third bending in y -direction
10	12121.8	12095.5	12069.2	12042.9	Fifth bending in x -direction

These results are pure dynamic behavior of the test object. An experimental modal analysis is performed on the test object to validate the numerical model.

3.3 Experimental modal analysis of the test object

An experimental modal analysis is performed on the test object using modal hammer excitations. In this analysis the test object is put on a soft foam to mimic free-free conditions. Figure 3.9 shows this setup in which also the global coordinate system and the roving hammer excitation grid are indicated. Note that excitation point 2 is located in the middle of the top interface and excitation point 7 is the driving point which is hit by initially rotating the object. Five hits are use at each excitation point for averaging. The three DOF PCB356A01 accelerometer is attached in the middle of the object on a flat face and connected to the PAK data acquisition system as well as the DYTRAN 5800B4 modal hammer. Further details on how to perform this measurement are elaborated in Appendix D.

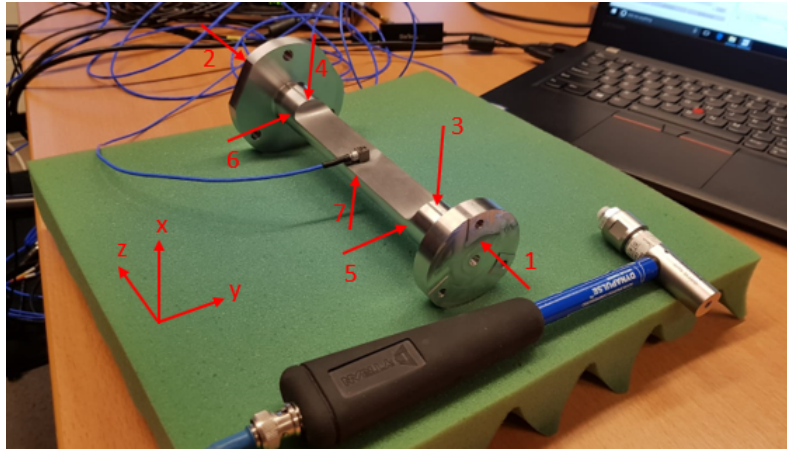


Figure 3.9: Free-free EMA on the test object.

The EMA results are compared to the NMA results of a free-free modal analysis in ANSYS. Figures 3.10, 3.11 and 3.12 show the transfer from force to acceleration in similar directions, once for each direction (x , y , z), and the corresponding coherence for excitation points 1, 5 and 7, respectively. In the numerical results 1% damping is used.

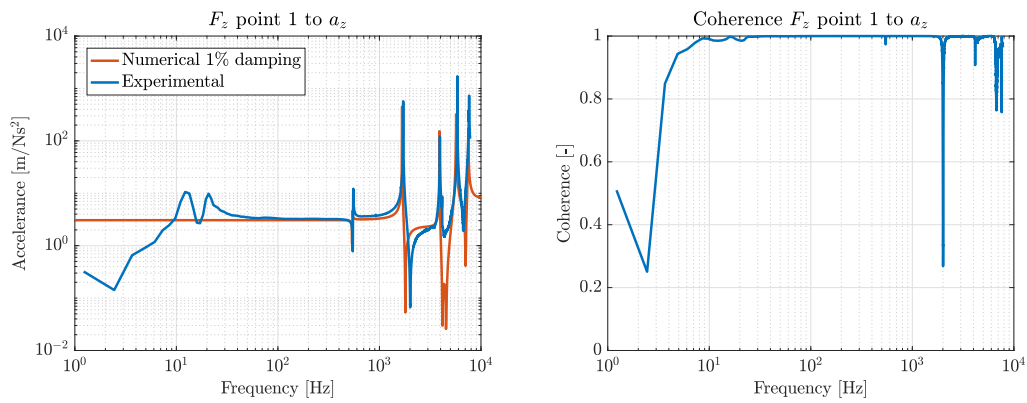


Figure 3.10: EMA vs. NMA acceleration point 1 (left) and EMA coherence (right).

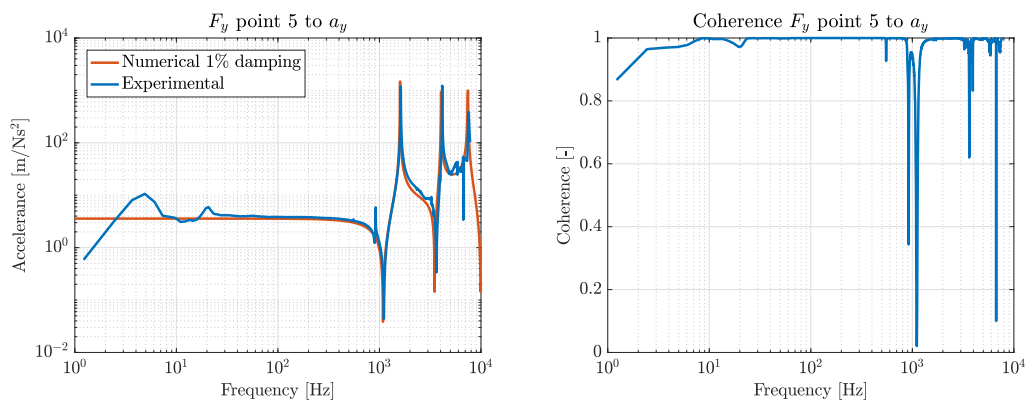


Figure 3.11: EMA vs. NMA acceleration point 5 (left) and EMA coherence (right).

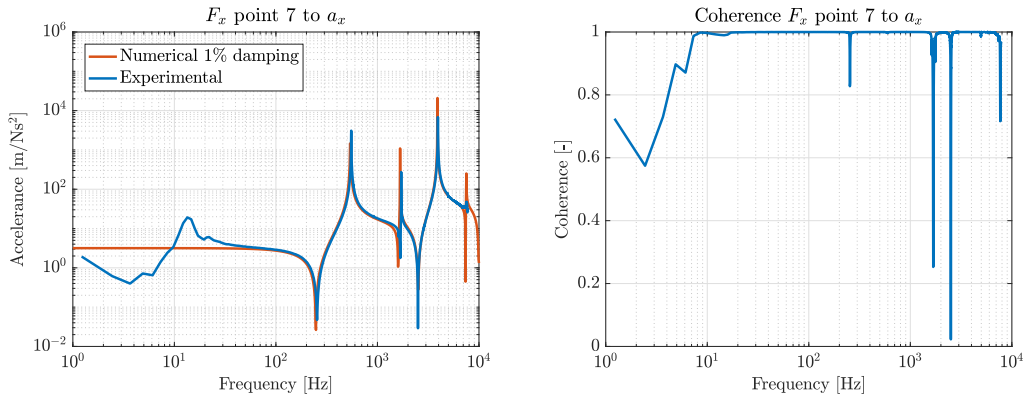


Figure 3.12: EMA vs. NMA acceleration point 7 (left) and EMA coherence (right).

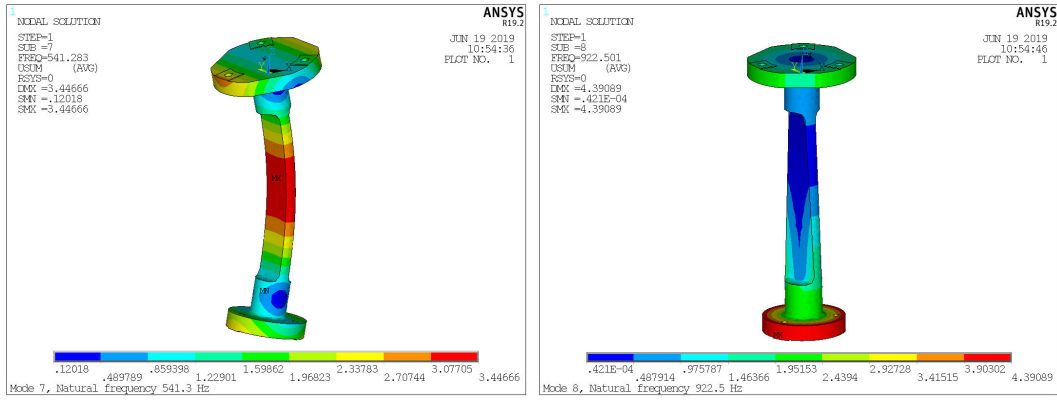
It is shown that numerical and experimental results match quite well apart from some striking differences. These differences can for example be caused by different material and damping properties, the fact that experimental excitation is not perfectly aligned and consistent, and the fact that experimental modal analysis is not entirely free-free. The latter causes the low frequency resonance peaks in the experimental results. These are caused by the rigid body modes of the test object on the stiffness of the soft foam and are also called suspension modes. The coherence plots indicate a proper measurement quality except near anti-resonances. However, it is normal that the coherence is poor near anti-resonances where the vibration response is low.

The numerical and experimental eigenfrequencies are compared next. The resulting values are given in Table 3.6 and visualized in Figure 3.13 where the rigid body modes are left out as well as the low frequency suspension modes. Note that the numerical and experimental results slightly differ within a error margin of 3%. These differences can again be caused by for example different material and damping properties, and the fact that experimental modal analysis is not entirely free-free.

Table 3.6: Free-free NMA vs. EMA on the test object.

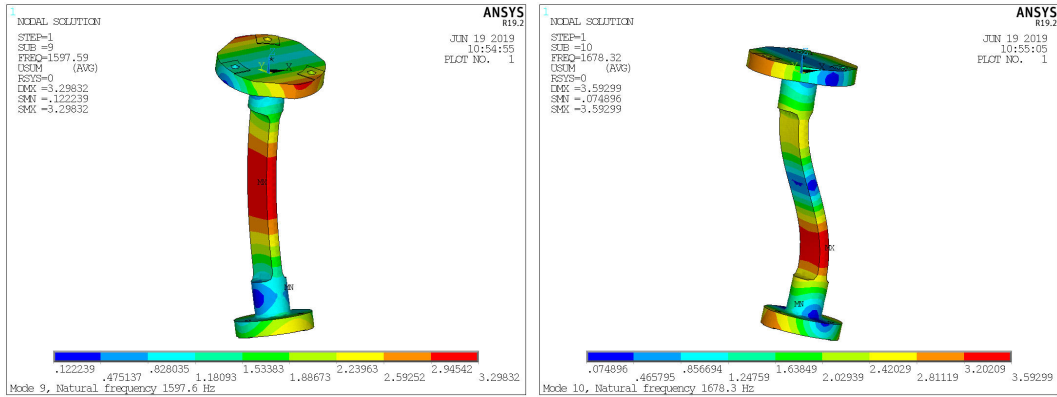
Mode	f_{NMA} [Hz]	f_{EMA} [Hz]	Error [%]	Description
1	541.3	551.8	1.9	First bending in x -direction
2	922.5	919.2	0.4	First torsion around z -axis
3	1597.6	1622.3	1.5	First bending in y -direction
4	1678.3	1713.9	2.1	Second bending in x -direction
5	3919.3	3941.7	0.6	Third bending in x -direction
6	4054.3	4148.2	2.3	Second bending in y -direction
7	5713.5	5859.3	2.6	Axial in z -direction
8	7358.2	7405.1	0.6	Second torsion around z -axis
9	7442.3	7515.9	1.0	Third bending in y -direction
10	7530.9	7641.7	1.5	Fourth bending in x -direction

3.3. EXPERIMENTAL MODAL ANALYSIS OF THE TEST OBJECT



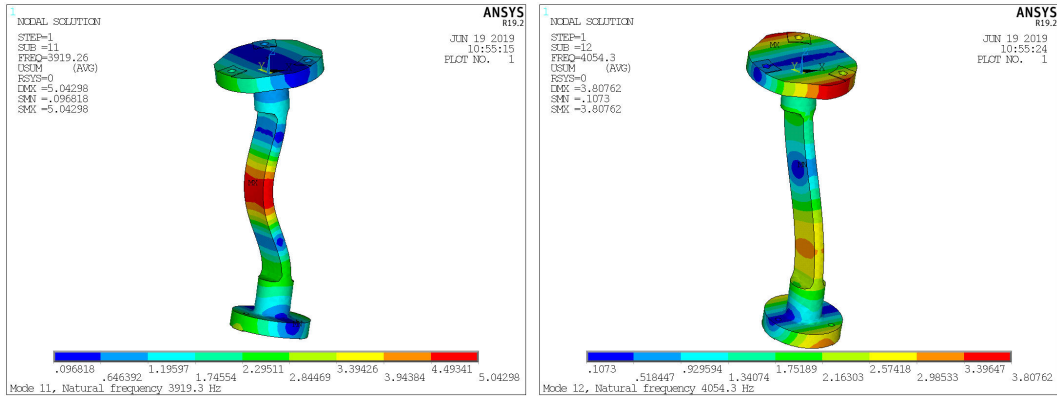
(a) Mode 1: 541.3 Hz

(b) Mode 2: 922.5 Hz



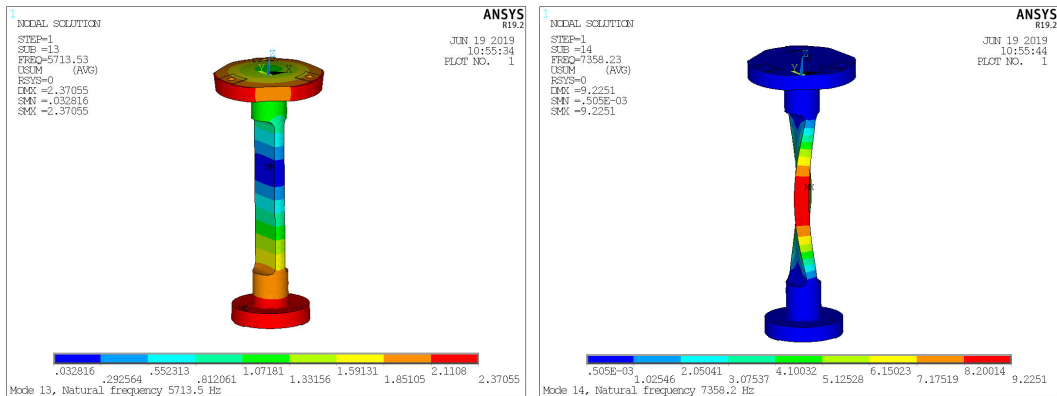
(c) Mode 3: 1597.6 Hz

(d) Mode 4: 1678.3 Hz



(e) Mode 5: 3919.3 Hz

(f) Mode 6: 4054.3 Hz



(g) Mode 7: 5713.5 Hz

(h) Mode 8: 7358.2 Hz

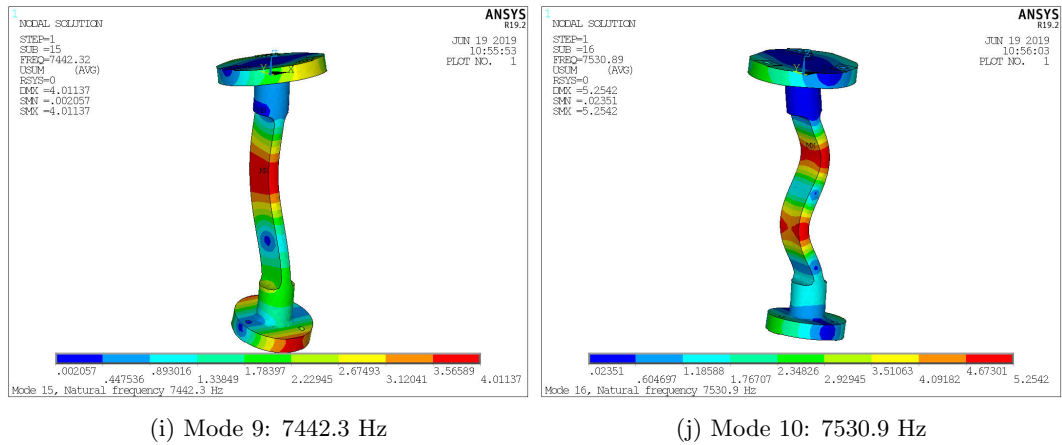


Figure 3.13: Modes visualization of the test object.

It can be concluded that the numerical model of the test object is validated with the aid of experimental results. The next step is to develop a 3-dimensional finite element model of the dynamic stiffness measurement setup in which the test object can be mounted.

3.4 Finite element model

A 3-dimensional geometry model of the dynamic stiffness setup is made in Siemens NX. It is used to eventually perform numerical modal analysis with the finite element method in ANSYS. Therefore, a detailed NX model of the setup is initially adapted to the configuration for the test object. This implies for example placing the test object plus its interface such that it fits in between the shaker table and the force cell as shown in Figure 3.14a. Furthermore, the bellow is moved to the top of the frame instead of underneath such that it can pull the metrology frame upwards to the desired height and pre-load. The desired configuration is now modelled such that it can be simplified for FEM calculations to reduce computational costs while maintaining accuracy during NMA. The model is simplified by: removing most holes to make meshing easier and quicker, removing the legs of the granite stone, and uniting connected components of the setup with similar material properties. Figure 3.14b shows the simplified model including component names and the global coordinate system.

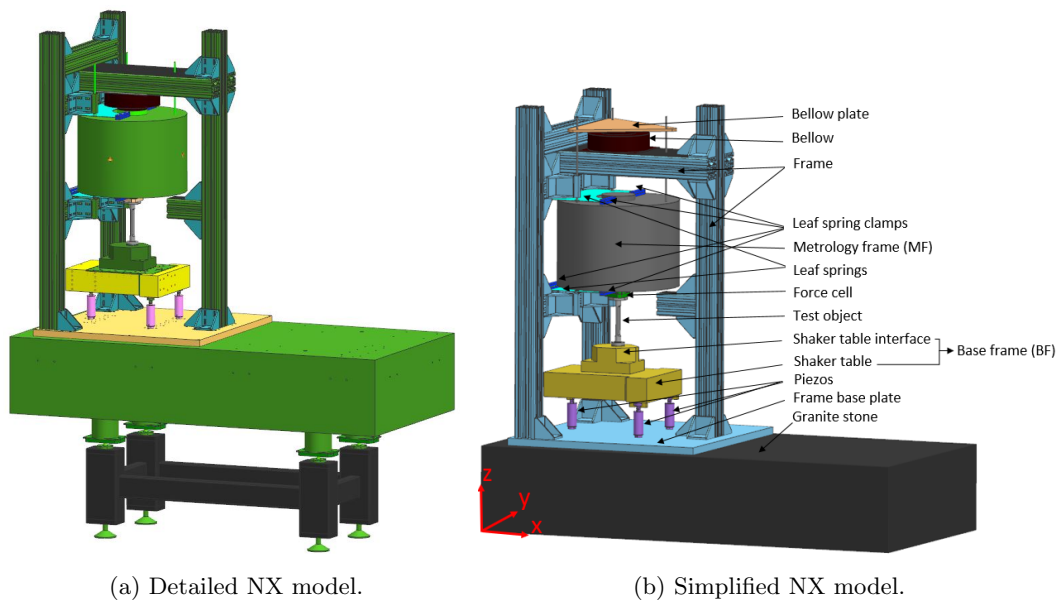


Figure 3.14: Detailed setup model vs. simplified setup model for FEM.

Note that in Figure 3.14b different colors are used to indicate united components such as the shaker table plus the interface (yellow), and the frame with the frame base plate (light blue), but also to indicate similar material properties of components which can not be united such as the piezo actuators (purple), the leaf springs (teal) and the leaf spring clamps (dark blue). This simplified model is used to perform NMA for which several assumptions are initially made. These assumptions imply that contacts between components are bonded and the bottom of the granite stone is fixed. A mesh is generated using quadratic tetrahedral elements (frame, piezos, shaker table, test object, force cell, MF and bellow) and quadratic hexahedral elements (granite stone, leaf spring clamps, M8 rods and bellow plate). The leaf springs are very thin and therefore shell elements are used. The resulting number of elements, nodes and DOFs after a mesh convergence study are listed in Table 3.7.

Table 3.7: The mesh properties of the dynamic stiffness setup FE model.

Component	#elements	#nodes	#DOFs
Granite stone	4.536	21.345	128.070
Frame	318.246	575.840	3.455.040
Piezoes (3x)	111.770	171.431	1.028.586
Shaker table + interface	11.720	19.565	117.390
Test object	9.258	15.065	90.390
Force cell	24.208	37.369	224.214
Metrology frame	15.444	27.224	163.344
M8 rods	756	5.844	35.064
Leaf spring (2x)	8.975	9.779	58.674
Leaf spring clamps (12x)	1.086	8.300	49.800
Bellow	4.892	8.378	50.268
Bellow plate	485	3.629	21.774
Total	511.376	903.769	5.422.614

A fine mesh is used for geometrically complex parts such as the test object, piezos, frame, force cell, and leaf springs and a coarse mesh is used for geometrically simple parts such as the granite stone and the MF. Moreover, a local mesh refinement is applied to the saw cuts of the leaf springs and the piezo tips. Further decreasing the mesh size barely changes the modal data (maximum 5% in the frequency range of interest) whereas it greatly increases the computational time. For some cases it even causes insufficient disk space to solve the calculations locally, e.g. halving the element size of the mesh. Therefore the mesh properties as in Table 3.7 are used to perform the FEM calculations. However, due to the large amount of DOFs these calculations are still computationally expensive. In a future study it is thus recommended to apply a model reduction technique as for example introduced in [25] or with component mode synthesis as in [17][19][20][26] and shortly elaborated in Appendix C.

Experimental modal analysis is required to obtain the true dynamic behavior of the setup such that the FE model can be updated. The results of the updated FE model compared to the experimental results as well as further experimental measurements and validations are elaborated in Chapter 4.

3.5 Summary

In this chapter several numerical models are introduced which are used to predict the dynamic behavior of the setup and the test object. Initially, a 1-dimensional lumped mass-spring model of the setup is designed to examine influence of the dynamic behavior of the setup on the dynamic stiffness of the object under test. Afterwards, a test object has been designed which is used to eventually validate the dynamic stiffness measurement setup. A thorough investigation is executed on performing numerical modal analysis to determine the dynamic stiffness. This investigation is based on the test object to keep it simple and get familiar with the way of working. Also, the numerical model of the test object is validated with the aid of experimental modal analysis. Lastly, a 3-dimensional finite element model is designed in order to eventually obtain more representative predictions of true dynamic behavior. This model will be updated using experimental data as elaborated in Chapter 4.

Chapter 4

Experimental measurements and validation

In order to obtain accurate and reliable numerical models they can be improved and updated if necessary with the aid of experimental results. These experimental results are obtained by performing experimental measurements and experimental modal analysis. The outcome can be considered as (closest to) the true dynamic behavior and is used to perform experimental validation. A measurement plan to formulate what and how to measure before executing experimental measurements is elaborated in Appendix D. This plan includes step-by-step guides for both piezo and modal hammer measurements and the measurement equipment used.

In this chapter the results of dynamic stiffness measurements with the test object mounted in the setup are investigated first. The influence of the dynamic behavior of the setup on these measurement results is examined. This behavior is subsequently investigated by performing experimental modal analysis on the setup using a modal hammer. These results are post-processed in order to obtain the dynamic properties. After post-processing and investigating the experimental results, the finite element model is updated such that the dynamic properties can be approximated and dynamic stiffness measurements can be imitated. At the end of this chapter a discussion is given on the results.

4.1 Dynamic stiffness measurements

A measure to characterize the vibration isolation performance of vibration isolation systems is the dynamic stiffness. It is therefore highly relevant to experimentally measure this property of a certain vibration isolation system and validate the results prior to practical usage. An experimental dynamic stiffness measurement setup is available within ASML as elaborated in Section 1.2.2. However, the measured dynamic stiffness does not purely consist of only the dynamic stiffness of the vibration isolation system to be investigated. The accuracy of the measured dynamic stiffness in a certain frequency range depends on the accuracy of the sensors and alignment of setup modules for example, and is influenced by exciting the dynamic behavior of the setup itself as well. Referring to the research goals, there is a wish to validate the test setup in order to fully understand the experimental results obtained during dynamic stiffness measurements in a frequency range of 1 - 2000 Hz. As shown in Figure 4.1 the test object is mounted in the setup such that validation experiments can be performed.

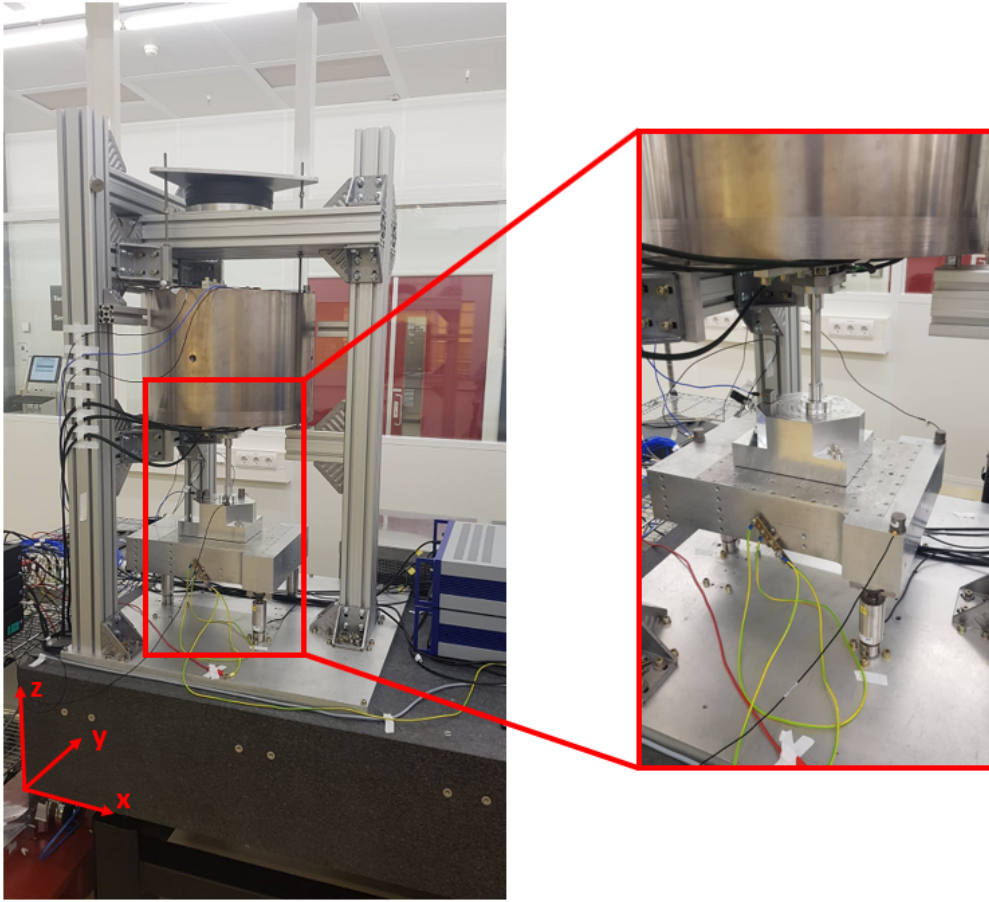


Figure 4.1: The test object mounted in the setup.

It can be seen that the test object is attached on top of the shaker table interface and to the bottom of the force cell interface. During vertical dynamic stiffness measurements a white noise signal is sent to the three piezo actuators which excite the shaker table. The resulting forces are measured at the force cell with three 3 DOF Kistler 9027C force sensors. These can be combined to calculate a global force in 6 DOF. In this research only the global force in vertical z -direction is used. The resulting accelerations are measured at the steel cylinder (metrology frame) and the shaker table configuration (base frame) with each three 1 DOF B&K 4381 accelerometers. These are combined to a global acceleration in z -direction and used to determine rotations R_x and R_y . One 3 DOF PCB356B18 accelerometer is used for the accelerations in x - and y -direction. Note that rotations R_z are not measured. The specifications of these sensors are given in Table 4.1.

Table 4.1: The specifications of the sensors used during dynamic stiffness measurements.

Force sensor	Kistler 9027C	Accelerometer	B&K4381	PCB356B18
Type	Charge	Type	Charge	ICP
Direction	3D	Direction	1D z -direction	3D
Range	$F_x, F_y \pm 4 \text{ kN}$ $F_z \pm 8 \text{ kN}$	Range	$\pm 2000 \cdot 9.81 \text{ m/s}^2$	$\pm 50 \cdot 9.81 \text{ m/s}^2$
Sensitivity	$F_x, F_y \approx -7.8 \text{ pC/N}$ $F_z \approx -3.8 \text{ pC/N}$	Sensitivity	10 pC/ms^2	100 mV/ms^2
Overload	$F_x, F_y \pm 5 \text{ kN}$ $F_z \pm 10 \text{ kN}$	Bandwidth	0.1 - 4800 Hz	0.5 - 3000 Hz
Mass	30 grams	Mass	43 grams	25 grams

Note that during this research the focus is on the vertical z -direction. By integrating the measured accelerations twice (in the frequency domain) the dynamic stiffness can be determined as the transfer from the relative displacement between the MF and BF to the global force at the FC and is thus defined as

$$k_{dynamic}(f) = \frac{F_{FC}(f)}{U_{MF}(f) - U_{BF}(f)}. \quad (4.1)$$

The experimental properties during dynamic stiffness measurements are listed in Table 4.2. The measured time signals are divided into blocks of 100.000 samples with 50% overlap such that the noisy signals can be averaged. A Hanning window is applied to each data block to avoid signal leakage after which the FFT of each block and therewith the averaged power spectral densities are computed. Averaging is necessary because the PSD corresponding to the random (white noise) excitation signal is a random process itself and it reduces the influence of measurement noise.

Table 4.2: The experimental measurement properties.

Full measurement property	Symbol	Value	Unit
Measurement time	T	120	s
Sample frequency	f_s	50.000	Hz
Number of samples	N	6.000.000	-
Frequency resolution	Δf	0.0083	Hz
Sample time	ΔT	0.00002	s
Data block property	Symbol	Value	Unit
Measurement time	T_B	2	s
Number of samples	N_B	100.000	-
Frequency resolution	Δf_B	0.5	Hz
Overlapping	-	50	%
Number of blocks/averages	N_a	119	-

With these properties the experimental data is obtained and post-processed. During the dynamic stiffness measurements there are several features which (might) influence the results such as sensor locations, sensor fixation, and measurement noise. These features are investigated such that reliable data is obtained and, perhaps more importantly, the results are understood. The investigation on sensor locations is elaborated first whereas examples of inappropriate sensor fixation and standstill measurement noise are examined in Appendix E. Moreover, measurement repeatability is investigated to check the agreement of successive measurements. Lastly, the influence of the dynamic behavior of the setup is shown and should be investigated with experimental modal analysis.

4.1.1 Sensor locations

The locations of sensors greatly influence the measurement results hence a proper choice of sensor locations is relevant in order to obtain reliable and convenient results. The force sensors have a fixed location during dynamic stiffness measurements and the MF accelerometer locations are restricted by the leaf springs. Therefore the locations of the BF accelerometers, which can be placed anywhere on either the shaker table or the shaker table interface, are varied when the test object is mounted in the setup. For other objects to be measured, such as an airmount, the possible sensor locations may be more restricted. The investigated BF z -direction accelerometer locations are visualized in Figure 4.2 where the top view of the BF (shaker table plus its interface) is shown. Each sensor location group is colored and named.

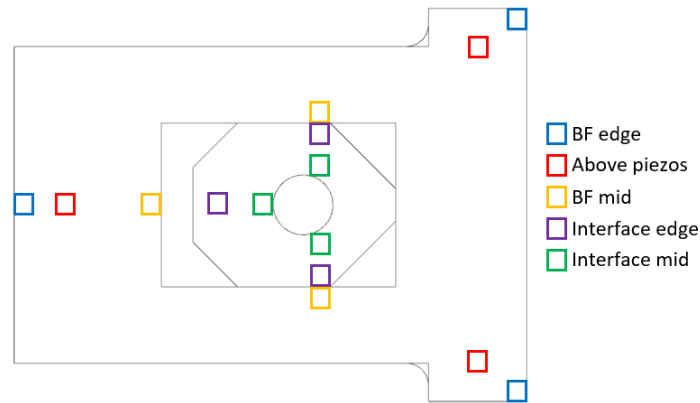


Figure 4.2: Top view of the shaker table with the different accelerometer locations.

Five different sensor location groups with each a different name and color are used to investigate dynamic stiffness measurement results. Three sensor groups are positioned on the shaker table (BF edge, above piezos and BF mid) and two sensor groups are positioned on the shaker table interface (interface edge and interface close). Note that the colors of each sensor group match the colors in the dynamic stiffness results as shown in Figure 4.3.

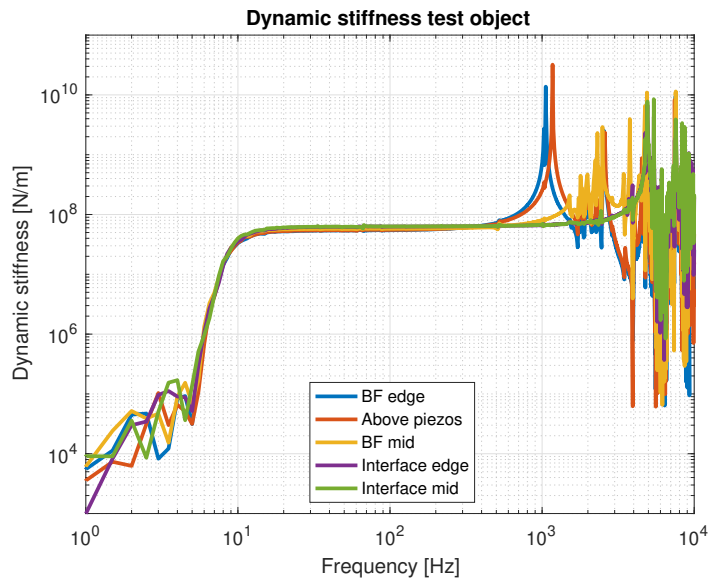


Figure 4.3: The dynamic stiffness results for several BF accelerometer locations.

The resulting dynamic stiffness of each measurement is almost similar until approximately 500 Hz, after which internal dynamic behavior of the shaker table starts to play a huge role in the measurement results. One can see that the sensor groups located on the shaker table (BF edge, above piezos and BF mid) show resonance peaks in the dynamic stiffness results from 1 to 3.5 kHz, whereas the sensor groups on the shaker table interface (interface edge and interface mid) do not or are just slightly affected. The dominant resonance peaks at 1057 Hz of the blue line (BF edge) and 1157 Hz of the red line (above piezos) as well as the other resonances in the 1.5 - 3.5 kHz region are mainly caused by anti-resonances in the acceleration responses of the corresponding sensor location groups due to internal dynamic behavior of the shaker table. Moreover, the shaker table interface shows dynamic behavior relative to the shaker table itself. This behavior is not or to a lesser extent observed at the shaker table, hence a less convenient reconstruction of the BF accelerations is obtained here to determine the dynamic stiffness. Therefore it is recommended to place the accelerometers on the shaker table interface instead of on the shaker table itself if the configuration of the setup allows this.

Furthermore, the motions of the MF and BF are almost identical for low frequencies. This is due to the relatively high axial stiffness of the test object such that the MF follows the motion of the BF. At 5 Hz the MF and BF move exactly in phase causing an anti-resonance in the measured force. Afterwards, the measured force starts to increase since the motion of the MF and BF starts to diverge and move out of phase. The divergence is caused by the vertical mode of the MF on the combined stiffness of the test object, leaf springs, threaded rods, and bellow after which the MF motion decouples. Thereby the dynamic stiffness increases until the static axial stiffness of the test object is reached at around 10-20 Hz. Hence the low frequency measurement results are unreliable below 10-20 Hz due to the relatively high stiffness of the test object. For objects with a lower stiffness, which is typical for vibration isolation systems, the low frequency results will fortunately improve.

Moreover, until 5 Hz the measurements are greatly influenced by noise which is examined by performing standstill measurements as elaborated in Appendix E. The influence of noise results in poor measurement quality as shown in Figure 4.4 where the coherence is plotted.

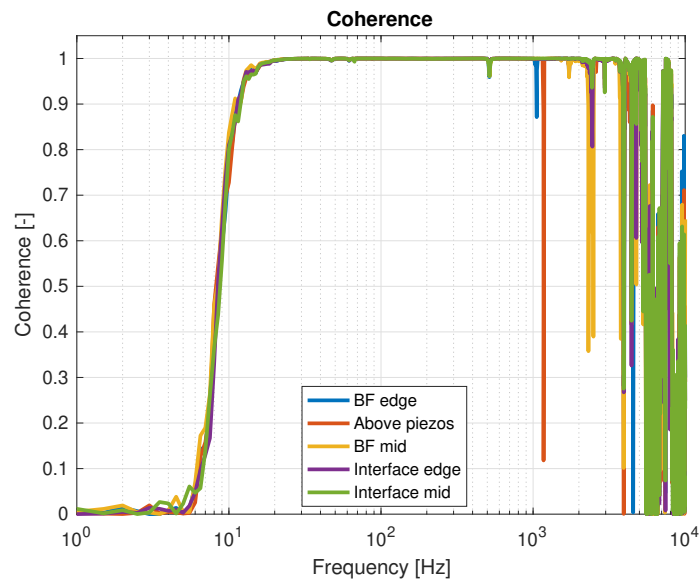


Figure 4.4: The coherence for several BF accelerometer locations.

The measurement quality is poor until 5 Hz after which the coherence and with that the measurement quality increases. Note that beyond 5 kHz the measurement quality becomes poor as well due to the accuracy limitations of the sensors and the decoupling of the force cell after its vertical mode at approximately 5 kHz. Also near or at (anti-)resonances the coherence drops which frequently occurs for the case when the accelerometers are placed on the shaker table rather than its interface. Therefore, further dynamic stiffness measurements are performed with the BF accelerometers located at the purple sensor group (interface edge) on the BF interface. These locations are preferred over the green sensor group (interface mid) since more free space is created for objects to be mounted on the BF interface. In Figure 4.5 the results are compared to the predicted dynamic stiffness obtained in Chapter 3 of purely the test object and the mass-spring model with both 1% damping.

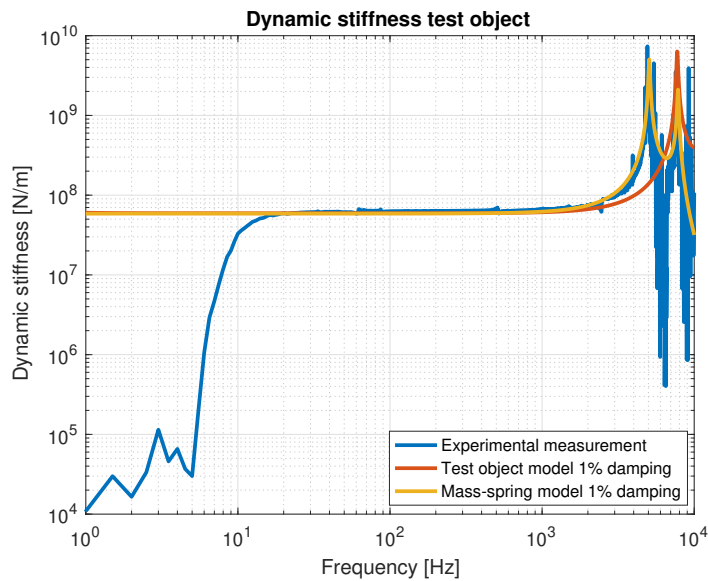


Figure 4.5: Comparison of experimental versus numerical dynamic stiffness results.

It can be seen that the numerical results globally predict the experimental measurement reasonably well. The static stiffness lines approximately coincide as well as the resonance peak at 5 kHz and the vertical mode of the test object at around 7.6 kHz. These simple numerical models indicate that reliable results are obtained. A next step is to perform a repeatability test.

4.1.2 Repeatability test

Experimental measurements can be disturbed or influenced by several causes (for example floor vibrations) and it is therefore highly relevant that reliable and repetitive results are obtained. In order to check the repeatability of the dynamic stiffness measurements ten consecutive reference measurements under the same conditions are performed and compared. Figure 4.6 shows the measured dynamic stiffness results of these ten measurements, which can hardly be distinguished from each other.

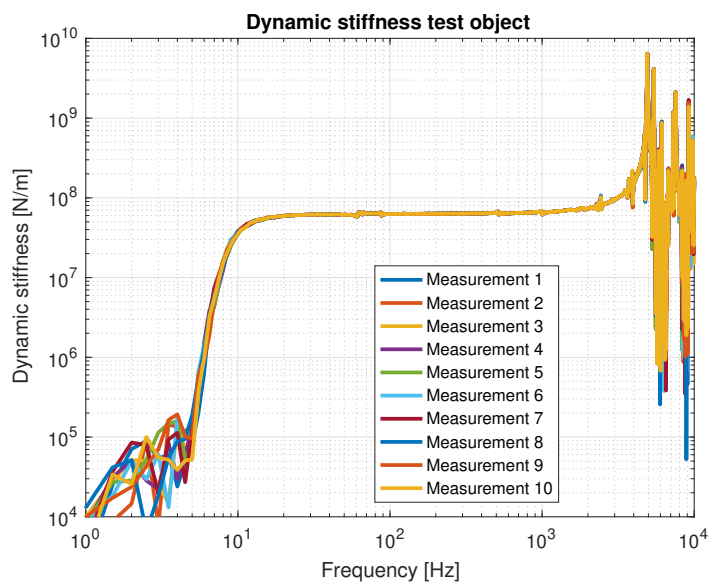


Figure 4.6: The dynamic stiffness results of ten consecutive measurements.

It can be seen that the FRFs of the consecutive dynamic stiffness measurements globally match apart for the poor measurement quality region of 1 - 5 Hz. Figures 4.7a and 4.7b show close ups of the results in the frequency ranges of 10 - 2000 Hz and 2 kHz - 10 kHz, respectively.

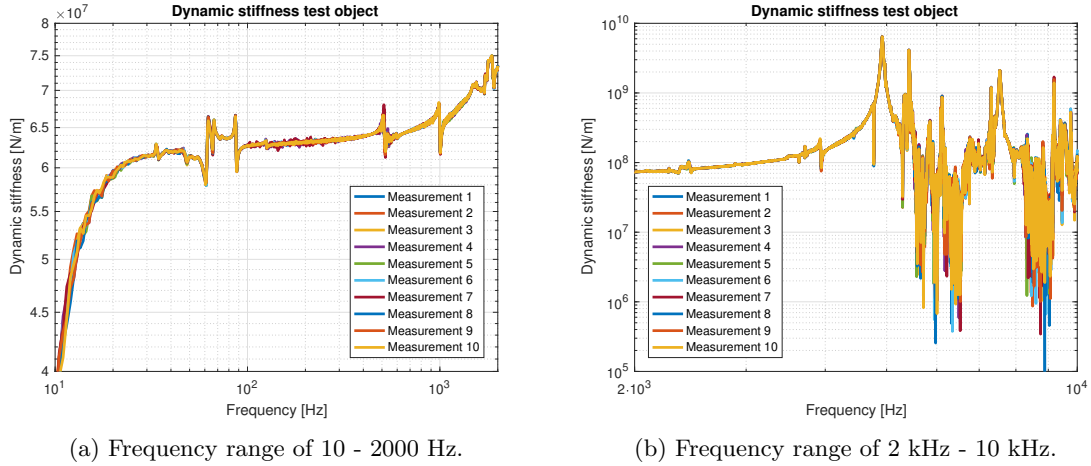


Figure 4.7: Close ups of the ten consecutive dynamic stiffness results.

The measurement results are still hard to distinguish from each other. It can thus be concluded that these measurements are repeatable under the same conditions. The repeatability can also be valued by computing the frequency response assurance criterion (FRAC), which indicates the correlation of FRFs.

4.1.2.1 Frequency response assurance criterion

Comparison of FRFs representing the same input-output relationship is done with the frequency response assurance criterion [9]. The FRAC indicates the correlation between FRFs and varies between 0 and 1, where 1 indicates perfect correlation and 0 no correlation at all. Once the FRFs are measured the FRAC can be computed and is defined as

$$FRAC = \frac{\left| \sum_{f_{\min}}^{f_{\max}} H_i(f) H_j^*(f) \right|^2}{\sum_{f_{\min}}^{f_{\max}} H_i(f) H_i^*(f) \sum_{f_{\min}}^{f_{\max}} H_j(f) H_j^*(f)}, \quad (4.2)$$

with H the measured FRFs and H^* the complex conjugate of the FRFs in the frequency range of $f_{\min} \leq f \leq f_{\max}$ for $i = 1, 2, \dots, N$ and $j = 1, 2, \dots, N$ with N the number of measurements. Note that the frequency resolution of all the FRFs should match. The FRAC values for the ten consecutive measurements are given in Table 4.3.

Table 4.3: The FRAC values of the ten consecutive measurements.

FRAC	1	2	3	4	5	6	7	8	9	10
1	1	0.92	0.92	0.92	0.91	0.91	0.91	0.91	0.92	0.91
2	0.92	1	0.92	0.92	0.91	0.92	0.91	0.92	0.92	0.91
3	0.92	0.92	1	0.92	0.92	0.92	0.92	0.92	0.92	0.92
4	0.92	0.92	0.92	1	0.92	0.92	0.92	0.92	0.92	0.92
5	0.91	0.92	0.92	0.92	1	0.92	0.92	0.92	0.92	0.92
6	0.91	0.92	0.92	0.92	0.92	1	0.92	0.92	0.92	0.92
7	0.91	0.91	0.92	0.92	0.92	0.92	1	0.92	0.92	0.92
8	0.91	0.92	0.92	0.92	0.92	0.92	0.92	1	0.92	0.92
9	0.91	0.92	0.92	0.92	0.92	0.92	0.92	0.92	1	0.92
10	0.91	0.91	0.92	0.92	0.92	0.92	0.92	0.92	0.92	1

Note that the diagonal terms are all equal to one, since these results represent comparison of the FRFs with themselves. The off-diagonal correlations also result in high FRAC values which proves the (consecutive) measurements to be repeatable.

Next, five dynamic stiffness measurements which are performed a few days apart from each other are compared. This implies that the bellow has been deflated and inflated with an air compressor for tyres with an analogue pressure gauge which is inaccurate. Also the sensors are moved and reattached in between these measurements. Figure 4.8 shows the resulting dynamic stiffness measurements.

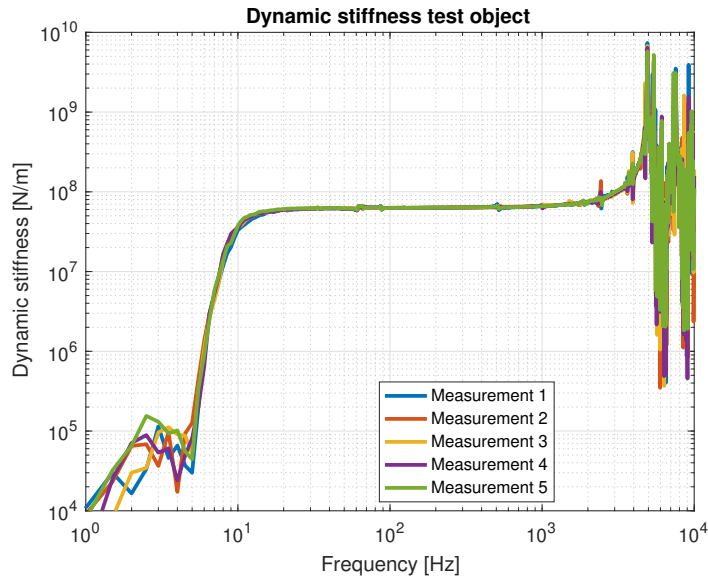
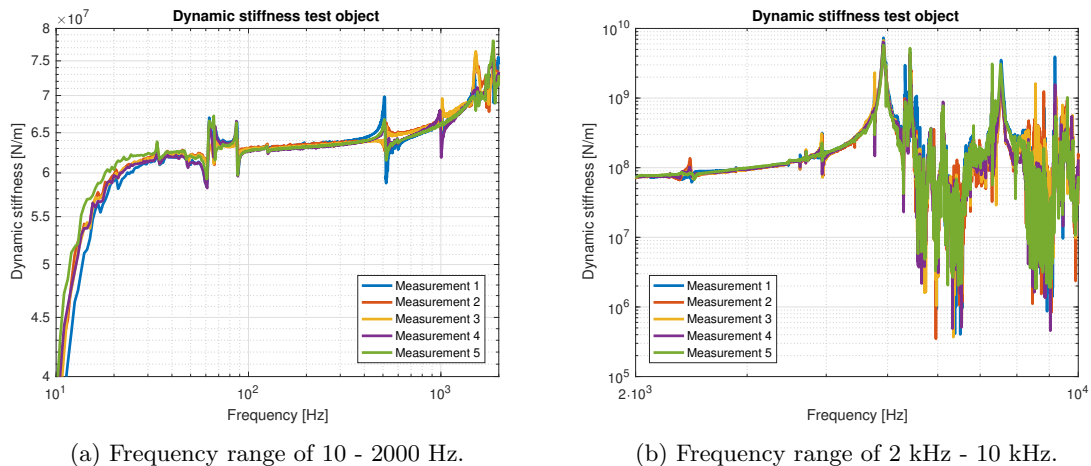


Figure 4.8: The dynamic stiffness results of five non-consecutive measurements.

These results seem to be similar apart from the low frequency region again as well as for frequencies above 2 kHz. Figures 4.9a and 4.9b show close ups of the results in the frequency ranges of 10 - 2000 Hz and 2 kHz - 10 kHz, respectively.



(a) Frequency range of 10 - 2000 Hz.

(b) Frequency range of 2 kHz - 10 kHz.

Figure 4.9: Close ups of the five non-consecutive dynamic stiffness results.

In this case it can be seen that the measurement results differ from each other in terms of shifted eigenfrequencies and the dominance of resonance peaks. Table 4.4 gives the FRAC values indicating that these FRFs are indeed less correlated than the ten consecutive measurements.

Table 4.4: The FRAC values of the five non consecutive measurements.

FRAC	1	2	3	4	5
1	1	0.77	0.74	0.73	0.56
2	0.77	1	0.84	0.79	0.66
3	0.73	0.84	1	0.82	0.55
4	0.73	0.79	0.82	1	0.56
5	0.56	0.66	0.55	0.56	1

The lower FRAC values compared to the previous values as in Table 4.3 prove the importance of consistently inflating the bellow as well as placing the sensors exactly at the same locations. Note that thus far the dynamic stiffness results are only globally investigated where dynamic behavior of the setup is hard to distinguish apart from the 5 kHz mode probably originating from the force cell. In order to examine the influence of dynamic behavior of the setup in the frequency range of interest and the striking high frequency modes, close ups of the dynamic stiffness results are inspected next.

4.1.3 Influence of dynamic behavior

Referring to the research problems it is known that the dynamic behavior of the setup influences measurement results. Therefore close ups of the dynamic stiffness results in the frequency ranges of 10 - 2000 Hz and 2 kHz - 10 kHz are shown in Figures 4.10a and 4.10b, respectively, such that resonance behavior is clearly visible.

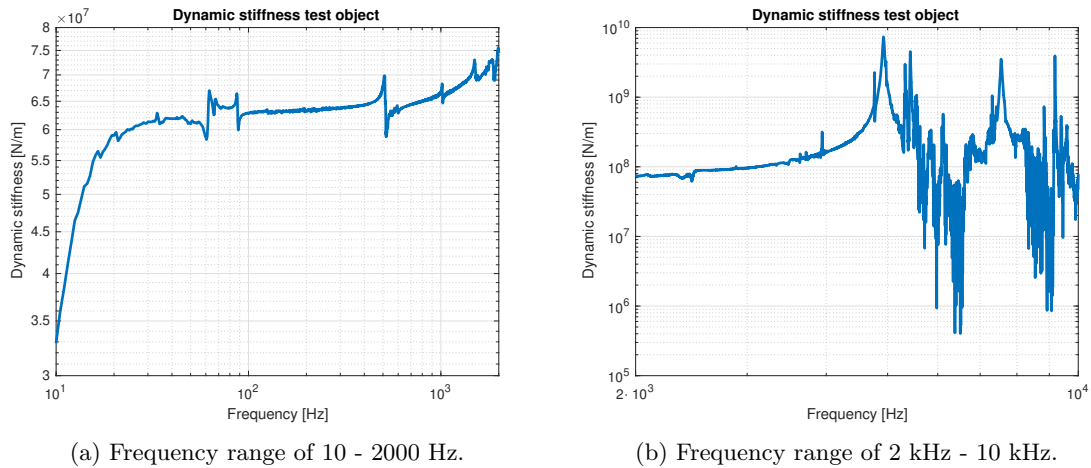


Figure 4.10: Close ups of the dynamic stiffness results.

There are a number of resonances (probably) caused by dynamic behavior of the setup which are now clearly visualized and are yet to be identified. In the lower frequency range of 10 - 2000 Hz the amplitude is relatively small compared to the higher frequency range of 2 kHz - 10 kHz. It is interesting to see that some high frequency resonances are easy to distinguish from the noisy high frequency signal such as the resonances at 5 kHz and 7.6 kHz. The first presumably originates from the vertical mode of the force cell (interface) after which it decouples and the measurement quality becomes poor and the latter is mainly caused by the vertical mode of the test object. Note that the dynamic stiffness in the frequency range of 10 - 2000 Hz gets lifted due to the dominant 5 kHz resonance. This mode influences the measurements in the frequency range of interest which might be problematic and should be improved on or compensated for. Moreover, it would be satisfactory to be able to link each resonance peak to either a mode shape or an operational deflection shape (ODS) of the setup. For this purpose experimental modal analyses on the setup are performed.

4.2 Experimental modal analysis of the setup

An experimental modal analysis on the dynamic stiffness setup is performed in order to examine the dynamic behavior excited during dynamic stiffness measurements. The results of this analysis are required to: clarify the experimental results during dynamic stiffness measurements, update the numerical models, and eventually propose improvements to be made.

Initially, an EMA is performed by hitting a 45 degrees block attached to the frame. A DYTRAN 5800B4 hammer with a nylon tip and extra mass is used to cause an impulsive force due to the impact for which the acceleration responses are measured with accelerometers. Usage of the 45 degrees block results in a good repeatability, excitation in all directions at the same time, and multiple position measurements at the same time using the roving sensor approach which is therefore less time consuming. This approach implies that the point of impact remains the same while the sensor positions change and is used because the sensors are more flexible with respect to positioning. The results of this first EMA are investigated and have given global knowledge about the dynamic behavior of the setup especially for the frame which is excited. Less energy is, however, inserted to the shaker table configuration (BF) and the heavy steel cylinder (MF) resulting in a poor signal to noise ratio. This also causes the deflections of the frame to be relatively large compared to the more interesting ODSs of the BF and MF.

A second EMA is therefore performed by hitting a 45 degrees block attached to the shaker table. Responses are measured at the BF, test object, force cell, and MF using a finer sensor grid. This is required to obtain more detailed knowledge about the (internal) dynamic behavior of these components which influence dynamic stiffness measurements. For this analysis a PCB086C03 modal hammer with a nylon tip is used since the nylon tip of the DYTRAN 5800B4 was no longer available. Figure 4.11 shows close ups of the points of impact for the first EMA (left) and the second EMA (right).

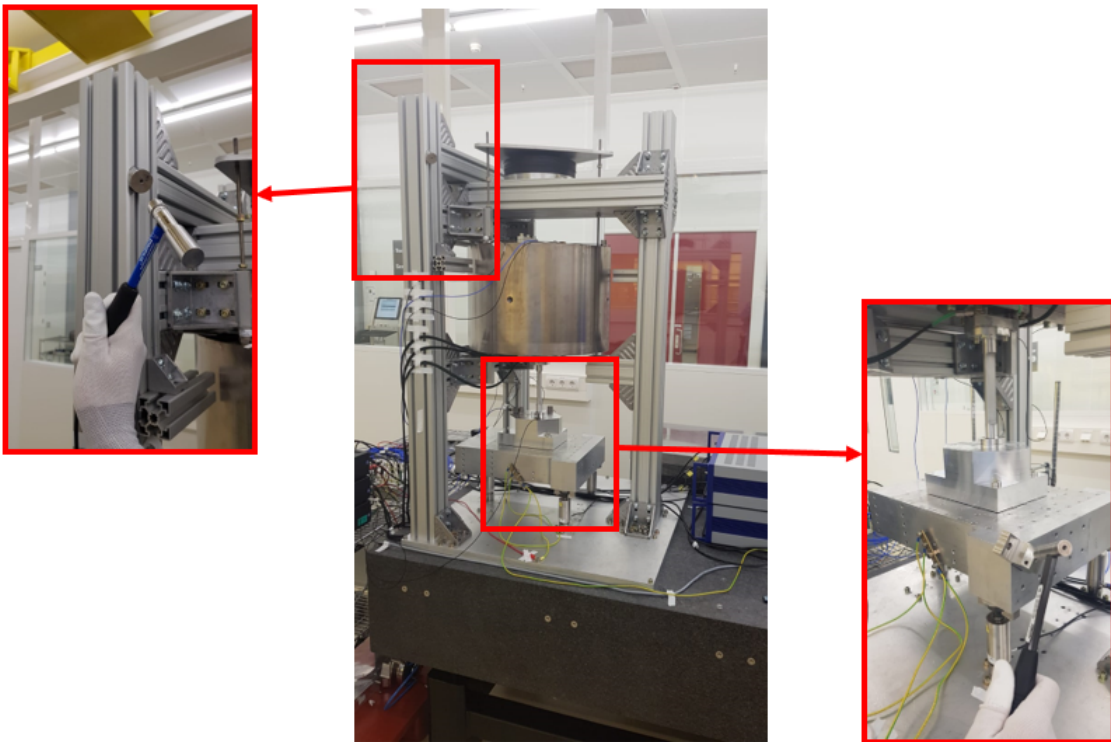


Figure 4.11: The points of impact during EMA.

The excitation due to the impact is measured by the force transducer in the head of the hammer and the resulting responses are measured with two types of accelerometers (PCB356A15 and PCB356B18) with different sensitivities. The specifications of the modal hammers and the accelerometers used during EMA on the setup are listed in Table 4.5.

Table 4.5: The specifications of the hammers and accelerometers used during EMA on the setup.

Hammer	DYTRAN 5800B4	PCB086C03	Accelero	PCB356A15	PCB356B18
Type	ICP	ICP	Type	ICP	ICP
Range	2 kN	2.2 kN	Range	$\pm 50\cdot 9.81 \text{ m/s}^2$	$\pm 50\cdot 9.81 \text{ m/s}^2$
Sensitivity	2 mV/N	2.25 mV/N	Sensitivity	10 mV/ms ²	100 mV/ms ²
Mass	220 grams	160 grams	Mass	10 grams	25 grams
			Direction	3D	3D
			Bandwidth	2-5000 Hz	0.5 - 3000 Hz

Note the difference in sensitivity of the accelerometers. The PCB356A15 accelerometers have a lower sensitivity and are used to measure responses of the excited components since enough energy is induced here and to prevent overloads. The PCB356B18 accelerometers have a higher sensitivity and are required to measure enough response elsewhere than the excited component since less energy is induced at these components. During these modal tests the hammer and five accelerometers are connected simultaneously to a PAK data acquisition system, which is connected to a laptop with PAK software. Each sensor group measurement with five accelerometers is averaged over (at least) five impacts to obtain smooth and reliable FRFs. The force impulse is windowed with a rectangular window to eliminate noise after the impact and the response is windowed with a decaying exponential window to minimize leakage. The measurement properties are listed in Table 4.6 for both analyses.

Table 4.6: The measurement properties during EMA 1 (frame) and EMA 2 (shaker table).

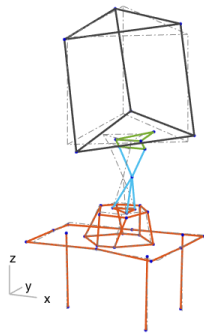
Property	Symbol	EMA 1	EMA 2	Unit
Measurement time	T	0.4	1.6	s
Sample frequency	f_s	10240	20000	Hz
Number of samples	N	4096	32000	-
Frequency resolution	Δf	2.5	0.625	Hz
Sample time	ΔT	$9.8\cdot 10^{-5}$	$5.0\cdot 10^{-5}$	s
Number of impacts/averages	N_a	5	5	-

The second EMA employs a higher sample frequency to examine the high frequency modes and a finer frequency resolution to obtain more detailed results. The measured data is post-processed such that the dynamic behavior of the setup influencing dynamic stiffness results can be visualized and examined. Figures 4.10a and 4.10b show the corresponding resonance peaks to be investigated due to ODSs of the setup. These ODSs mostly indicate modes and are listed in Table 4.7.

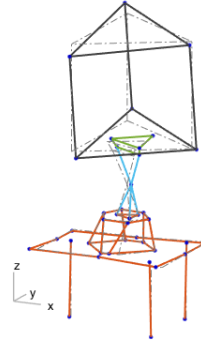
Table 4.7: The interesting ODSs during dynamic stiffness measurements.

ODS	Frequency [Hz]	ODS explanation
1	15.6	MF rotation R_y
2	21.3	MF rotation R_x
3	33.5	Frame bending $U_x \rightarrow$ MF and shaker table (mainly) translation U_z
4	62.5	Shaker table rotation R_z on piezo
5	67.5	Shaker table rotation R_z on piezo
6	87.0	Shaker table translation U_x on piezo
7	123.0	Shaker table rotation R_z on piezo
8	508.0	Shaker table rotation R_x on piezo
9	593.0	Shaker table rotation R_y on piezo
10	1031.0	Shaker table interface rotation R_x
11	1486.0	Shaker table internal bending U_z
12	1919.0	Shaker table interface torsion R_z
13	4959.0	Force cell interface U_z mode
14	7547.0	Test object (and force cell) mainly translation U_z

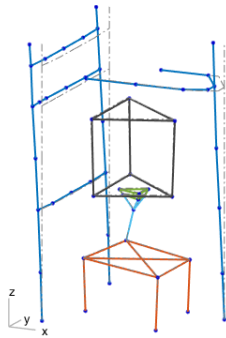
Note that only ODS 3 is experimentally obtained with EMA 1 in which the frame is excited whereas all the other ODSs are obtained with EMA 2 in which the shaker table is excited. These ODSs are also visualized in Figure 4.12 and most of the ODSs originate from the rigid body motions of the shaker table on top of the piezo actuators and internal modes of the shaker table. Only the resonance peaks in the dynamic stiffness results are investigated here, but EMA results also show many other ODSs indicating modes. These modes, however, do not affect the dynamic stiffness results in z -direction.



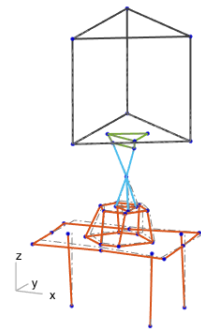
ODS 1: 15.6 Hz



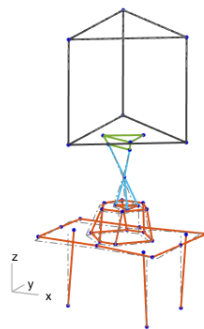
ODS 2: 21.3 Hz



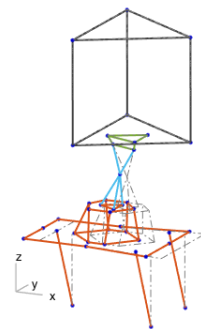
ODS 3: 33.5 Hz



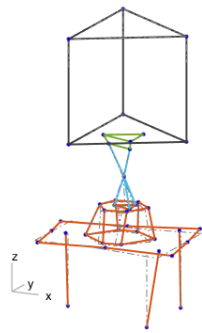
ODS 4: 62.5 Hz



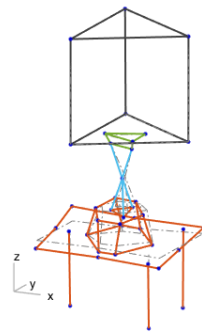
ODS 5: 67.5 Hz



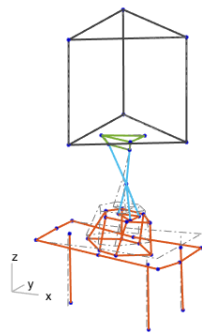
ODS 6: 87.0 Hz



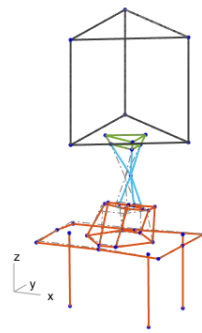
ODS 7: 123.0 Hz



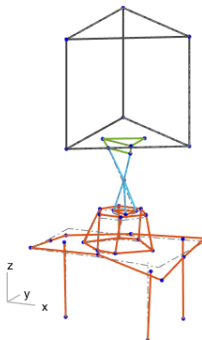
ODS 8: 508.0 Hz



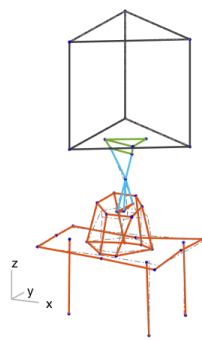
ODS 9: 593.0 Hz



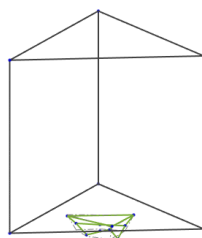
ODS 10: 1031.0 Hz



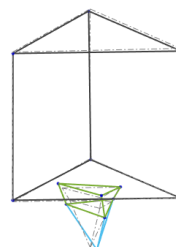
ODS 11: 1486.0 Hz



ODS 12: 1919.0 Hz



ODS 14: 4959.0 Hz



ODS 15: 7547.0 Hz

Figure 4.12: ODS visualization.

These experimental results clarify the dynamic behavior of the setup influencing the dynamic stiffness measurements. With this experimental data the numerical FE model as introduced in Section 3.4 is updated such that it can be employed to perform reliable numerical simulations. This includes performing numerical modal analysis of the setup and numerical dynamic stiffness measurements with any vibration isolation system mounted in the setup. The updated FE model can also be used to approximate and investigate possible improvements of the setup before practical implementation. Before that it has to be verified that the FE model is reliable by comparing experimental and numerical results.

4.3 Experimental versus numerical results

Prior to comparison of the experimental and numerical results the FE model is updated such that it is valid and representative results are obtained. Remember that in this FE model several assumptions are made. Bolted connections between components are ignored and replaced by bonded contact, and the bottom of the granite stone is fixed since its legs are ignored. It is also greatly simplified by removing (threaded) holes to simplify meshing, uniting parts of the frame and force cell, and assuming that the piezo actuators and the bellow are massive volumes. After simplification of the model it is mainly updated by tuning the material properties of the piezo actuators and the bellow. After this tuning procedure the numerical dynamic behavior matches the experimental dynamic (true) behaviour within a 10% accuracy margin for most modes.

In this section the results of experimental and (updated) numerical modal analysis are compared first. This is required to verify that predictions of the dynamic behavior with the FE model are reliable to represent the true experimental behavior. At the end of this section the dynamic stiffness measurements are imitated with the updated FE model and compared to experimental measurement results.

4.3.1 Modal analysis

Results of the experimental and numerical modal analysis are compared in order to verify that the FE model is properly tuned. For this purpose the dominant experimental ODSs are found first with the complex mode indicator function using the imaginary part of the FRF matrix as elaborated in Section 2.2.5 and in [14][15]. Each peak in the CMIF plot indicates a mode and the dominant peaks influencing the dynamic stiffness measurements are encircled as shown in Figure 4.13, where also the contribution of each direction is shown.

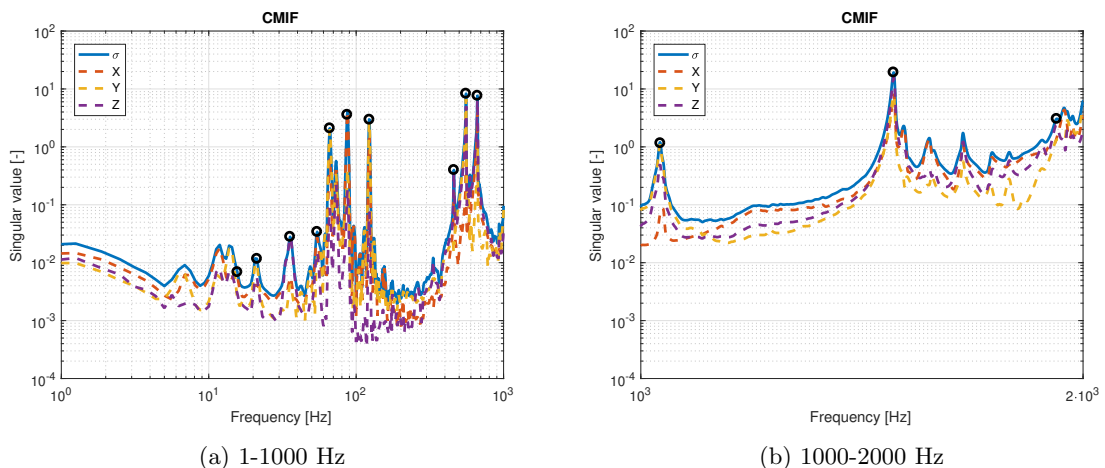


Figure 4.13: Close ups of the CMIF plot.

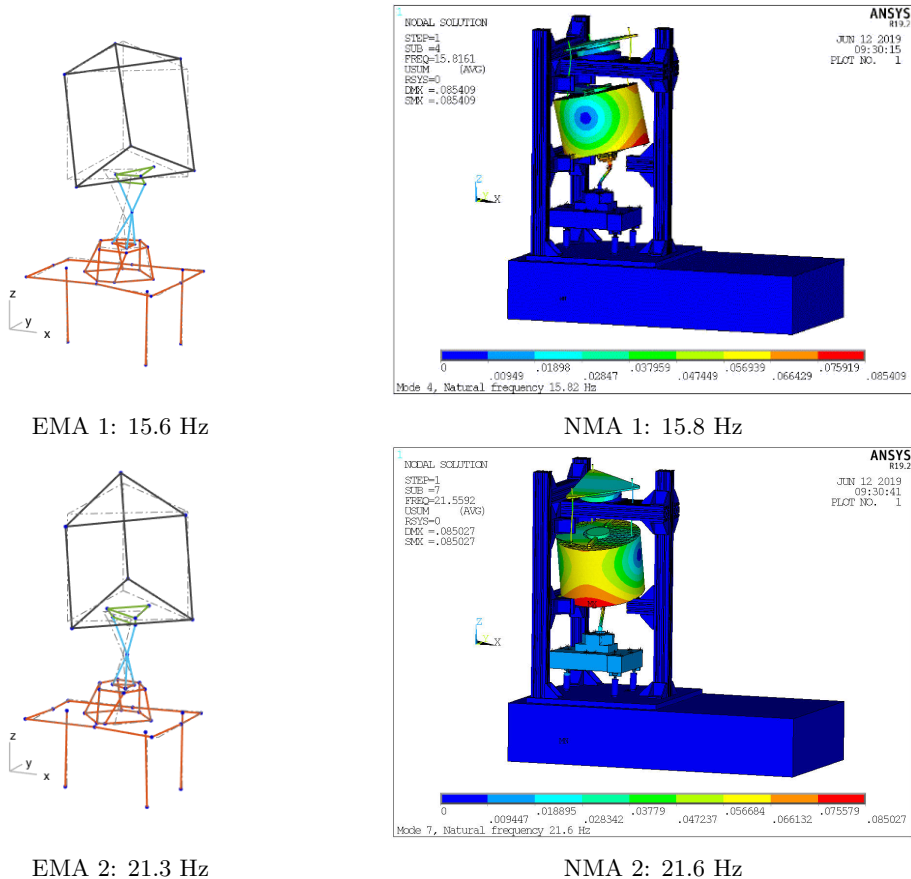
Note that the low frequency peaks in Figure 4.13a originate from the modes of the MF. These are (mostly) compensated for in the definition of dynamic stiffness as in (4.1) where the relative displacement between the MF and BF is used. Therefore, the resonance peaks below 15 Hz are ignored. The

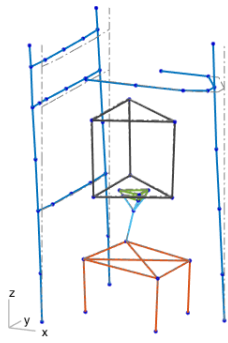
modes corresponding to each encircled peak are investigated. These are the modes that influence the dynamic stiffness measurements. The FE model is therefore updated such that it accurately matches these modes. A comparison of the experimental and updated numerical eigenfrequencies corresponding to each mode is given in Table 4.8, which also includes an explanation of each mode.

Table 4.8: Eigenfrequency comparison per mode of EMA vs. NMA.

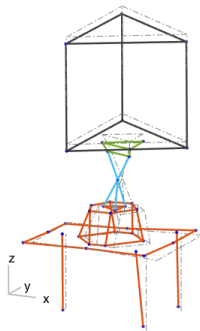
Mode	f_{EMA} [Hz]	f_{NMA} [Hz]	Error [%]	Mode explanation
1	15.6	15.8	1.3	MF rotation R_y
2	21.3	21.6	1.4	MF rotation R_x
3	33.5	33.1	1.2	Frame bending $U_x \rightarrow$ MF and shaker table translation U_z
4	54.4	51.4	5.5	MF translation U_z mode
5	66.3	83.8	26.4	Shaker table rotation R_z on piezo
6	87.0	86.1	1.0	Shaker table translation U_x on piezo
7	123.0	123.3	0.2	Shaker table rotation R_z on piezo
8	460.6	493.0	7.0	Shaker table rotation R_y on piezo
9	556.3	554.4	0.3	Shaker table rotation R_x on piezo
10	665.0	674.7	1.5	Shaker table rotation R_y on piezo
11	1031.0	1106.5	7.3	Shaker table interface bending U_x
12	1486.0	1595.8	7.4	Shaker table internal bending U_z
13	1919.0	2101.7	9.5	Shaker table interface torsion R_z

It can be seen that the updated FE model approximates most of the experimental modes within a 10% error margin. The numerical modes slightly differ from the experimental modes since they can not be tuned separately hence a trade-off had to be made. Figure 4.14 shows a visualization of both the experimental and numerical mode shapes. Note that only mode 3 is experimentally obtained with EMA 1 in which the frame is excited whereas all the other modes are obtained with EMA 2 in which the shaker table is excited.

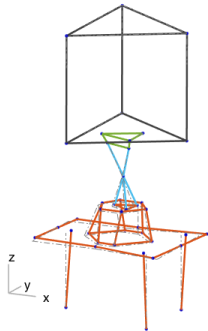




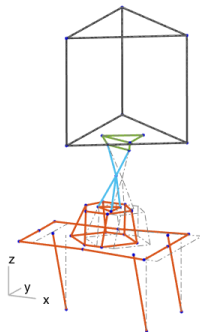
EMA 3: 33.5 Hz



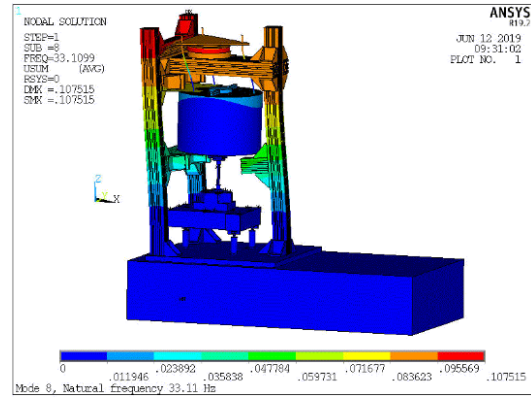
EMA 4: 54.4 Hz



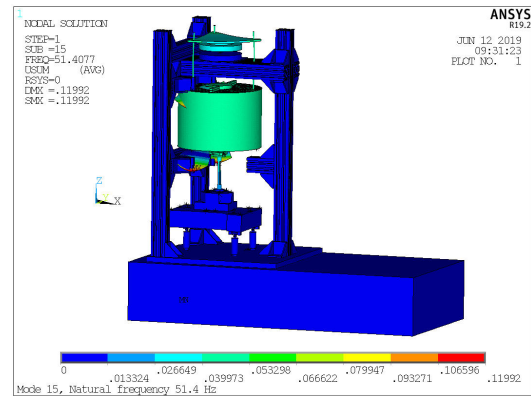
EMA 5: 66.3 Hz



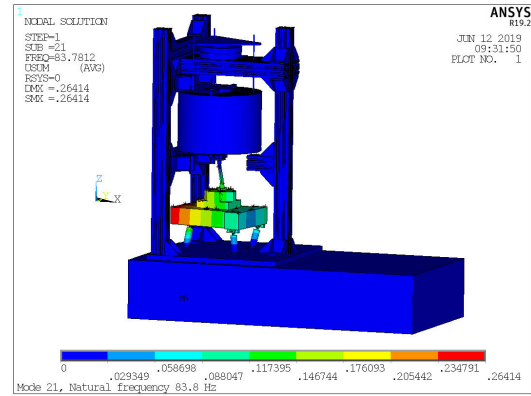
EMA 6: 87.0 Hz



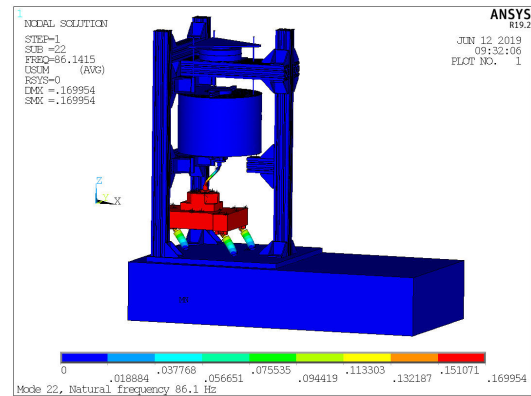
NMA 3: 33.1 Hz



NMA 4: 51.4 Hz

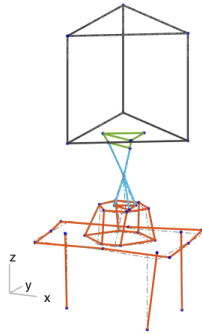


NMA 5: 83.8 Hz

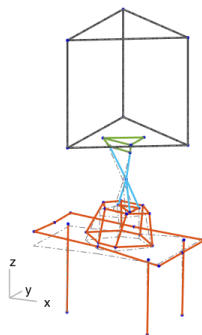


NMA 6: 86.1 Hz

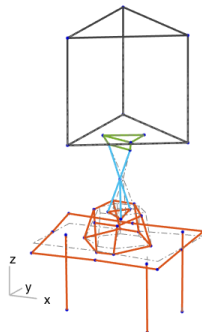
4.3. EXPERIMENTAL VERSUS NUMERICAL RESULTS



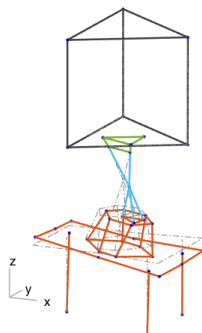
EMA 7: 123.0 Hz



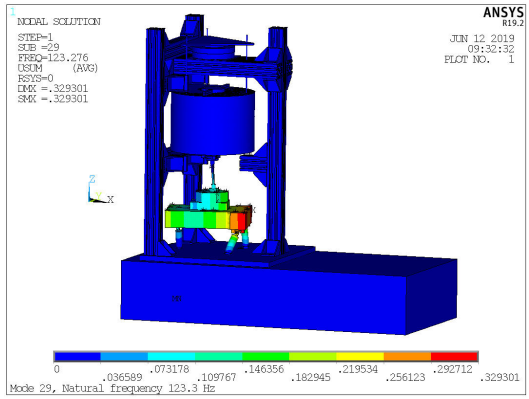
EMA 8: 460.6 Hz



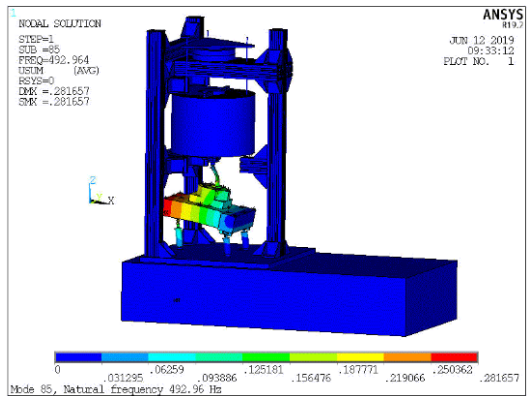
EMA 9: 556.3 Hz



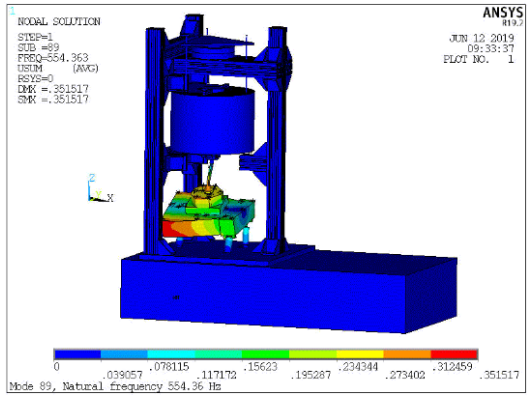
EMA 10: 665.0 Hz



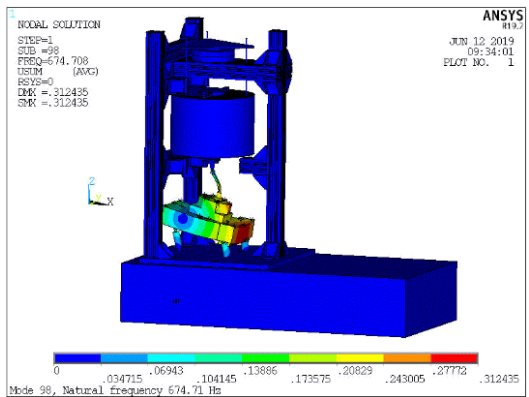
NMA 7: 123.3 Hz



NMA 8: 493.0 Hz



NMA 9: 554.4 Hz



NMA 10: 674.7 Hz

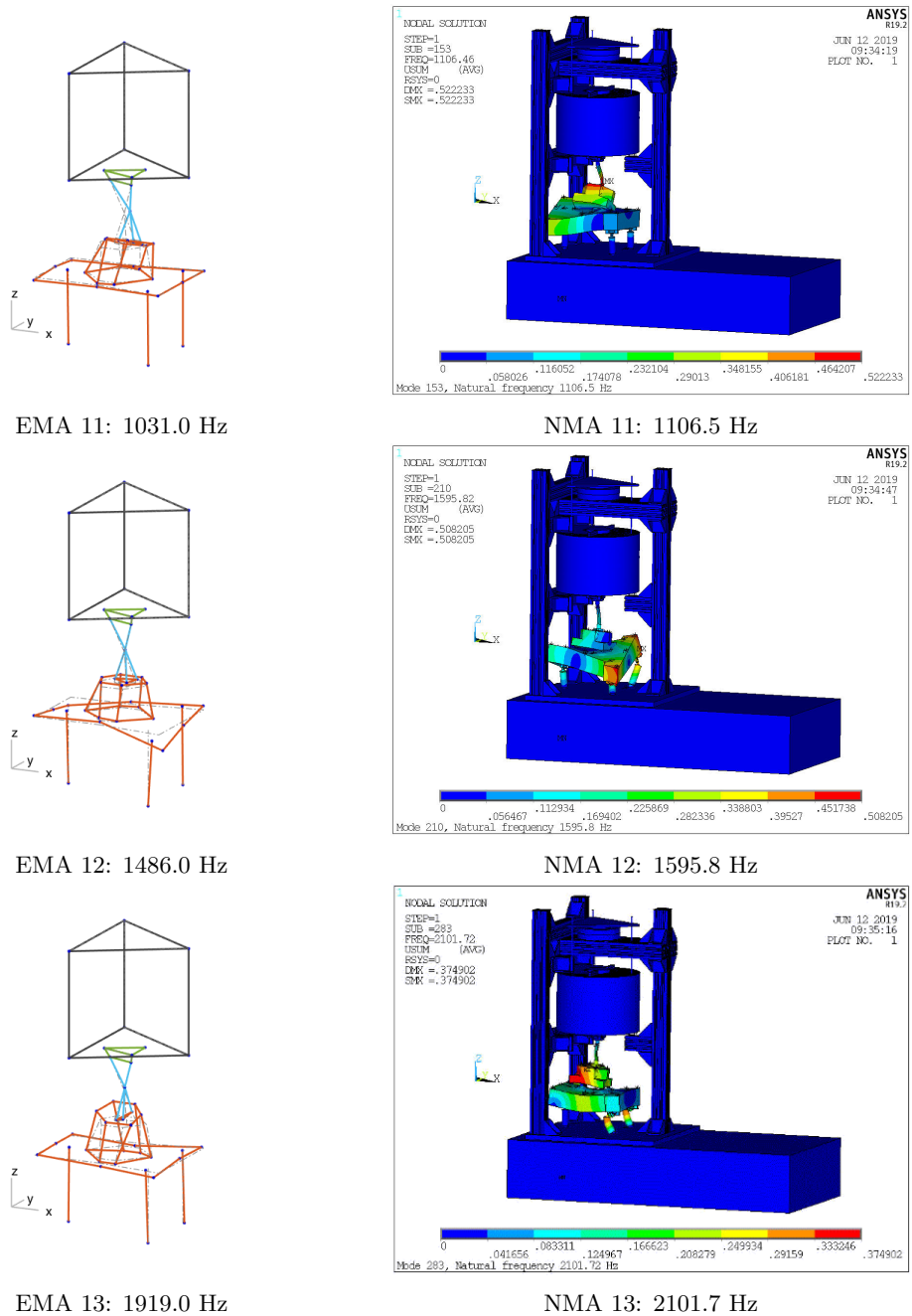


Figure 4.14: Experimental vs. numerical FEM mode shapes.

A clear correlation between the experimental and numerical mode shapes is visualized. The corresponding MAC values are given in Table 4.9 in order to investigate how well these mode shapes are correlated. In this table the diagonal is given in bold and mode 3 at 33.5 Hz is ignored here since it is experimentally obtained with another EMA than all the other mode shapes.

Table 4.9: The MAC values of EMA modes compared to NMA modes.

		NMA eigenfrequencies [Hz]											
		1: 15.8	2: 21.6	4: 51.4	5: 83.8	6: 86.1	7: 123.3	8: 493.0	9: 554.4	10: 674.7	11: 1106.5	12: 1595.8	13: 2101.7
EMA eigenfrequencies [Hz]	Mode												
	1: 15.6	0.67	0.04	0.00	0.01	0.01	0.00	0.00	0.00	0.01	0.01	0.00	0.01
	2: 21.3	0.01	0.78	0.01	0.01	0.03	0.00	0.01	0.00	0.00	0.00	0.00	0.00
	4: 54.4	0.01	0.02	0.18	0.14	0.63	0.00	0.11	0.04	0.15	0.01	0.01	0.00
	5: 66.3	0.00	0.10	0.00	0.97	0.00	0.00	0.00	0.24	0.00	0.04	0.01	0.00
	6: 87.0	0.01	0.00	0.00	0.02	0.97	0.00	0.05	0.00	0.15	0.00	0.00	0.00
	7: 123.0	0.00	0.03	0.00	0.03	0.00	0.98	0.00	0.07	0.00	0.05	0.02	0.00
	8: 460.6	0.00	0.00	0.06	0.00	0.11	0.00	0.95	0.00	0.03	0.00	0.00	0.01
	9: 556.3	0.00	0.08	0.00	0.29	0.01	0.07	0.00	0.94	0.01	0.36	0.04	0.00
	10: 665.0	0.01	0.00	0.03	0.01	0.15	0.00	0.00	0.02	0.95	0.01	0.00	0.02
	11: 1031.0	0.00	0.06	0.00	0.14	0.00	0.05	0.00	0.42	0.00	0.79	0.18	0.00
	12: 1486.0	0.00	0.00	0.01	0.00	0.00	0.02	0.01	0.01	0.02	0.00	0.51	0.01
	13: 1919.0	0.00	0.02	0.02	0.01	0.00	0.00	0.03	0.03	0.02	0.05	0.01	0.41

Note the low MAC value of 0.18 on the diagonal for mode 4 representing the vertical translation mode of the MF. This low MAC value is caused by the influence of mode 5 and mostly mode 6 on the experimental mode shape of mode 4. These modes result in additional horizontal motion of the shaker table on top of the piezos in experimental mode shape 4. It also declares the high MAC value of 0.63 on the off-diagonal position of EMA mode 4 compared to NMA mode 6 representing horizontal translation of the shaker table on top of the piezos. In the FE model this is not the case for mode 4 hence the mode shape results in mainly vertical motion of the MF. If only the motion in the vertical z -direction is considered for this mode a MAC value of 0.77 would be achieved on the diagonal. Furthermore, for the high frequency modes it becomes harder to distinguish and accurately approximate its mode shape with the FE model. Moreover, during the model updating a certain balance had to be found such that as many modes can be predicted as accurately as possible. Note that tuning the model such that a certain mode matches the experimental results might decrease the accuracy of other modes. Further updating can be performed with optimization procedures as for example in [21][22][23][24] and a detailed investigation of material properties, which is a study on its own and beyond the scope of this project. It is also recommended to reduce the model since these simulations are computationally expensive, i.e. 4 hours per simulation to obtain the required amount of modes for the frequency range of interest. Nevertheless, this model is used predict the dynamic stiffness of the test object including the influence of setup related dynamic behavior.

4.3.2 Dynamic stiffness results

After updating the FE model it can be used to imitate the experimental dynamic stiffness measurements. In these simulations an excitation input in z -direction is applied by three piezo actuators underneath the shaker table. This combined input is located such that it inserts excitations right under the test object. The displacement responses in z -direction due to the piezo excitation are measured at the three sensor locations on both the BF and the MF. These displacements are combined to one global displacement for each the BF and MF as is also done for experimental measurement results. The force cell is cut in half and a spring with a high stiffness of $0.33 \cdot 10^{12}$ N/m is modelled in between each of the three force sensors. This is done to determine the three resulting forces with the relative displacements between the top and bottom part of each force sensor and the known stiffness in between. This stiffness is chosen very high to prevent additional dynamics in the frequency range of interest. These three local forces are combined to a global force. The dynamic stiffness can then be determined with the transfer from relative displacement between the MF and BF to the measured force at the force cell. In Figure 4.15 the resulting dynamic stiffness of the FE model with 5% damping is compared to an experimental measurement.

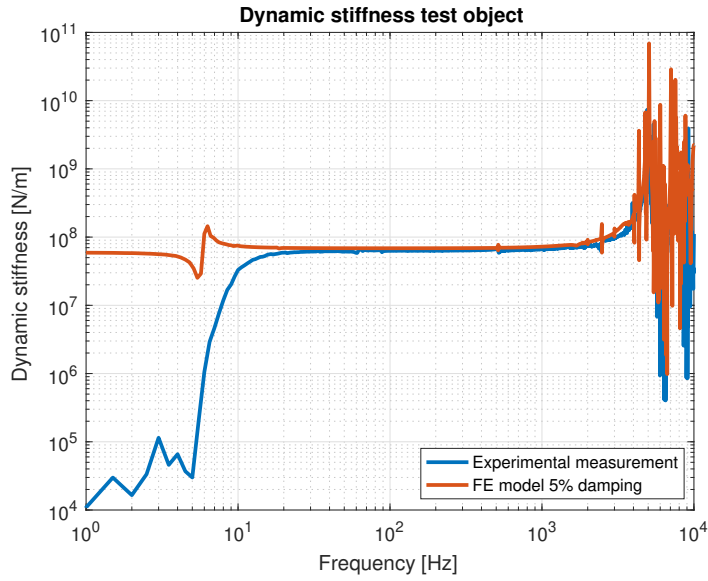
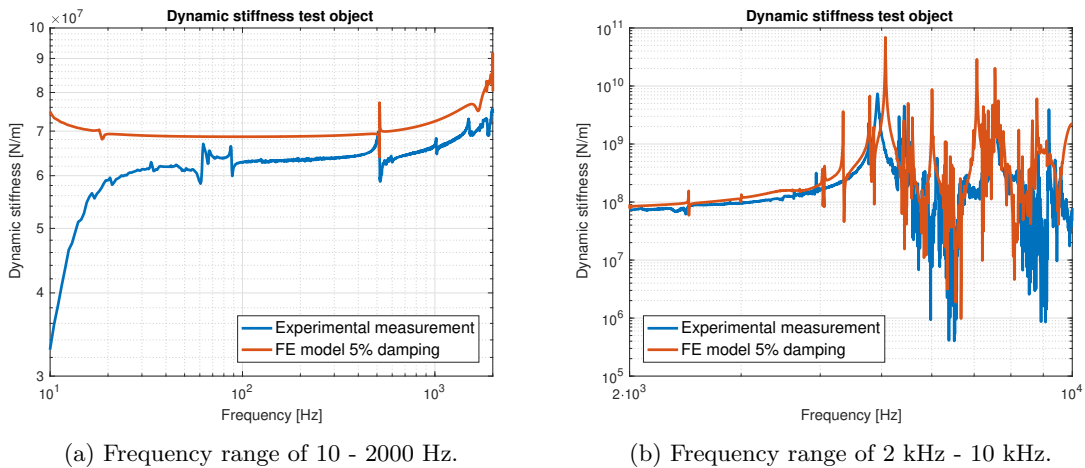


Figure 4.15: Experimental vs. FE model dynamic stiffness.

It can be seen that numerical results globally match the experimental results. For low frequencies until 4 Hz the numerical result equals the static stiffness of $6 \cdot 10^7$ N/m of the test object. At around 5 Hz the MF and BF move in phase such that minimal forces are measured resulting in an anti-resonance peak in both the experimental and numerical results. After 5 Hz the MF and BF start to move out of phase due to the vertical mode of the MF on the test object. Now the measured forces start to increase such that the curves approach the static stiffness of the test object. Note that the FE model is approximately 5-10% stiffer than the experimental results in the static stiffness region, which can be seen more clearly in Figure 4.16a. This is partly caused by the assumption of bonded (stiffer) contacts and differences in material properties. Furthermore, the static stiffness region is lifted due to the dominant resonance peak at 5 kHz originating from the vertical mode of the force cell. This also influences the results in the frequency range of interest. It can be seen that the FE model predicts this mode quite accurately, but if one takes a closer look as in Figure 4.16b the differences are more clear.



(a) Frequency range of 10 - 2000 Hz.

(b) Frequency range of 2 kHz - 10 kHz.

Figure 4.16: Close ups of the dynamic stiffness results.

In the frequency range until 2000 Hz it can be seen that the numerical results show less resonance peaks than the experimental results. A reason for this is that in the numerical simulations purely the global z -direction is considered. No extra rotations are introduced in the FE model since the alignment

between components is perfect which is practically not the case. In experimental measurements the x - and y -direction also influence the results due to crosstalk in for example the force cell. Moreover, for frequencies beyond the 5 kHz mode the measurement becomes unreliable due to decoupling of the force cell. However, the axial 7.6 kHz mode of the test object is still clearly visible and accurately predicted with the FE model.

During the numerical simulations the modal superposition method is applied. Taking more modes into account gives more accurate results but drastically increases the computation time. In the shown results 2500 modes (until ≈ 10 kHz) are taken into account in order to obtain the dominant high frequency modes as well. These simulations require a huge amount of disk space and they are computationally demanding. It is therefore recommended to further reduce the model by applying a model reduction technique in a future study. Additionally, the model can be further updated to increase the accuracy of simulation results. Nonetheless the current model can be used to obtain useful results from simulations with other objects mounted in the setup, for example an airmount. This is however not verified yet, but is outside the scope of this study. The current FE model can also be used to investigate the influence of applying improvements to the setup.

4.4 Discussion

Several experimental measurements are performed to validate and update the numerical models as introduced in Chapter 3. Initially, the numerical model of the test object is experimentally validated by performing an experimental modal analysis. This is done for the free-free case, which is experimentally imitated by placing the test object on a soft egg-shaped foam. The numerical results differ somewhat from the experimental results. These differences are due to the fact that the boundary conditions are not totally free-free during EMA, material and damping properties differ, and experimental excitation is not perfectly aligned and consistent whereas numerically it is. The errors are negligibly small though.

After validating that the test object is correctly modelled and manufactured it is mounted in the setup in order to perform dynamic stiffness measurements with it. Firstly, the influence of several BF sensor locations on the measurement results is investigated in order to obtain the most reliable measurement data. The outcome shows that additional resonance peaks are measured by placing the BF accelerometers on the shaker table due to internal dynamics. From this it can be concluded that placing the BF accelerometers on the shaker table interface gives the most reliable results. These results are also the most representative in comparison with the expected results from the numerical models. With these locations a repeatability test is executed showing that consecutive measurement results match. Repeatability is significantly worse when measurements are performed non-consecutively for which the bellow is re-inflated and the sensors are moved and reattached. It is therefore relevant to consistently inflate the bellow and place the sensors.

In the dynamic stiffness measurement results it can be seen that for low frequencies until 5 Hz the measurement quality is poor due to the great influence of noise. This can be explained by the fact that the MF follows the motion of the BF due to the high stiffness of the test object, hence low forces are measured as well as small relative displacement. At around 5 Hz the MF and BF move exactly in phase causing an anti-resonance in the measured forces. Afterwards, the MF starts to decouple due to the influence of the vertical mode of the MF on the stiffness of mainly the test object and thereby the relative displacement increases. The measured force starts to increase until the static stiffness of the test object is approximately reached and the measurement quality improves. For typical vibration isolation systems such as airmounts the MF decouples at a lower frequency since the stiffness is significantly lower. In this case the poor measurement quality for low frequencies is moved to the left on the frequency axis preventing or reducing this problem in the frequency range of interest. Moreover, the dominant resonance peak of the force cell at 5 kHz greatly influences the measurement in a large frequency range and also a part of the frequency range of interest. Further dynamic behavior influencing the measurement results in this frequency range is only clearly visible when zoomed in on this part. This behavior has been investigated by performing experimental modal analysis as a next step.

The results of this EMA clarify that mainly the dynamic behavior of the shaker table configuration influences the measurement results in the frequency range of interest. For the lower frequencies this

influence originates from the rigid body movements of the shaker table on top of the piezo actuators. For the higher frequencies above 1000 Hz the internal dynamic behavior of the shaker table starts to play a role and influences the measurement results. With the aid of these experimental results the numerical FE model is updated such that it better represents the experimental data. The tuned model quite accurately predicts the true behavior, but further model updating that might improve accuracy can be applied with optimization procedures as for example in [21][22][23] and is a study on its own. In this study the updated model is used to imitate dynamic stiffness measurements and results are compared to experimental measurements. The outcome shows that the model is slightly stiffer than reality, but globally it results in a quite accurate approximation of the experimental data. The disadvantage is the high computational time when many modes have to be taken into account for the modal superposition method. This problem can be reduced by applying a model reduction technique as for example introduced in [25] or with component mode synthesis as in [17][19][20][26]. The latter is also shortly elaborated in Appendix C.

Nevertheless, the current FE model enables to test the influence of changes made to the setup in the model prior to practical implementation. This makes testing the influence of possible improvements to the setup cost-efficient. Moreover, the FE model can probably be used to obtain reliable predictions from numerical simulations with other objects mounted in the setup, e.g. an airmount. However, this is not tested yet.

Chapter 5

Conclusions and recommendations

In this research the dynamic stiffness measurement setup is validated in the frequency range of interest of 1 - 2000 Hz. With the findings of this validation some proposals for improvement of the setup are given. This chapter elaborates on the conclusions that follow from this research and the recommendations for future work.

5.1 Conclusions

In this thesis the dynamic stiffness measurement setup is validated by investigating the influence of its dynamic behavior on the dynamic stiffness measurements. Note that this refers to the first research goal. It is achieved by initially designing a test object according to specific requirements. This object is used to simplify the investigation of which part of the measured dynamic stiffness response originates from the object under test and which part from setup artifacts. As a first step, the dynamic stiffness of the test object is determined with numerical models of the test object and a mass-spring model of the setup. These models are experimentally validated with dynamic stiffness measurement results. From these results it can be concluded that the relatively simple numerical models can be used for reliable initial predictions.

The influence of BF accelerometer locations on the dynamic stiffness measurement results are investigated in order to obtain the most reliable results. After this study it is concluded that placing the BF accelerometers on the shaker table interface rather than on the shaker table itself is the best option. Otherwise, the internal dynamic behavior of the shaker table significantly affects the measurement response. Also a repeatability test is performed from which it can be concluded that consistently inflating the bellow and placing the sensors is important to achieve consistent results.

In addition to experimental validation, the results of the dynamic stiffness measurements are used to investigate at which frequencies the measurements are influenced by the dynamic behavior of the setup. This behavior is investigated by performing an EMA on the setup. From this analysis it is concluded that mainly the dynamic behavior of the shaker table configuration and the force cell influence the measurements. The rigid body motions of the shaker table on top of the piezo actuators cause some small resonance peaks in the dynamic stiffness response below 1000 Hz. From 1000 Hz onwards internal dynamic behavior of the shaker table starts to slightly influence the measurements. Lastly, the dominant vertical mode of the force cell at 5 kHz has a big influence on the measurement since it lifts the static stiffness line already in the frequency range of interest. Beyond the 5 kHz resonance frequency of this mode the measurement becomes unreliable, but the vertical mode of the test object at around 7.6 kHz can still be distinguished from the noisy signals.

Finally, a FE model is made and updated with the aid of the EMA results in order to obtain a valid and representative model. By comparison of the EMA and NMA results it can be concluded that the numerical FE model accurately represents the true experimental behavior within a 10% error margin for most modes. The purpose of the FE model is threefold. Firstly, it enables the prediction of the dynamic behavior of the setup with any object mounted in the setup. It can be concluded that the dynamic behavior of the setup with the test object mounted in it can be accurately predicted. Secondly, it can be used to imitate the dynamic stiffness measurements with any object mounted

in the setup in order to verify that setup dynamic behavior has minimal influence on the dynamic stiffness measurement. The dynamic stiffness measurements of the test object are imitated with the FE model. These results are globally accurate compared to the experimental results, but the FE model is slightly stiffer. Only pure global vertical z -directions are taken into account which is not true in practice. Thirdly, the FE model enables to numerically test changes made to the setup prior to practical implementation. One big disadvantage at the moment, however, is the high computational costs of the full FE model.

Overall it can be concluded that the dynamic stiffness measurement setup in its current state already performs quite reliable measurements. However, some proposals for improvement of the dynamic stiffness measurement setup are found and are discussed in the recommendations.

5.2 Recommendations

Referring to the second research goal, some improvements of the dynamic stiffness measurement setup can be proposed as recommendations. From the EMA and dynamic stiffness measurements it has been concluded that the dominant 5 kHz resonance behavior of the force cell has a widely spread influence on the dynamic stiffness measurement results. Also, the rigid body movements of the shaker table on top of the piezo actuators and the internal dynamic behavior of the shaker table influence the dynamic stiffness response in the frequency range of interest. It is therefore recommended to design a stiffer and lighter force cell, shaker table, and shaker table interface. This can be achieved by for example re-designing the geometries and changing material properties. As a result, most of the resonance peaks related to dynamic behavior of the setup will shift outside the frequency range of interest. This will, however, not apply to the modes caused by rigid motions of the shaker table on top of the piezo actuators. Damping the movements of these modes is recommended in order to reduce the influence of the corresponding dynamic behavior on the dynamic stiffness response.

During the repeatability test it was found that consistently pressurizing the bellow is important for obtaining similar measurement results. A tyre air compressor with an analogue pressure gauge is used to pressurize the bellow. This way of reading the pressure is inaccurate and could be improved by using a pressure regulator to control the bellow pressure to a desired value. For repetitive measurements, it is also relevant to fixate the sensors at the exact same locations since sensor locations greatly influence the measurement results. These sensors are currently placed at almost the same locations using a ruler for approximate alignment. It would be more convenient to mark or precisely define the correct sensor locations such that they are consistently aligned and positioned.

Combining the three local BF accelerations to one global acceleration is done by assuming rigid transformations while the shaker table shows flexible behavior. This introduces inaccuracies that might affect the measurement results and should be compensated for in future research. Compensation requires one additional sensor for each additional flexible mode to be compensated for. Furthermore, the influence of measuring the BF and MF accelerations with 6 DOFs instead of 5 DOFs (by including rotations R_z) as well as the effect of crosstalk in the force cell and crosstalk due to imperfect alignment of setup components should be investigated in a future study. There is also a wish to investigate the effect of using a multisine instead of white noise excitation input. This could improve the signal-to-noise ratio and thereby the measurement results since multisine excitation: has a user-defined constant amplitude rather than a randomly defined amplitude spectrum, has a better distribution of excitation energy, and the signal is periodic.

Finally, some recommendations regarding the FE model are suggested for future work. It is concluded that the FE model quite accurately predicts the true behavior, but further model updating might improve accuracy and can be applied with optimization procedures as for example in [21][22][23][24]. Another recommendation is to investigate the material properties of the piezo actuators and the bellow, which are currently tuned by hand. The disadvantage of the current FE model is the high computational time when many modes are taken into account for the modal superposition method. This problem can be reduced by applying a model reduction technique as for example introduced in [25] or with component mode synthesis as in [17][19][20][26] and shortly elaborated in Appendix C. Moreover, it would be satisfactory to have a modular FE model which can be employed to: perform valid simulations with other objects mounted in the setup for example an airmount, and obtain reliable predictions with numerical setup improvements prior to practical implementation.

Bibliography

- [1] Mack, C.A. (2006), Field Guide to Optical Lithography. *SPIE Press*, Bellingham, Washington USA.
- [2] Palmer, K.M. (2012), An extremely fine line. *IEEE Spectrum*, 49(1), 47-50. doi: 10.1109/MSPEC.2012.6117838
- [3] Ding, C. (2013), Vibration isolation control of a contactless electromagnetic suspension system. *PhD Thesis*, Eindhoven University of Technology. DOI: 10.6100/IR757779
- [4] ASML. *Company - Our history*, September 10, (2018). Retrieved from URL: <https://www.asml.com/company/our-history/en/s277?rid=51985>
- [5] Butler, H. (2008), A perspective on stage dynamics and control. In *Proceedings of the APSE 2008 Spring Topical Meeting - Precision Mechanical Design and Mechatronics for Sub-50 nm Semiconductor Equipment*, Berkeley, California USA.
- [6] Huiskamp, M. (2015), Airmounts XT4 and NXT1/2/3. *Knowledge Transfer Airmounts - Power-Point*, ASML.
- [7] Uz, C. (2013), Design of a test setup for characterization of vibration isolators. *Master Thesis*, Middle East Technical University.
- [8] Salgado, J., Meireles, J. (2013), Study of the experimental modal analysis techniques applied to structural dynamics. *IOMAC - 5th International Operational Modal Analysis Conference*, Guimaraes.
- [9] Pasha H.G., Allemang R.J., Phillips A.W. (2014), Techniques for Synthesizing FRFs from Analytical Models. In: *Foss G., Niezrecki C. (eds) Special Topics in Structural Dynamics*, Volume 6. Conference Proceedings of the Society for Experimental Mechanics Series. Springer, Cham.
- [10] Kraker, B. (2004), A Numerical - Experimental Approach in Structural Dynamics. *Shaker Publishing*, Maastricht, ISBN: 90-423-0259-3.
- [11] Agilent Technologies. The Fundamentals of Modal Testing. *Application Note 243 - 3*.
- [12] Avitabile, P. (2001), Experimental Modal Analysis - A Simple Non-Mathematical Presentation. *Sound and Vibration*, University of Massachusetts, 35(1), 20-31.
- [13] Kumar, S.M. (2008), Analyzing Random Vibration Fatigue - Powerful ANSYS Workbench tools help calculate the damage of vibrations that lack straightforward cycle repetition. *ANSYS Advantage*, 2(3), 39-42.
- [14] Allemang, R.J., Brown, D.L. (2006), A Complete Review of the Complex Mode Indicator Function (CMIF) with Applications. *Structural Dynamics Research Laboratory*, Mechanical, Industrial and Nuclear Engineering, University of Cincinnati.
- [15] Phillips, A.W., Allemang, R.J., Fladung, W.A. (1998), The Complex Mode Indicator Function (CMIF) as a Parameter Estimation Method. *SPIE the 16th International modal analysis conference*, 3243(1), 705-710.

- [16] Sharcnet. *Stress Stiffening*, February 13, 2019. Retrieved from URL: https://www.sharcnet.ca/Software/ANSYS/17.2/en-us/help/ans_thry/thy_geo3.html
- [17] Voormeeren, S.N. (2012), Dynamic Substructuring Methodologies for Integrated Dynamic Analysis of Wind Turbines. *PhD Thesis*, Delft University of Technology. ISBN 978-94-91104-10-7.
- [18] Majed, A. (2015), A Unified Approach to Modal Reduction Methods. *Nesc Academy Webcast*, Web lecture.
- [19] Sharcnet. *Component Mode Synthesis*, February 13, 2019. Retrieved from URL: https://www.sharcnet.ca/Software/ANSYS/16.2.3/en-us/help/ans_substr/advcms.html
- [20] Herting, D.N. (1985), A general purpose, multi-stage, component modal synthesis method. *Finite Elements in Analysis and Design 1*, pp. 154-164.
- [21] Girardi, M., Padovani, C., Pellegrini, D., Porcelli, M. and Robol, L. (2018), Finite element model updating for structural applications. *Cornell University*. arXiv:1801.09122v2.
- [22] Zivanovic, S., Pavic, A. and Reynolds, P. (2007), Finite element modelling and updating of a lively footbridge: the complete process. *Journal of Sound and Vibration*, Vol. 301, No. 1-2, pp. 126-145. doi:10.1016/j.jsv.2006.09.024
- [23] Mottershead, J.E. and Friswell, M.I. (1993), Model updating in structural dynamics: a survey. *Journal of Sound and Vibration*, 167(2), 347-375. doi: 10.1006/jsvi.1993.1340
- [24] Mottershead, J.E., Link, M. and Friswell, M.I. (2011), The sensitivity method in finite element model updating: A tutorial. *Mechanical Systems and Signal Processing*, 25(7), 2275-2296. doi: 10.1016/j.ymssp.2010.10.012
- [25] Jensen, H.A., Millas, E., Kusanovic, D. and Papadimitriou, C. (2014), Model-reduction techniques for Bayesian finite element model updating using dynamic response data. *Computer methods in applied mechanics and engineering*, Vol. 279, 301-324.
- [26] Verlinden, O. (2005), Computer-aided analysis of rigid and flexible multibody systems (Part II). Component mode synthesis of flexible bodies. *Graduate School in Mechanics*, KU Leuven.

Appendix A

Dynamic stiffness setup

A.1 Background

The background of ASML's dynamic stiffness measurement setup is as follows. In 2014 a project was started where ASML collaborated with PInS. The aim was to increase NXE MF dynamic robustness, because it was observed in different ways that NXE machines showed quite some performance variation in dynamics. The main approach to increase robustness is to decrease the propagation of all BF-borne disturbances by improving the BF to MF coupling. Therefore, a test setup was developed at PInS to measure dynamic stiffness of airmounts and dynamic links. Afterwards, the test setup was transferred to ASML and build up again with a lot of changes in the equipment except for the force cell to make the setup operational again. These changes are listed in Table A.1 for each component. Note that the changes are coloured red.

Table A.1: Changes in setup equipment ASML vs. PInS.

Component	ASML	PInS	Comment
Piezo (vertical)	PI P225.40	PI P242.40	ASML piezo has 2x higher stiffness
Piezo amplifier	PI E472.20	PI E472.00	PInS is older model; connector and polarity different
Shaker (horizontal)	Tira TV 51120	B&K 4809	ASML: hanging in crane, PInS: on separate table
Shaker amplifier	Tira E120	B&K 2718	-
Accelerometers	B&K 4381 PCB356B18 PCB356M98	B&K 4379 PCB 356B18	-
Force cell	Kistler 9027C	Kistler 9027C	3x3 DOF force cell combined to 6 DOF force
Signal conditioning	B&K 2692 B&K 2693	B&K 2692 B&K 2693	ASML filtering: 0.1 Hz High pass + 3 kHz Low pass
Data acquisition	dSPACE 1007	dSPACE 1103	-
Sampling frequency	50 kHz	10 kHz	-

The interfacing for operating the setup is done through dSPACE. This consists of three components: the connection board, the dSPACE system running the real time model, and the desktop PC for interfacing. Furthermore, a MATLAB Simulink model of what is desired to be measured and controlled has to be build which will be loaded into dSPACE. In the dSPACE control desk parameters can be adjusted and measurements can be performed.

A.2 Setup pictures

In Figure A.1 the whole setup is shown first including the names of its components again.

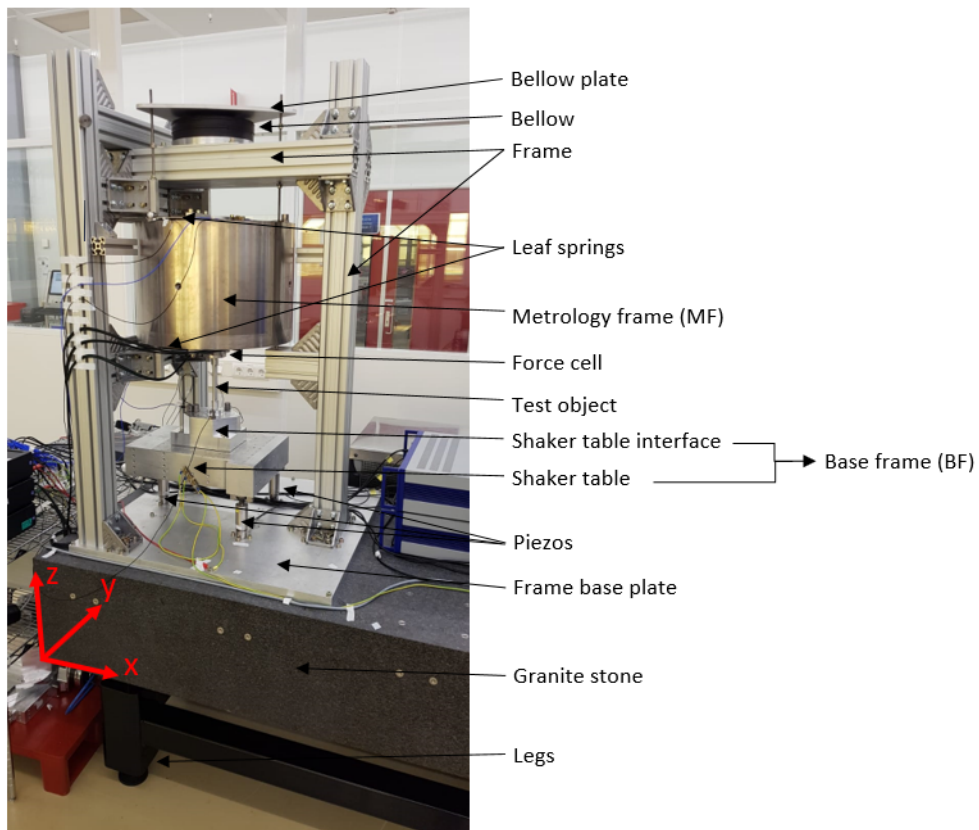


Figure A.1: The whole setup including names.

Some extra detailed pictures of the setup are shown next. This is done in the order from the bottom of the setup to the top starting with the granite stone and its (passive vibration isolation) legs as shown in Figure A.2.

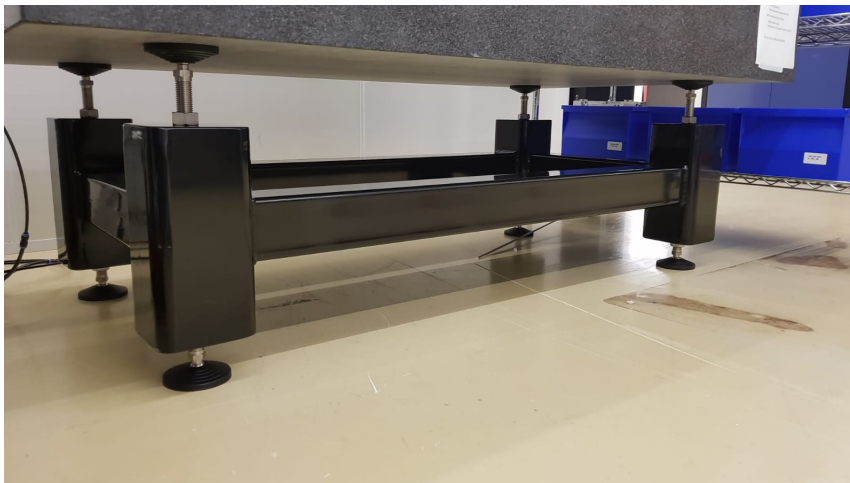


Figure A.2: The granite stone and legs.

On top of the granite stone the frame and its base plate are mounted on which the shaker table and its interface on the three piezo actuators are placed. This is shown in Figure A.3 where also a close up of a single piezo actuator with its tip is shown.

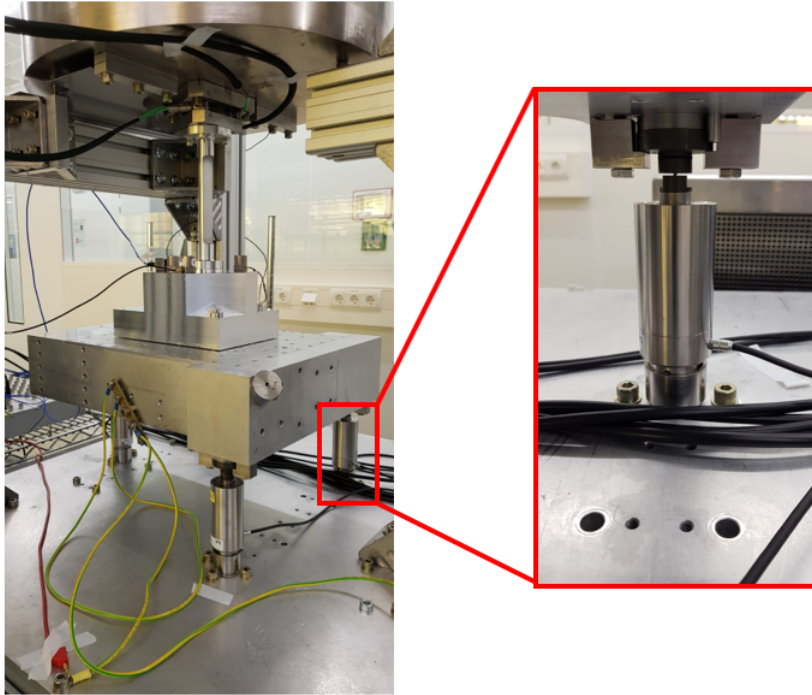


Figure A.3: The shaker table on three piezo actuators and a close up of a single piezo.

Note that the test object is mounted between the shaker table interface and the force cell. Figure A.4 shows a close up of the FC which is mounted at the bottom of the MF.

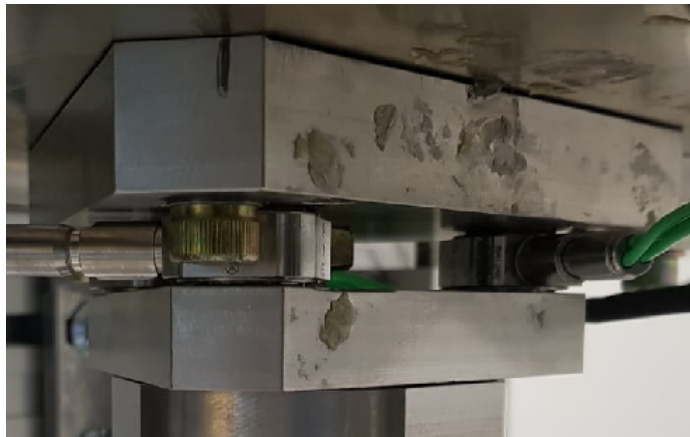


Figure A.4: A close up of the force cell.

The bottom of the MF is shown in Figure A.5. Also close ups of the end stops of the MF can be seen on which it can rest.

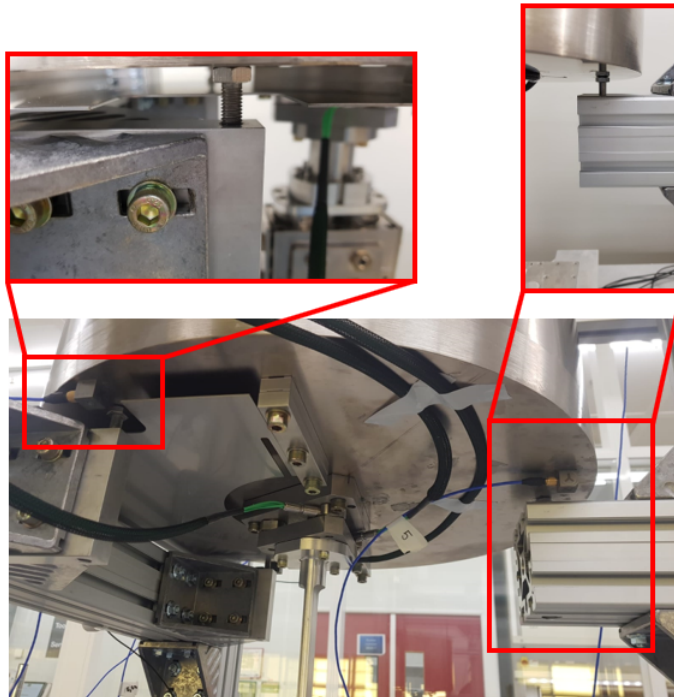


Figure A.5: The bottom of the MF showing the force cell and close ups of some end stops.

Note that the bottom leaf spring is also shown and the saw cuts can be seen. In Figure A.6 the leaf spring is shown from the other side where also a cut can be seen to reduce stiffness.

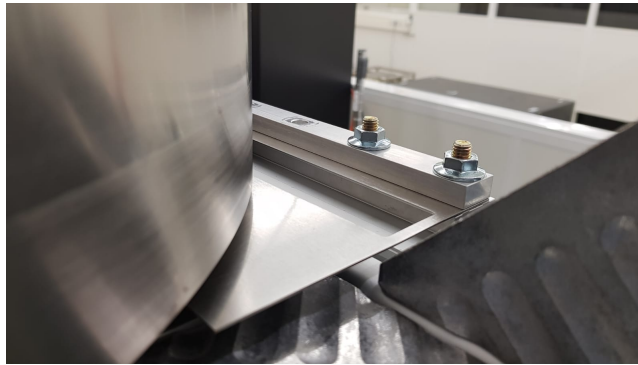


Figure A.6: The other side of the bottom leaf spring.

Figure A.7 shows the top of the MF. The top leaf spring can also be seen which contains the same saw cuts as the bottom leaf spring.

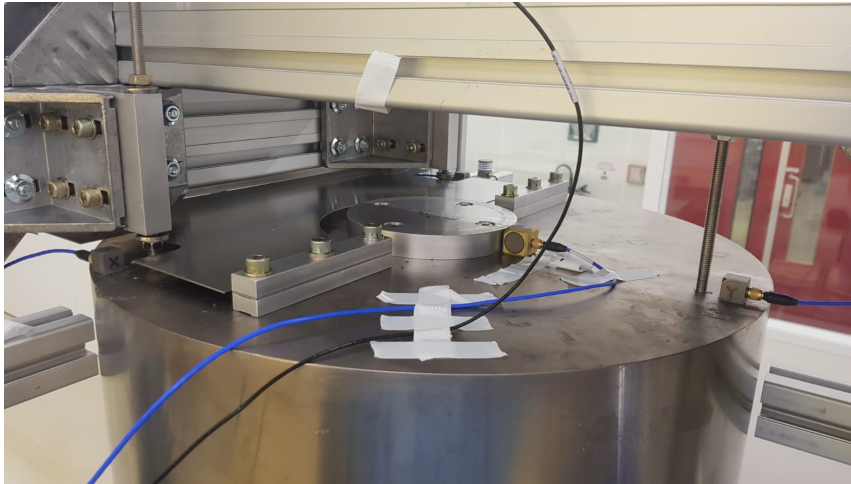


Figure A.7: The top of the MF showing the leaf spring as well.

Note the MF end stops of the frame on the left and right and also the end stop nuts on the threaded rods. On top of the frame a bellow is placed as shown in Figure A.8. This bellow can be inflated with a tyre air compressor.

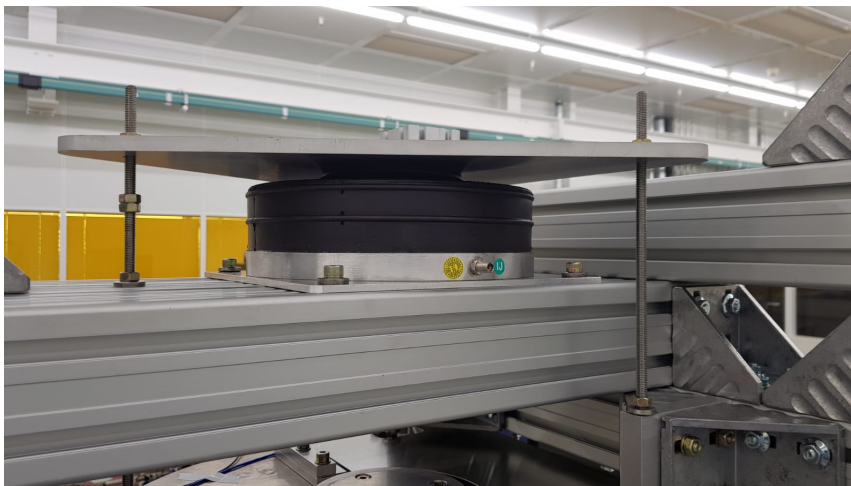


Figure A.8: The bellow on top of the frame.

On top of the bellow a plate is mounted such that when the bellow gets inflated it lifts the mass of the MF. This can be used to set the correct preload of a specific vibration isolation situation. Lastly, the nexus data acquisition systems and the dSPACE connection board is shown in Figure A.9.

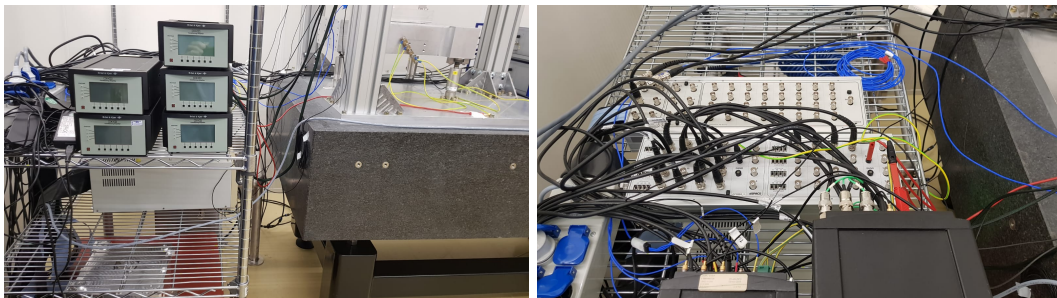


Figure A.9: The Nexus data acquisition systems (left) and the dSPACE connection board (right).

Appendix B

Test object designs

Before manufacturing the test object, it has to be designed according to some requirements. With these requirements an initial design is made which is optimized in the design process, resulting in several designs as shown in Figure B.1 for initial to final design from left to right. The optimization is based on manufacturability, asymmetry such that x and y modes do not coincide, and numerical modal analysis and dynamic stiffness results. The first design is a simple rigid rod. To get rid of symmetry, design 2 contains two short and narrow slits: one in xz -plane and one in yz -plane. Design 3 has one long and narrow slit in yz -plane. Design 4 has two notches in yz -plane and design 5 is similar to design 4, but with a smaller diameter. Finally, radii at the top and bottom between the rod and the interfaces are added to design 5 for ease of manufacturability resulting in final design 6.

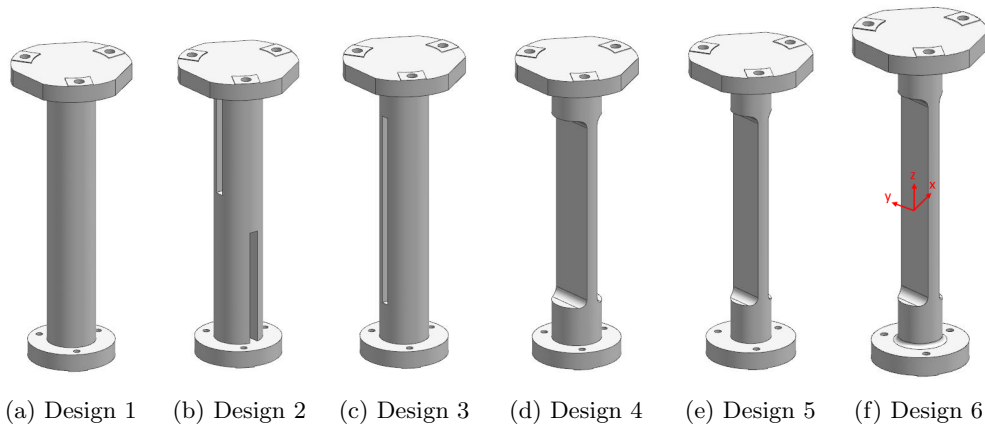


Figure B.1: Design optimization steps.

The initial design results in similar x and y modes which can hardly be distinguished from each other. Therefore, from initial to final design the test object becomes more asymmetric by adding slits in the rod such that x and y modes can easier be distinguished from each other. Also, from initial to final design the manufacturability becomes easier and therefore quicker and cheaper. Furthermore, the diameter decreased after design 4 to prevent numerical instabilities while calculating the dynamic stiffness with the mass-spring method. The final design of the test object is manufactured with the following specifications:

- Aluminum with Young's modulus $E = 70 \cdot 10^9$ Pa and density $\rho = 2710$ kg/m³ is chosen, resulting in a total weight of 0.327 kg.
- The total length of the object is 197.5 ± 1 mm, where the height of the top contact faces is 0.5 ± 0.1 mm, the top interface 10.75 ± 0.25 mm, the rod 175 ± 0.3 mm, the bottom interface 10.75 ± 0.25 mm and the bottom contact faces 0.5 ± 0.1 mm. This adds up to 197.5 ± 1 mm.

- The top interface was initially circular with a diameter of 76 mm. Afterwards, the circular shape has been cut according to the setup interface to which it will be attached as shown in Figure B.2. This is done for correct alignment and the three holes are positioned such that they match with the holes in the setup top interface.
- The bottom interface is circular with a diameter of 55 mm with three holes such that it fits with the bottom interface of the setup and it aligns with the top attachment.

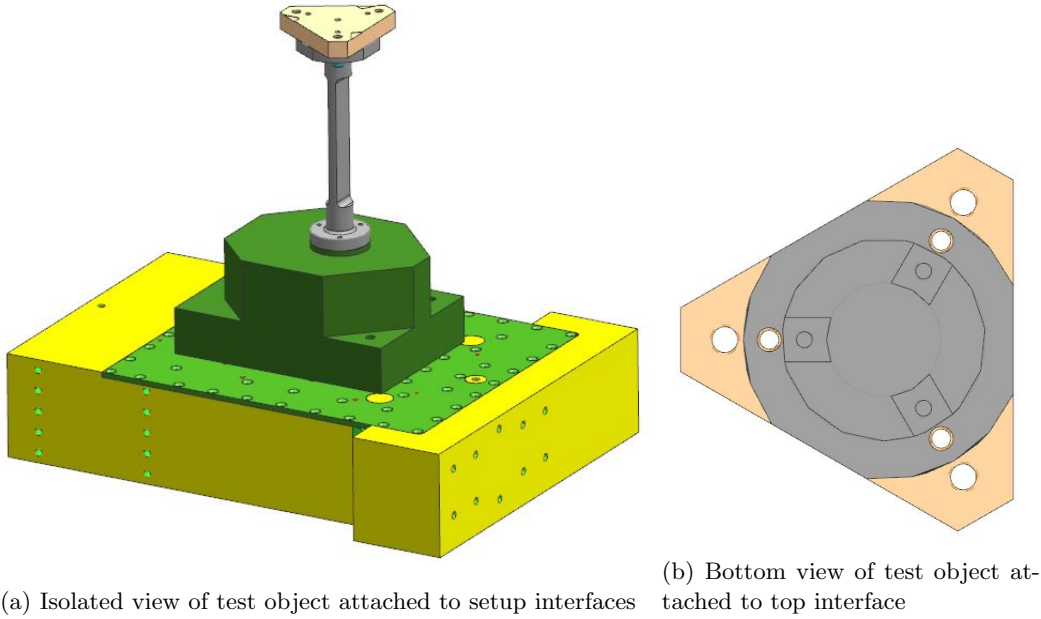


Figure B.2: The test object attached to the setup.

B.1 Modal analysis

Numerical modal analysis is performed in ANSYS to ensure that the first requirement is fulfilled. The constraints during this modal analysis are: the three bottom and three top contact surfaces are fully fixed, i.e. $U_x = U_y = U_z = R_x = R_y = R_z = 0$, for both top and bottom contact surfaces with U the displacements and R the rotations. The resulting eigenfrequencies of each design are given in Tables B.1, B.2, B.3, B.4, B.5, and B.6 including a description of each eigenmode.

Table B.1: Modal analysis of the design 1.

Mode	Eigenfrequency [Hz]	Description
1	2786.6	First bending in x -direction
2	2787.0	First bending in y -direction
3	6541.7	Axial in z -direction
4	6928.8	Rotation around x -axis
5	6928.9	Rotation around y -axis
6	8254.4	Rotation around z -axis
7	10381.2	Second bending in x -direction
8	10382.9	Second bending in y -direction
9	13832.4	Third bending in x -direction
10	13833.2	Third bending in y -direction

Table B.2: Modal analysis of design 2.

Mode	Eigenfrequency [Hz]	Description
1	2077.8	First bending in x -direction
2	2148.9	First bending in y -direction
3	5049.3	Rotation around z -axis
4	5956.5	Second bending in x -direction
5	6326.0	Second bending in y -direction
6	6527.3	Slit modes in x - and y -direction
7	7080.9	Bottom slit mode in x -direction
8	7302.5	Top slit mode in y -direction
9	7767.5	Third bending in y -direction
10	8991.5	Third bending in x -direction

Table B.3: Modal analysis of design 3.

Mode	Eigenfrequency [Hz]	Description
1	2444.8	First bending in y -direction
2	2896.6	First bending in x -direction
3	3130.1	First slit mode in y -direction
4	4830.0	Second bending y -direction
5	5425.7	First slit mode in x -direction
6	6864.6	Axial in z -direction
7	6900.0	Second bending in x -direction
8	7803.7	Rotation around z -axis
9	8078.0	Third bending in y -direction
10	8221.8	Second slit mode in y -direction

Table B.4: Modal analysis of design 4.

Mode	Eigenfrequency [Hz]	Description
1	2280.0	First bending in x -direction
2	3814.0	First bending in y -direction
3	4979.3	Second bending in x -direction
4	6306.9	Rotation around z -axis
5	7032.3	Third bending in x -direction
6	7585.8	Second bending in y -direction
7	7641.1	Axial in z -direction
8	9553.0	Fourth bending in x -direction
9	10651.0	Third bending in y -direction
10	12753.5	Second rotation around z -axis

Table B.5: Modal analysis of design 5.

Mode	Eigenfrequency [Hz]	Description
1	2167.2	First bending in x -direction
2	3332.2	First bending in y -direction
3	4742.8	Second bending in x -direction
4	6777.8	Third bending x -direction
5	6842.3	Second bending in y -direction
6	7186.7	Rotation around z -axis
7	7682.1	Axial in z -direction
8	9093.1	Fourth bending in x -direction
9	9288.5	Third bending in y -direction
10	11858.8	Fifth bending in x -direction

Table B.6: Modal analysis of design 6 (final design).

Mode	Eigenfrequency [Hz]	Description
1	2193.8	First bending in x -direction
2	3410.4	First bending in y -direction
3	4841.1	Second bending in x -direction
4	6904.7	Third bending x -direction
5	6959.0	Second bending in y -direction
6	7197.3	Rotation around z -axis
7	7811.5	Axial in z -direction
8	9259.6	Fourth bending in x -direction
9	9488.2	Third bending in y -direction
10	12130.3	Fifth bending in x -direction

Initially, design 1 results in coinciding x and y modes due to symmetry and design 2 experiences the same problem. Next, design 3 is more asymmetric and therefore x and y modes can be distinguished. Due to the ease of manufacturability design 4 is made and results in even better distinction between x and y modes, but it encounters numerical instability during the determination of dynamic stiffness. The latter is caused by the fact that high spring stiffness and point mass values are required for the mass-spring method, because of the high stiffness of the test object. Therefore, the stiffness is reduced by decreasing the diameter resulting in design 5 for which modes are closer together but can still be distinguished. Finally, adding radii results in higher stiffness and therefore design 6 has somewhat higher eigenfrequencies compared to design 5. Note that for the final design the eigenfrequency of mode 1 is higher than 2000 Hz and results from bending in the weakest direction. During actual experiments the desired measurement direction is vertically in z -direction for which its first mode is found at 7811.5 Hz. However, measurements in z -direction might be influenced by resonance behaviour in other directions. Therefore, the lowest eigenfrequency in any direction is designed to be above 2000 Hz.

Appendix C

Model reduction

For complex geometries with a large amount of DOFs it is desired to create an accurate, reduced dynamic model of the system in a frequency range of interest. Such a reduced model can for example be derived by coupling of superelements, i.e. system components, with a reduced number of DOFs. The motivation to reduce the number of DOFs is to reduce computational times for dynamic analyses while retaining sufficient accuracy. Therefore, the general procedure to reduce the number of DOFs is explained first. The equations of motion of a linear undamped mechanical system are defined as

$$\mathbf{M}\ddot{\underline{q}}(t) + \mathbf{K}\underline{q}(t) = \underline{f}(t), \quad (\text{C.1})$$

where $\mathbf{M}, \mathbf{K} \in \mathbb{R}^{n \times n}$ are respectively the mass and stiffness matrices with n the total number of DOFs, and $\underline{f}, \underline{q} \in \mathbb{R}^{n \times 1}$ respectively the load and physical DOFs columns. Reduction is achieved by a coordinate transformation where $\underline{q}(t)$ is approximated with a linear combination of n_p Ritz columns \underline{t}_i such that:

$$\underline{q}(t) \approx \sum_{i=1}^{n_p} \underline{t}_i p_i(t) = \mathbf{T}\underline{p}(t), \quad (\text{C.2})$$

with n_p the number of generalized DOFs, $\mathbf{T} \in \mathbb{R}^{n \times n_p}$ the Ritz reduction matrix where $n_p \ll n$, and $\underline{p} \in \mathbb{R}^{n_p \times 1}$ the generalized DOFs column. Now the reduced equations of motion can be written as

$$\mathbf{M}^{red}\ddot{\underline{p}}(t) + \mathbf{K}^{red}\underline{p}(t) = \underline{f}^{red}(t), \quad (\text{C.3})$$

with $\mathbf{M}^{red}, \mathbf{K}^{red} \in \mathbb{R}^{n_p \times n_p}$ respectively the reduced mass and stiffness matrices, and $\underline{f} \in \mathbb{R}^{n_p \times 1}$ the reduced load column defined as:

$$\begin{aligned} \mathbf{M}^{red} &= \mathbf{T}^T \mathbf{M} \mathbf{T}, \\ \mathbf{K}^{red} &= \mathbf{T}^T \mathbf{K} \mathbf{T}, \\ \underline{f}^{red} &= \mathbf{T}^T \underline{f}. \end{aligned} \quad (\text{C.4})$$

C.1 Component mode synthesis

In this project the model reduction technique Component Mode Synthesis (CMS) is applied once, which is a form of substructure coupling analysis using modal superposition. The coupling of substructures is done with superelements. These superelements are reduced models for which the responses at all DOFs are described by linear combinations of mode shapes characterized by generalized DOFs. Each CMS superelement of an undamped system is therefore partitioned according to the component physical DOF column $\underline{q} = [\underline{q}_B \quad \underline{q}_I]^T$ with q_B the boundary DOFs and q_I the internal DOFs such that:

$$\begin{bmatrix} \mathbf{M}_{BB} & \mathbf{M}_{BI} \\ \mathbf{M}_{IB} & \mathbf{M}_{II} \end{bmatrix} \begin{bmatrix} \ddot{\underline{q}}_B \\ \ddot{\underline{q}}_I \end{bmatrix} + \begin{bmatrix} \mathbf{K}_{BB} & \mathbf{K}_{BI} \\ \mathbf{K}_{IB} & \mathbf{K}_{II} \end{bmatrix} \begin{bmatrix} \underline{q}_B \\ \underline{q}_I \end{bmatrix} = \begin{bmatrix} \underline{f}_B \\ \underline{f}_I \end{bmatrix}. \quad (\text{C.5})$$

In general, the boundary DOFs column $\underline{q}_B \in \mathbb{R}^{n_B \times 1}$ with n_B the number of boundary DOFs contains: DOFs at which the reduced superelement is coupled to other (reduced) superelements, externally loaded DOFs, and DOFs with prescribed non-zero displacements. The internal DOFs column $\underline{q}_I \in \mathbb{R}^{n_I \times 1}$ with n_I the number of internal DOFs contains the remaining (unloaded) DOFs and generally $n_B \ll n_I$. By means of a coordinate transformation the physical DOFs column $\underline{q}(t)$ can be represented in terms of physical boundary DOFs \underline{q}_B extended by generalized DOFs $\underline{p}_K \in \mathbb{R}^{n_K \times 1}$ with n_K the number of generalized DOFs to actually reduce the model such that:

$$\underline{q}(t) = \begin{bmatrix} \underline{q}_B \\ \underline{q}_I \end{bmatrix} = \mathbf{T} \begin{bmatrix} \underline{q}_B \\ \underline{p}_K \end{bmatrix}, \quad (\text{C.6})$$

where generally $n_B + n_K \ll n$. Note that the reduction is achieved on the set of internal DOFs \underline{q}_I by means of a reduced set of generalized DOFs whereas boundary DOFs \underline{q}_B remain unreduced. Full behavior of the latter is required for assembly with neighboring superelements. The reduction basis consists of two types of modes: static modes to describe interaction with neighboring superelements and (a truncated set of) dynamic modes to account for the dynamics of the superelement.

Several CMS model reduction methods are extensively elaborated in other studies [17][18] of which two are elaborated and applied during this project: the fixed-interface method of Craig-Bampton and the free-interface method of Hintz-Herting. These methods are supported by ANSYS and are therefore used.

C.1.1 Craig-Bampton method

The classic fixed-interface method of Craig-Bampton is commonly used due to its ease of application and maintenance of accuracy. Usage is generally recommended when accuracy on the lower modes of the assembled structure is necessary [19]. The transformation matrix employs the interface constraint modes (static modes) plus a truncated set of fixed-interface normal modes (dynamic modes). For this reduction basis the component DOF vector $\underline{q}(t)$ is represented in terms of a static solution and fixed-interface dynamic modes approximated as:

$$\underline{q}(t) = \begin{bmatrix} \underline{q}_B(t) \\ \underline{q}_I(t) \end{bmatrix} \approx \underline{q}^S(t) + \underline{q}^D(t), \quad (\text{C.7})$$

with \underline{q}^S the dynamic response due to a linear combination of n_B static modes, and \underline{q}^D the dynamic response due to a linear combination of a truncated set of fixed-interface dynamic modes.

The static (constraint) modes are defined for boundary DOFs \underline{q}_B and the static part of (C.5) is defined as:

$$\begin{bmatrix} \mathbf{K}_{BB} & \mathbf{K}_{BI} \\ \mathbf{K}_{IB} & \mathbf{K}_{II} \end{bmatrix} \begin{bmatrix} \underline{q}_B \\ \underline{q}_I \end{bmatrix} = \begin{bmatrix} \underline{f}_B \\ \underline{f}_I \end{bmatrix}. \quad (\text{C.8})$$

It is assumed that $|\underline{f}_I| \ll |\mathbf{K}_{IB}\underline{q}_B + \mathbf{K}_{II}\underline{q}_I|$ such that $\mathbf{K}_{IB}\underline{q}_B + \mathbf{K}_{II}\underline{q}_I = \underline{0}$ can be solved resulting in

$$\underline{q}_I^S = -\mathbf{K}_{II}^{-1} \mathbf{K}_{IB} \underline{q}_B, \quad (\text{C.9})$$

which describes the static deformation of the internal DOFs \underline{q}_I as a result of a unit displacement applied to each boundary DOF in turn while the other boundary DOFs are constrained. The resulting static displacement field is a static mode for which \underline{q}^S results in

$$\underline{q}^S = \begin{bmatrix} \underline{q}_B^S \\ \underline{q}_I^S \end{bmatrix} = \begin{bmatrix} \mathbf{I}_{BB} \\ -\mathbf{K}_{II}^{-1} \mathbf{K}_{IB} \end{bmatrix} \underline{q}_B = \begin{bmatrix} \mathbf{I}_{BB} \\ \mathbf{T}_{IB} \end{bmatrix} \underline{q}_B = \mathbf{T}_{nb} \underline{q}_B, \quad (\text{C.10})$$

with the transformation matrix $\mathbf{T}_{nb} \in \mathbb{R}^{n \times n_B}$ whose columns contain the static modes. These static modes represent interaction with neighboring substructures and ensures statically correct response of the reduced model.

The fixed-interface eigenmodes (dynamic modes) are determined by fixing the boundary DOFs \underline{q}_B , i.e. $\underline{q}_B^D = \underline{0}$, and assuming that there is no external load on the internal DOFs, i.e. $\underline{f}_I = \underline{0}$. The results in

$$\underline{q}^D = \begin{bmatrix} \underline{q}_B^D \\ \underline{q}_I^D \end{bmatrix} = \begin{bmatrix} \mathbf{0}_{BK} \\ \mathbf{\Phi}_{IK} \end{bmatrix} \underline{p}_K, \quad (\text{C.11})$$

with $\underline{p}_K \in \mathbb{R}^{n_K \times 1}$ the modal participation factors of the fixed-interface dynamic modes used as measure of how strongly these modes contribute to the response of the structure when subjected to a force or displacement, and $\Phi_{IK} \in \mathbb{R}^{n_I \times n_K}$ the kept fixed-interface eigenmodes containing the eigenvectors obtained with boundary DOFs fixed. This matrix is determined by solving the eigenvalue problem

$$(-\omega_j^2 \mathbf{M}_{II} + \mathbf{K}_{II}) \phi_{Ij} = 0 \quad \text{for} \quad j = 1, 2, \dots, n_K \quad (\text{C.12})$$

containing n_K modes ϕ_{Ij} up to the user-defined cutoff frequency ω_c , i.e. $\omega_j < \omega_c$. These dynamic modes represent substructure dynamics and include only a limited number of modes in order to reduce the total number of DOFs. As a rule of thumb the fixed-interface dynamic mode cutoff frequency should be 1.5 - 2.5 times above the highest frequency of interest.

All the ingredients for the Craig-Bampton transformation are gathered and by substituting (C.10) and (C.11) in (C.7) the reduction basis results in

$$\underline{q}(t) \approx \begin{bmatrix} \mathbf{I}_{BB} \\ \mathbf{T}_{IB} \end{bmatrix} \underline{q}_B + \begin{bmatrix} \mathbf{0}_{BK} \\ \Phi_{IK} \end{bmatrix} \underline{p}_K = \begin{bmatrix} \mathbf{I}_{BB} & \mathbf{0}_{BK} \\ \mathbf{T}_{IB} & \Phi_{IK} \end{bmatrix} \begin{bmatrix} \underline{q}_B \\ \underline{p}_K \end{bmatrix} = \mathbf{T}^{CB} \underline{p}, \quad (\text{C.13})$$

where boundary displacement DOFs \underline{q}_B are retained. The reduced equations of motion are obtained by substituting (C.13) into (C.1) and pre-multiplying with $(\mathbf{T}^{CB})^T$ just as the transformation in (C.4) and can be written as

$$\mathbf{M}^{CB} \ddot{\underline{p}} + \mathbf{K}^{CB} \underline{p} = \underline{f}^{CB}. \quad (\text{C.14})$$

Note that the variables in the Craig-Bampton reduced system relate to the physical coordinates as $\underline{p} = [\underline{q}_B \quad \underline{p}_K]^T$, where \underline{q}_B contains the boundary DOFs and \underline{p}_K describes the participation of the fixed-interface dynamic modes. Via mass normalization and writing (C.14) out the reduced equations of motion result in

$$\begin{bmatrix} \mathbf{M}_{BB}^{CB} & \mathbf{M}_{BK}^{CB} \\ \mathbf{M}_{KB}^{CB} & \mathbf{I}_{KK} \end{bmatrix} \ddot{\underline{p}} + \begin{bmatrix} \mathbf{K}_{BB}^{CB} & \mathbf{0}_{BK} \\ \mathbf{0}_{KB} & \Omega_{KK}^2 \end{bmatrix} \underline{p} = \begin{bmatrix} \underline{f}_B \\ \Phi_{IK}^T \underline{f}_I \end{bmatrix}, \quad (\text{C.15})$$

with $\Omega_{KK} \in \mathbb{R}^{n_K \times n_K}$ the diagonal matrix containing the fixed interface eigenfrequencies.

C.1.2 Hintz-Herting method

The free-interface method of Hintz-Herting is generally recommended when accuracy on both lower and higher modes of the assembled structure is required [19]. The Hintz-Herting transformation matrix employs the fixed-interface constraint modes plus a truncated set of free-interface normal modes [20]. For this reduction basis the component DOF vector $\underline{q}(t)$ is represented in terms of a static solution and free-interface dynamic modes and can be approximated as:

$$\underline{q}(t) = \begin{bmatrix} \underline{q}_B(t) \\ \underline{q}_I(t) \end{bmatrix} \approx \underline{q}^S(t) + \underline{q}^R(t) + \underline{q}^E(t), \quad (\text{C.16})$$

with \underline{q}^S the dynamic response due to a linear combination of static modes, \underline{q}^R the dynamic response due to a linear combination of inertia relief modes, and \underline{q}^E the dynamic response due to a linear combination of a truncated set of free-interface elastic modes.

The static (constraint) mode part again describes the static deformation of the internal DOFs \underline{q}_I as a result of a unit displacement applied to each boundary DOF in turn while the other boundary DOFs are constrained. The resulting static displacement field is a static mode for which \underline{q}^S is similar to (C.10) and results in

$$\underline{q}^S = \begin{bmatrix} \underline{q}_B^S \\ \underline{q}_I^S \end{bmatrix} = \begin{bmatrix} \mathbf{I}_{BB} \\ -\mathbf{K}_{II}^{-1} \mathbf{K}_{IB} \end{bmatrix} \underline{q}_B = \begin{bmatrix} \mathbf{I}_{BB} \\ \mathbf{T}_{IB} \end{bmatrix} \underline{q}_B. \quad (\text{C.17})$$

The inertia relief mode part \underline{q}^R is defined as the deformation of the body subjected to a rigid body acceleration field with boundary DOFs \underline{q}_B fixed [26] resulting in

$$\underline{q}^R = \begin{bmatrix} \mathbf{0}_{BR} \\ \Phi_{IR} \end{bmatrix} \underline{p}_R, \quad (\text{C.18})$$

with $\underline{p}_R \in \mathbb{R}^{n_R \times 1}$ the modal participation factors for the rigid body modes where n_R is the number of rigid body modes (usually 6), and $\Phi_{IR} \in \mathbb{R}^{n_I \times n_R}$ the matrix of inertia relief modes defined as

$$\Phi_{IR} = -\mathbf{K}_{II}^{-1} \mathbf{M}_{IB} \Phi_{BR} - \mathbf{K}_{II}^{-1} \mathbf{M}_{II} \mathbf{T}_{IB} \Phi_{BR}. \quad (\text{C.19})$$

Here $\Phi_{BR} \in \mathbb{R}^{n_B \times n_R}$ are the rigid body modes of the boundary DOFs. The matrix of inertia relief modes Φ_{IR} is used to balance externally applied forces on a free rigid body in space. Otherwise, the rigid body would both move and vibrate due to the absence of constraints. This balancing is done by determination of the relative displacements between internal DOFs due to accelerations on both internal and boundary DOFs. This can be seen by the two parts in (C.19). The first part $-\mathbf{K}_{II}^{-1} \mathbf{M}_{IB} \Phi_{BR}$ defines the displacements of internal DOFs due to acceleration on boundary DOFs by imposing Φ_{BR} as an acceleration and determining forces on internal DOFs with $\mathbf{M}_{IB} \Phi_{BR}$. The second part $-\mathbf{K}_{II}^{-1} \mathbf{M}_{II} \mathbf{T}_{IB} \Phi_{BR}$ defines the displacements on internal DOFs due to acceleration on internal DOFs by initially mapping Φ_{BR} with $\mathbf{T}_{IB} \Phi_{BR}$ to get rigid body modes of internal DOFs and imposing these modes as accelerations to determine forces on internal DOFs with $\mathbf{M}_{II} \mathbf{T}_{IB} \Phi_{BR}$.

The deformation mode part \underline{q}^E relates to the free-interface elastic modes. These modes are defined as the relative deformation between the non-rigid free-interface elastic modes of the internal DOFs and the non-rigid free-interface elastic modes of the boundary DOFs mapped on the internal DOFs. This results in

$$\underline{q}^E = \begin{bmatrix} \mathbf{0}_{BE} \\ \hat{\Phi}_{IE} \end{bmatrix} \underline{p}_E, \quad (\text{C.20})$$

with $\underline{p}_E \in \mathbb{R}^{n_E \times 1}$ the modal participation factors for the elastic modes where n_E is the number of elastic modes, and $\hat{\Phi}_{IE} \in \mathbb{R}^{n_I \times n_E}$ the residual non-rigid free-interface elastic modes defined as

$$\hat{\Phi}_{IE} = \Phi_{IE} - \mathbf{T}_{IB} \Phi_{BE}. \quad (\text{C.21})$$

Here Φ_{IE} are the non-rigid free-interface elastic modes of the internal DOFs, and Φ_{BE} the non-rigid free-interface elastic modes of the boundary DOFs. Note that any rigid body modes present are not included in $\hat{\Phi}_{IE}$. As a rule of thumb the free-interface elastic modes cutoff frequency should be 1.5 - 2.0 times above the highest frequency of interest.

All the ingredients for the Hintz-Herting transformation are gathered and by substituting (C.17), (C.18) and (C.20) in (C.16) the reduction basis results in

$$\underline{q}(t) \approx \begin{bmatrix} \mathbf{I}_{BB} \\ \mathbf{T}_{IB} \end{bmatrix} \underline{q}_B + \begin{bmatrix} \mathbf{0}_{BR} \\ \Phi_{IR} \end{bmatrix} \underline{p}_R + \begin{bmatrix} \mathbf{0}_{BE} \\ \hat{\Phi}_{IE} \end{bmatrix} \underline{p}_E = \begin{bmatrix} \mathbf{I}_{BB} & \mathbf{0}_{BR} & \mathbf{0}_{BE} \\ \mathbf{T}_{IB} & \Phi_{IR} & \hat{\Phi}_{IE} \end{bmatrix} \begin{bmatrix} \underline{q}_B \\ \underline{p}_R \\ \underline{p}_E \end{bmatrix} = \mathbf{T}^{HH} \underline{p}, \quad (\text{C.22})$$

The reduced equations of motion are obtained by substituting (C.22) into (C.1) and pre-multiplying with $(\mathbf{T}^{HH})^T$ and can be written as

$$\mathbf{M}^{HH} \ddot{\underline{p}} + \mathbf{K}^{HH} \underline{p} = \underline{f}^{HH}. \quad (\text{C.23})$$

Note that the variables in the Hintz-Herting reduced system relate to physical coordinates as $\underline{p} = [\underline{q}_B \ \underline{p}_R \ \underline{p}_E]^T$, where \underline{q}_B contains the boundary DOFs and \underline{p}_R and \underline{p}_E describe the contribution of respectively the rigid body and elastic modes. A big advantage of the free-interface method over the fixed-interface method is that the free-interface modes as in (C.21) can experimentally be determined by testing the component in free-free conditions. However, the fixed-interface method of Craig-Bampton is easier to understand and therefore easier to apply.

Appendix D

Measurement plan

Before performing experimental modal analysis a measurement plan is made to formulate what and how to measure. EMA is essentially measuring the dynamic properties (eigenvalues and eigenmodes) of an object or system of interest using estimated FRFs. The following measurements have to be performed:

- Experimental modal analysis of the test object.
- Dynamic stiffness measurement of the test object mounted in the dynamic stiffness setup.
- Experimental modal analysis of the dynamic stiffness setup.

Two excitation principles are used: shaker excitation and modal hammer excitation. The shaker excitation (three piezo actuators for vertical excitation) is performed by sending white noise signals to the piezo actuators, which are connected to the shaker table. This excitation method is used for dynamic stiffness measurements with the test object. These results show the influence of setup related dynamic behavior which should be investigated with the results of modal hammer EMA. The modal hammer excitation is performed by hitting (components of) the setup causing an impulsive force due to the impact. It is desired to excite the setup in all directions (x, y and z) at the same time. Therefore, a 45 degrees block will be mounted in the setup as point of impact for the modal hammer. Usage of this block results in: good repeatability, excitation in all directions at the same time, and multiple position measurements at the same time using the roving sensor approach which is therefore less time consuming. This approach states that the point of impact remains the same while the sensor positions change and is used because the sensors are more flexible with respect to positioning. The hammer excitation method is used to perform EMA on the setup by measuring the resulting forces and accelerations and initially also for the test object separately. The measured analogue signals from the force and acceleration sensors are fed in data acquisition systems to condition and subsequently digitize the analogue signals. The digital signals can then be post-processed with MATLAB and/or ME'scope such that FRFs and if possible eigenmodes can be visualized to clarify the dynamic behavior of the setup. The order of performing the different measurements is as follows:

1. Initially, EMA with a modal hammer will be practiced on the test object to get familiar with the way of working during such analysis. These results are used to validate the numerical modal analysis results for the free-free boundary conditions case as elaborated in Section 3.3. This experiment is performed with the roving hammer approach for the free-free case by placing the test object on a soft egg shaped foam as shown in Figure D.1. The PCB086C03 modal hammer (steel tip) and PCB356A01 accelerometer are connected with respectively a BNC and a triax BNC cable to the data acquisition system PAK, which is connected via an USB2LAN cable to a laptop with PAK5.7 software. Note that the DYTRAN 5800B4 modal hammer (plastic tip) was initially used and therefore shown in Figure D.1, but its bandwidth is too small for modal analysis on the test object. Further details and a step-by-step guide for EMA with a modal hammer are given in Section D.1.2.

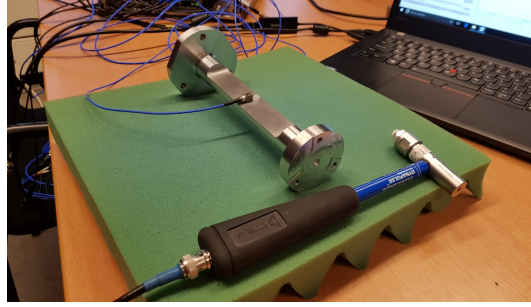


Figure D.1: The EMA with hammer excitation of the test object.

2. Afterwards, the test object is mounted in the setup and vertical piezo excitation with three piezo actuators will be used to perform a dynamic stiffness measurement of the test object. This measurement is performed by sending white noise signals to the piezos with a measurement time T of 120 s, hence a frequency resolution Δf of 0.0083 Hz, and a sampling frequency f_s of 50 kHz. The measured data will then be post-processed to investigate what dynamic behavior of the setup (resonance frequencies) is involved during dynamic stiffness measurements in a frequency range of 1 - 2000 Hz. Further details and a step-by-step guide for the measurements with piezo excitation are given in Section D.1.1.
3. Finally, an EMA on the setup will be performed with the test object still mounted in the setup. For this purpose 45 degrees blocks are attached to the frame and shaker table. These two components are used to excite the system such that dynamic behavior of the whole setup is accurately captured.

The goal is to clarify and understand dynamic behavior of the setup such that it can be distinguished in dynamic stiffness results and to update the FE model. Note that it is important to correctly document each measurement point for data post-processing by making pictures for example. During all these measurements a lot of equipment is required, which is listed in Table D.1 including the amount and the corresponding measurement and/or excitation types.

Table D.1: The measurement equipment for dynamic stiffness measurements and modal analyses.

Equipment	Type/Comment	Amount	Excitation type
Data acquisition	dSPACE1007	1	Piezo
PC	PC connected to dSPACE	1	Piezo
Piezo	PI P225.40	3	Piezo
Piezo amplifier	PI E472.20	2	Piezo
Signal conditioning	B&K 2692 and B&K 2693	5	Piezo
Force cell	Kistler 9027C	3	Piezo
Accelerometer	B&K4381	6	Piezo
Accelerometer	PCB356A15	5	Piezo and modal hammer
Accelerometer	PCB356B18	5	Piezo and modal hammer
Data acquisition	PAK	1	Modal hammer
Cable	USB2LAN	1	Modal hammer
Laptop	Laptop with PAK5.7 software	1	Modal hammer
Modal hammer	DYTRAN 5800B4 or PCB086C03	1	Modal hammer
Block	45 degrees block	1	Modal hammer

D.1 Experimental modal analysis guide

D.1.1 Piezo measurements

Piezo excitation is used to perform dynamic stiffness measurements. During dynamic stiffness measurements, the shaker table gets excited for which the resulting forces are measured at the force cell on top of the test object and the accelerations are measured on the shaker table interface as well as on the MF. The force cell consists of three Kistler 9027C force sensors measuring three DOFs each, which are combined to a global six DOF force cell. The accelerations are measured with four accelerometers (one PCB356B18 sensor for xy -direction, three B&K4381 sensors for z -direction) on the shaker table interface as well as on the MF. As preparation for the dynamic stiffness measurements, a Simulink scheme that defines the data acquisition has to be created. A step-by-step guide on how to perform a dynamic stiffness measurement is listed below:

1. Initialize object and setup for measurement
 - Check mounting of the test object in the setup, i.e. the alignment with respect to the shaker interface and force cells and the fixation of the bolts.
 - Pressurize the bellow such that the vertical force on the object meets the payload specification according to $F = pA$ with $A = 0.015 \text{ m}^2$.
 - Lift the steel cylinder by pressurizing the bellow such that it is not resting on the end stop bolts. Check that the vertical spacing between these end stop bolts and the steel cylinder is 1-2 mm. The measurement should be performed in this lifted situation.
 - Check that the vertical spacing between the end stop nuts and washers above the steel cylinder and the frame is 1-2 mm. Also check that the threaded rods do not touch the frame in horizontal direction.
 - Check whether the deformation of the leaf springs is within acceptable limits. The leaf springs contain a few saw cuts to minimize their in-plane stiffness and are easily damaged because of this.
 - Check that the accelerometers are fixed properly at the desired locations, because the bee wax may let loose.
 - Check the routing of all sensor cables, because the tape may let loose.
2. Initialize data acquisition
 - Switch on the dSPACE data acquisition box.
 - Switch on the B&K Nexus and Deltatron amplifiers.
 - Check that the Nexus and Deltatron settings are correct:
 - Sensor sensitivity should match the calibrated values.
 - Output gain should be a balance between sufficient output signal magnitude and no signal overload. Check the output signal magnitude indicator on the amplifier display and check that the red overload light is not on. Readjustment after putting the excitation signal on may be necessary.
 - Floating correction factor should be 1.
 - Check that the low pass and high pass filter frequencies are as desired. Default settings used in the dynamic stiffness setup are 0.1 Hz for the high pass filter and 3 kHz for the low pass filter.
 - Switch on the PI piezo amplifier.
3. Initialize software
 - Start the PC and start MATLAB R2016b. During startup a dSPACE RTI Platform Support window pops up. The Real-Time Interface (RTI) corresponding to the dSPACE hardware (DS1007) has to be selected.

- Start Simulink and open the Simulink scheme made in the preparation phase.
- Build the model by clicking on the *Build Model* icon in the toolbar. This generates several files that are being used in the background for the communication between dSPACE and the PC.
- Start dSPACE ControlDesk 6.0 and open the dSPACE ControlDesk project and experiment made in the preparation phase.

4. Perform measurement

- Click *Go Online* in the toolbar at the top. Values will appear for the buttons and displays in the layout part in the center of the screen. All the names correspond to the names in the Simulink scheme.
- Click *Start Measurements* in the toolbar at the top.
- Set the gains for the piezos and the shaker. For vertical measurements, set piezo gains to 1 and shaker gain to 0.
- Set the *Noise power* gain to a low value to start with, e.g. 0.01.
- Switch on the noise using the NoiseONOFF button. Immediately stop the excitation in case of too large displacements of the steel cylinder, measurement object, or excitation table. Also stop the excitation immediately in case of excessive sound.
- Check that the end stops (bolts at the bottom and nuts and washers at the top of the steel cylinder) are not being hit. Also check that the threaded rods do not make contact with the frame in horizontal direction. If anything is hit, stop the excitation immediately.
- Check the signal magnitude indicators of the Nexus and Deltatron amplifiers. The signal magnitude should be as high as possible for the best signal to noise ratio and measurement quality, but without having signal overload. Adjust the output gain if necessary. Write down the values of the output gains of all channels, because this information is needed for the post-processing.
- Increase or decrease the *Noise Power* gain if necessary. Repeat the previous two steps if the *Noise Power* gain is changed. If it is desired to change the gain in specific frequency ranges only, the excitation signal filtering settings have to be changed. This needs to be done in the Simulink scheme. Stop the measurements, adapt the Simulink scheme, and go back to the third bullet of step 3.
- Change the recorder settings. The recorder is being used to make time traces.
 - Select *Recorders* in the *Measurement Configuration* tab in the left part.
 - Create a new recorder if necessary with right mouse button on *Recorders* → *Create New Recorder*.
 - Select the *Storage information* bullet. Set the measurement data file name properties. Set automatic export to MATLAB files on. Set the data export folder.
 - Select the *Stop Condition* bullet. Set the time limit to the desired values.
- Start making a time trace by click *Start triggered* → *Recorder 1*. The status of the time trace is shown at the bottom right. Wait until the measurement is finished.
- Switch off the excitation signal using the NoiseONOFF button.

5. Stop measurement

- Click *Stop Measuring* in the toolbar at the top.
- Click *Go Offline* in the toolbar at the top.
- Make sure the steel cylinder rests on the end stop bolts (release the bellow pressure by pressing in the valve of the bellow if necessary).
- Switch off the piezo amplifier.
- Switch off the Nexus and Deltatron acquisition box.

- Switch off the dSPACE data acquisition box.
- Close the dSPACE software.
- Log off from the PC. Do not switch off the PC. This would disallow to do a remote login onto the PC, which is useful for: transferring measurement data, postprocessing data, and doing modifications on the Simulink scheme or in dSPACE ControlDesk.

Measurement data will be post-processed in MATLAB/ME'scope. The dynamic behavior of the setup involved during dynamic stiffness measurements has to be investigated by performing EMA on the setup.

D.1.2 Modal hammer measurements

Experimental modal analysis of the setup is performed with modal hammer excitations. This excitation signal is in principle a Dirac function with uniform amplitude for all frequencies. In practice the bandwidth will be limited and is controlled by the material of the hammer head and mass of the hammer. The harder material used at the tip, the shorter the pulse duration and hence the higher frequency range which can be measured. Sufficient pre-trigger length should be used to ensure that the full impact pulse is captured. The modal hammer has a force transducer built in its head and the output of this transducer will be measured as well as acceleration response due to the hammer impact. Averaging of the resulting signals of at least three hits is necessary, because hitting the structure at the same place in the same direction is practically impossible. Furthermore, to avoid signal leakage and to reduce the impact of noise after the hammer impact windowing techniques should be used. The data acquisition system used during these measurements is PAK for which a laptop with PAK5.7 software is required.

In the preparation phase make sure that the modal hammer and accelerometers are properly attached to the PAK system, which is connected to the laptop with PAK software using an USB2LAN cable. Also, make sure that the correct modal hammer with the desired head is used and that the 45 degrees block as well as the accelerometers are mounted at the correct grid locations. Remember that during experiments on the setup the roving sensor approach is used and during experiments on the test object the roving hammer approach is used. A guide to perform modal hammer measurements is listed below:

1. Initialize software

- Start PAK by using desktop shortcut *PAKProjectManager*
- Create a new project by clicking *New Project*. Measurement setup and all custom settings are stored in a project.
- When a project is created, press the *Start PAK* button.
- To start an impact measurement, press the *Impact Measurement* button at the top.
- In the *Settings* tabs the title, expert, division, description, test name, and subtitle can be given.
- Continue to *General Settings* and fill in the correct PAK settings.
- Continue to *Specific Settings* and fill in the correct impact measurement settings.

2. Perform measurement

- Go the *Measurement* tab.
- Press start in the *Control System* tab. The screen will switch to *Signal History*, where the impacts measured at the hammer and responses measured by accelerometers are shown. Axes can be scaled such that signals are clearly visible.
- Press start again in the *Control System* tab. Now there is one test to determine the measurement range, which continues with the measurements (preferred to be at least 3) to determine the average transfer function of the test subject. Afterwards, press *Apply Position* and then press *Stop*.

3. Measurement data clean up with FFT windowing

- View the single diagram of time block acceleration.
- Enable the FFT *Window Parameters - Response Position* by pressing the button. The window can be changed by tuning parameters or sliding the markers.
- When a proper window is chosen, press the green *OK* symbol.
- This windowing procedure can be repeated for the hammer input in a similar way. When windowing is completed, most likely the coherence is improved.
- Go back to *Settings* and save the parameters, such that the final FFT windowing parameters are saved as well.
- Remove all unwanted measurements.
- Go to *Measurements* → *View Measurement* and return to the tab *Measurement* and press *Save Analysis*. Now the subtitle is changed from *subtitle* to *subtitle.analysis*. The latter should be converted to MATLAB data.

4. Data conversion to MATLAB

- Preparation
 - Generate an ATFX header file in PAK by navigating to the Data Viewer application within PAK (the most left icon in the PAK main window).
 - Right-click on either a complete measurement project, a set of tests or a single measurement.
 - Either choose *Generate ATF* or *Administration* → *Add ref. ATF*. The first option will duplicate your measurement data and is therefore generally not preferred. The latter option only adds the *header.atfx* file to your measurement.
 - Measurements are now ready for conversion to MATLAB.
- PAK2MAT conversion
 - Drop ATFX files or measurement directories from windows explorer. The PAK2MAT Queue List will be filled and PAK2MAT start the conversion to .mat files.
 - Before the conversion, PAK2MAT needs to be configured. Go to *Preferences* and click *Derive from system variables*. Choose an export location, preferably the MATLAB directory in the project folder.
 - It is possible to easily reduce the amount of export data by filtering the data set. Therefore, go to *Plugins* and select the desired data types.

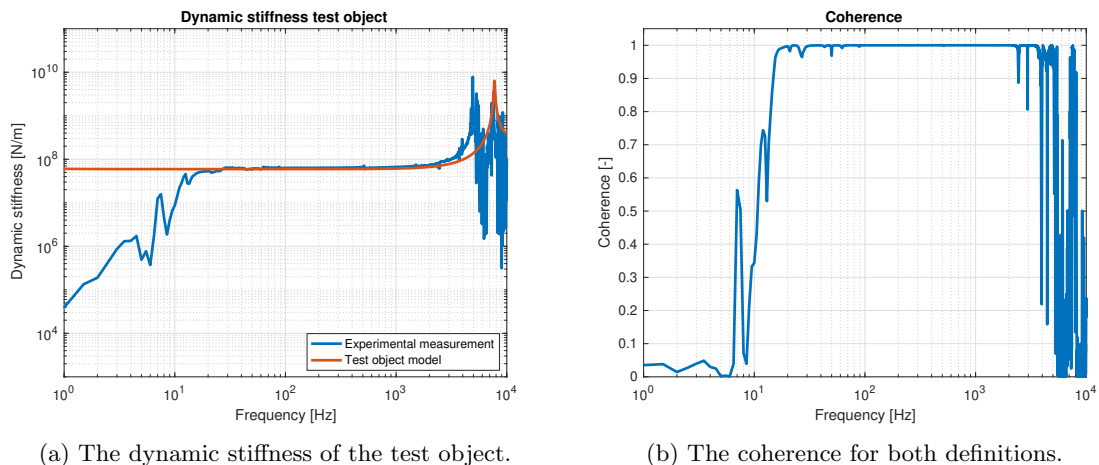
After the measurements the data has to be post-processed and the dynamic stiffness setup modes will be investigated such that the dynamic behavior of the setup will be fully understood in the frequency range of 1 - 2000 Hz. With these results also the FE model will be updated where necessary such that it better represents reality.

Appendix E

Dynamic stiffness measurement investigations

E.1 Accelerometer fixation

Proper fixation of sensors is relevant and influences the results. An example of a measurement with inappropriate accelerometer fixation is shown in Figure E.1a as will be explained later in this section. Numerical dynamic stiffness results of the test object model with 1% damping are also shown in Figure E.1a as the expected results. The corresponding coherence is shown in Figure E.1b. The shown frequency range is 1 - 10000 Hz in order to visualize the vertical z mode of the test object as well.



(a) The dynamic stiffness of the test object.

(b) The coherence for both definitions.

Figure E.1: The dynamic stiffness and coherence of the first measurements.

Several notable phenomena in the results can be discussed. Firstly, one can see that the model roughly matches the experimental results apart from the low frequency region until 20 Hz and the high frequency region from 2 kHz - 3 kHz onwards where measurement quality is poor. The dynamic behavior of the setup also influences the experimental results and therefore differs from the model, where setup behavior is not involved hence representing pure behavior of the test object. Lastly, the low frequency peaks and the high frequency noise in the dynamic stiffness results as well as the poor coherence indicate a poor measurement quality. This poor quality is caused by the fact that the MF accelerometer a_{z2} was not properly fixed during these measurements, which can be checked with for example the transfer from input voltage to acceleration of each accelerometer on the MF as shown in Figure E.2. Each accelerometer should measure approximately the same acceleration.

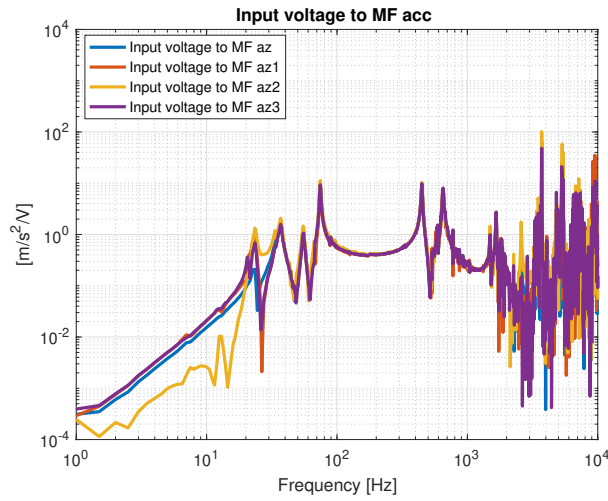


Figure E.2: The transfer from input voltage to MF accelerations.

It can be seen that the MF accelerometer a_{z2} diverges from the other two accelerometers especially in the low frequency region. Since the accelerations should be approximately similar this indicates inappropriate fixation.

E.2 Standstill measurements

Influence of noise on the measurements is examined by performing standstill measurements. The resulting power spectra of the relative accelerations of a reference dynamic stiffness measurement and a standstill measurement are compared as shown in Figure E.3.

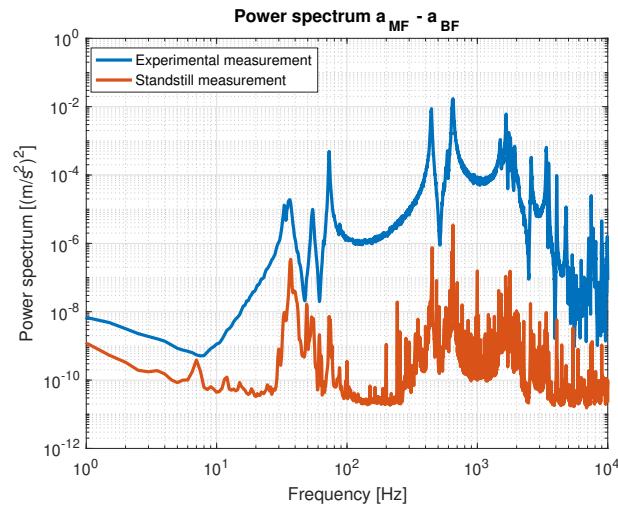


Figure E.3: The power spectrum of a reference and a standstill measurement.

It can be seen that for low frequencies the power spectrum of the standstill measurement (noise) is approximately 10% of the power spectrum during an actual measurement with active piezos. This indicates that measurement noise greatly influences the measurements as was also shown in Figure 4.3 until 5 Hz. It also means that for low frequencies not much energy is inserted into the system during measurements, which can perhaps be improved by changing the input signal.

Declaration concerning the TU/e Code of Scientific Conduct for the Master's thesis

I have read the TU/e Code of Scientific Conduct¹.

I hereby declare that my Master's thesis has been carried out in accordance with the rules of the TU/e Code of Scientific Conduct

Date

05-06-2019

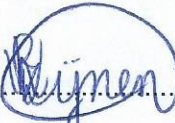
Name

R. A. G. (Ruud) Wijnen

ID-number

0856504

Signature



Submit the signed declaration to the student administration of your department.

¹ See: <http://www.tue.nl/en/university/about-the-university/integrity/scientific-integrity/>

The Netherlands Code of Conduct for Academic Practice of the VSNU can be found here also.

More information about scientific integrity is published on the websites of TU/e and VSNU